DESIGN OF BIORESORBABLE MAGNESIUM ALLOY

by

Tilottoma Saha

Student ID- 1017112010

MASTER OF SCIENCE IN MATERIALS AND METALLURGICAL ENGINEERING

Supervisor: Dr. Fahmida Gulshan

Co-supervisor: Dr. Syed Ansar Md. Tofail

Department of Materials and Metallurgical Engineering

Bangladesh University of Engineering and Technology

Dhaka-1000, Bangladesh

November 2021

Declaration

I, Tilottoma Saha, hereby declare that this thesis is entirely my work, and any part of it has not been submitted anywhere else for the award of any degree. All quotations, figures, and results from other sources are duly acknowledged and referenced.

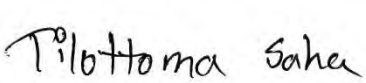

……

Student ID-1017112010

Tilottoma Saha

Department of Materials and Metallurgical Engineering

BUET, Dhaka

The thesis titled "DESIGN OF BIORESORBABLE MAGNESIUM ALLOY" Submitted by Tilottoma Saha, Roll No. 1017112010 and Session: October 2017 has been accepted as satisfactory as partial fulfilment of the requirement for the degree of Master of Science in Materials and Metallurgical Engineering on November 13, 2021.

Board of Examiners

1. Fahmida

Dr. Fahmida Gulshan
Professor
MME, BUET, Dhaka

Chairman
(Supervisor)

2.

Dr. Syed Ansar Md. Tofail
Associate Professor, Dept of Physics
Bernal Institute,
University of Limerick, Ireland

Member
(Co-Supervisor)

3. M.HADAN

Head/Director
Professor
MME, BUET, Dhaka

Member
(Ex-Officio)

4. Hamid

Dr. Hossain Mohammad Mamun Al Rashed
Associate Professor
MME, BUET, Dhaka

Member

5.

Dr. Al-Nakib Chowdhury
Professor
Chem, BUET, Dhaka

Member (External)

Dedication……..

To Dr. Fahmida Gulshan, whose constant warmth and companionship I could not repay.

Acknowledgements:

First and foremost, praises and thanks to God, the Almighty, for His showers of blessings throughout my research to complete the research successfully.

I owe a deep sense of gratitude to Prof. Dr. Fahmida Gulshan, my supervisor and advisor, for her invaluable advice, continuous support, and patience during my MSc. study. Her immense knowledge and experience have encouraged me in my academic research and daily life. I want to thank my esteemed co-supervisor, Dr. Syed Ansar Md. Tofail for his unwavering support, supervision, and tutelage during my work with the MOSAIC group of the Bernal Institute of the University of Limerick.

I profusely thank Garry Warren and Sarah Markham, University of Limerick, Ireland. Their prompt inspiration, timely suggestions, kindness, enthusiasm, and dynamism have enabled me to complete my thesis.

I am incredibly grateful to my parents for their love, prayers, caring, and sacrifices to educate and prepare me for my future. I am very much thankful to my peers, friends, and colleagues for their love, understanding, prayers, and continuing support to complete this research work.

Tilottoma Saha acknowledges European Commission Erasmus International Credit Mobility 2015-2020 between the University of Limerick, Ireland and Bangladesh University of Engineering and Technology, Dhaka, Bangladesh, for a seven-month secondment at the Modelling, Simulation, and Innovative Characterization (MOSAIC) group of the Bernal Institute of the University of Limerick, where a part of the research leading to the current thesis was conducted. Neither the European Commission nor the University of Limerick holds any responsibility for this thesis's content and conclusions.

Abstract:

In recent times, Magnesium alloys have been attractive in medical science since they have compatible mechanical properties with the cortical bone and bioresorbable properties. Depending on the fabrication method, alloy element, and coating surface, the degradation rate in the physiological condition can be tailored. The present study investigated the Spark Plasma Sintering (SPS) effect on the entirely newly designed Mg alloy. All alloying elements (Zn, Er and Ce) were chosen based on the Mg matrix's solubility and their mechanical properties and cytotoxic behaviour in the in-vivo condition. The sintering temperature on the microstructure, hardness and corrosion behaviour of a high-energy ball-milled $Mg_{.67}Zn_{.02}Er_{.2}Ce_{.01}$ was investigated. Along with that, the effect of alloying elements on the microstructure and radiographic properties was also examined. During the SPS, holding time and sintering pressure kept constant while varying the sintering temperature from 400^{o}C to 420^{o}C. The grain size and microstructure were investigated using optical microscopy (OM), scanning electron microscopy (SEM), and energy-dispersive X-ray spectroscopy (EDS). Corrosion behaviour was studied in the simulated body fluid using the milligram per decimeter per day (MDD) method, and the radiographic property was tested in the soft X-ray range. Vickers hardness and corrosion performance improved for the samples prepared at 420^{o} C, whereas radiopacity under x-ray increased. A possible reason for strengthening and corrosion behaviour has been discussed in light of reduced porosity and grain size. Alloying bioserobale Mg with rare earth metal-Er can provide duel effects such as bioabsorbility and high radiopacity. So, a positive correlation between the opacity enhancement under the x-ray and the presence of Erbium is also under consideration. Suggestions for future design and processing of Mg alloys for bioresorbable implants are provided.

Keywords: Magnesium alloys; Spark Plasma Sintering (SPS); Bioresorbable; Microstructure; Hardness; Corrosion; Radiopacity

TABLE OF CONTENT

LIST OF FIGURES

LIST OF TABLES

Chapter-1

Introduction

For the last few decades, the development of biocompatible implant materials has focused on implants with little degradation in body fluid and, ideally, no release of material into the surrounding tissue. The advent of biodegradable implant materials changed this premise: degradation products are now generated in considerable amounts, and the organism must cope with them. Another concept is bioresorbable implant material which can be absorbed in the body, causing a minimum effect on the body environment [1]. Absorbable materials can be used in various applications, including temporary scaffolds, temporary barriers, drug delivery systems, and multifunctional devices. An absorbable scaffold provides mechanical support that gradually transfers the load to the natural healing tissue. An absorbable suture offers an excellent example of a scaffold, as it initially seals a wound but absorbs over time while the skin heals. Hernia repair can often result in scar tissue between the abdominal wall and vital internal organs. A degradable barrier is well suited to prevent such unwanted attachment of tissues until healing is complete. Absorbable drug delivery devices provide opportunities for controlled release near the targeted tissue without the need to remove the carrier implant in a follow-up operation. Some implants may require incorporating a device with two or more functions. For example, an absorbable orthopaedic implant might provide initial mechanical support while eluting beneficial drugs or growth factors into the surrounding bone tissue. Multifunctional degradable implants can be highly diverse, depending on their intended functions [2].

The biocompatibility of released substances and their impact on surrounding tissue and the whole organism has become important implant material design factors. Medical implants are often placed inside the human body to support organs and tissues. Bioresorbable Implants (BRI) paved the way for the ‘fourth revolution in interventional cardiology because they could provide temporary scaffolding and then ‘disappear’ (resorb), potentially significantly improving coronary artery disease treatment. BRI technology has gradually matured and improved, and they have the attention currently undergoing preclinical or clinical testing worldwide. Due to the concerns about polyester-based scaffolds, biodegradable metallic implants hold great promise because they exhibit mechanical properties that match but can be based on naturally occurring metals in the human body. Necessary materials classes are iron (Fe)-based or magnesium(Mg) -based alloys, which have been the subject of numerous attempts to understand implant degradation behaviour as well as the impact of the degradation products on the bone-forming processes [3].

Magnesium alloy is now one of the most promising resorbable technologies, although available evidence on its performances in vivo is limited to small observational studies. Mg shows excellent potentials as a bioresorbable medical implant. Specifically, Mg is cytocompatible with many human cells in vitro and Vivo. Mg naturally degrades in the human body, which eliminates the secondary removal procedure of the implant. The primary degradation product, Mg ions, is an

essential element in over 300 enzymatic metabolisms. As a light metal, Mg possesses an adequate mechanical strength, even for the load-bearing condition in orthopaedic device applications [4]–[6].

The powder metallurgy (PM) process is well known to be one of the excellent metal forming techniques for producing high-quality structural components with a near-net shape. It can produce alloys and composites that conventional melting and casting processes [1]. Various PM technologies have been proposed, such as (1) pressureless sintering (PLS) after unidirectional compacting or hydrostatic compacting (CIP), (2) hot isostatic pressing (HIP), and (3) spark plasma sintering (SPS). SPS is also called pulse electric current sintering, which can significantly improve the properties of sintered samples. The main advantages of SPS are a local high-temperature generation at the created contact, rapid heating, and consolidation. This technique has already been used to consolidate the various metal powders. For magnesium, while reports on SPS sintering of magnesium and its alloy have been available, no study on Mg-Zn-Er-Ce based alloy has been reported yet [7].

1.1 Aims and objectives

The research aims to design an alloy of Magnesium (Mg), Zinc (Zn), Cerium (Ce), and Erbium (Er) powders that are Mg0.67Zn0.02Er0.2Ce0.01 and establish its fortune to be used in clinical purposes.

The aims of this research project:

i. Designing and Sample preparation of potential bioresorbable Mg-alloys for the clinical application.

ii. Analysis of the bioresorbable Magnesium alloys' mechanical, corrosion, and biodegradable properties.

iii. Evaluating the results and measuring the prepared biodegradable alloy's overall performance (trial and error basis).

1.2 Research questions

Magnesium is one of the significant essential elements of the body that performs more than 300 biochemical reactions. It has biodegradable nature in body fluid, so much advanced research has been conducted to establish its use in implants which will degrade after serving its purpose.

A highly specialised SPS machine has conducted this research to sinter an Mg-based completely new alloy and identify its suitability as an implant material. Such a study was expected to be helpful to improve its property with further modifications. Improved radiopacity was anticipated due to the presence of Er, which would be a suitable replacement of gold or platinum-like biomarker in the implant material.

The sustainability of the alloy material in the mimic body fluid was also investigated to identify its corrosion rate so that it can be used inside the body only with some modifications.

The research purpose of knowing and investigating the following queries:

i. What is the possibility of producing this newly designed Mg-Zn-Er-Ce based alloy using the SPS method and introducing this alloy as implants for clinical purposes?

ii. What is the effect of sintering temperature on the new alloy?

iii. What is the optimum sintering conditions for this alloy?

iv. How do microstructures, hardness and corrosion properties vary depending on sintering temperature?

1.3 Research hypothesis

Medical implants can be used in a range of applications, such as vascular stents and bone repair. Traditional permanent implants are standard and typically made from titanium or stainless steel; however, they often require a secondary operation for removal. On the other hand, bioresorbable materials, including magnesium alloys, allow for optimal healing before resorbing into the body as the surrounding tissue replaces the implant. Bioresorbable implants can also provide matching resorption kinetics to the healing period. This bioresorbability prevents the need for secondary surgical procedures, which can be costly and stressful for patients [8].

Bioresorbable implants are increasing within the medical industry, competing with the more traditional titanium implants. Recent developments within the bioresorbable implants market include magnesium alloys, which offer new, revolutionary solutions, demonstrating biocompatibility and biosafety. Magnesium alloys present opportunities across the medical device market, from orthopaedic implants to veterinary applications. The alloys have recently been used in cardiovascular stents, known as scaffolds [9].

Bioresorbable materials are advantageous throughout the medical device market because they offer a steady resorption rate and help achieve optimum body healing. Polymer materials have been used as a bioresorbable option for a few years; however, magnesium alloys now offer an improved alternative. Compared with the relatively low strength of polymers, magnesium demonstrates a tensile strength closer to that of natural bone. This means that these alloys are much more suited for use in load-bearing mechanical medical devices. Magnesium is also a naturally occurring element in the body, with proven biocompatibility.

Magnesium's biocompatibility means that the body can remove magnesium degradation products. Studies of blood following magnesium implants within the body revealed that resorption caused little change to the composition, with no disorder to the liver or kidneys [10].

This research has been carried out based on the following hypotheses:

1. It is possible to design and sinter a magnesium-based alloy using spark plasma sintering.
2. The sintered alloy may be feasible as a resorbable medical implant.

1.4 Structure of the thesis

This book contains the introduction, literature review, material selection, experimental procedure, results and discussion, and conclusion.

In the chapter one, the aim and objectives of this work specifying the research questions. The research hypothesis includes purposes and possible reasons behind this research. Along with that, the structure of this thesis has been described here.

In the chapter two, the review of previous related works to this thesis work. It contains the history of bioresorbable magnesium, effects of alloying elements, classifications, and applications of Mg alloys as body implant, mechanical and corrosion properties in different environmental conditions, x-ray radiopacity of alloy different metallic materials. In chapter three, the process of material selection by using xmudat software has been discussed based on the phase diagram. Brief descriptions of the instrument and its working principle have been incorporated in chapter four. This chapter contains raw materials processing, powder metallurgy, SPS methodology, heat treatment, different experiments such as SEM and EDS analysis, hardness, corrosion, and radiopacity analysis. It provides a detailed description of the activities carried out to synthesicharacterisationise Magnesium alloy. In chapter five, all the obtained experimental results and relevant explanations have been summarised. Finally, in chapter six, a conclusion has been drawn from the main empirical results.

Chapter-2

Literature review

2.1 Implants

Implants are traceable to early Egyptians and South-Central American cultures, and with all the developments in material and biological science, we have come a long way. Improvements in the implant material's quality and quantity have made this treatment modality very promising, budding, and highly practised in today's era. The Earliest dental implants of stone and ivory were various polymers, including ultrahigh molecular weight polyurethane, polyamide, polymethylmethacrylate resin, polytetrafluoroethylene, and polyurethane, have been used as the dental implant. In the present era, due to the advancements in biomaterials available for dental implants, newer materials came into being, such as zirconia, roxolid, surface-modified titanium implants. These materials fulfil the functional requirements and are also esthetically pleasing [1], [2]. Figure 2.1. describes the chronology of biomaterials from replacement to regeneration. Implant materials can be classified based on the type of material used and the biological response they elicit when implanted; this classification is shown in Table 2.1.

Table 2. 1-Classification of implant materials:

Biodynamic activity	Chemical composition		
	Metals	Ceramic	Polymer
Biotolerant	Gold Co-Cr alloys Stainless steel Niobium Tantalum		Polyethene Polyamide Polymethylmethacrylate Polytetrafluoroethylene Polyurethane
Bio Inert	Commercially pure titanium Titanium alloy (Ti-6AL-4U)	Al oxide Zirconium oxide	
Bioactive		Hydroxyapatite Tricalcium phosphate Bioglass Carbon-silicon	

2.2 Historical Development of Implant Material:

2.2.1 Ancient Era (through AD 1000)

Implants are traceable to ancient Egyptian and South American civilisations. There is a skull from the pre-Columbian era in which artificial tooth is carved with dark stone. Albucasis de condue Arabian surgeon, credited with a written paper of transplants to replace missing teeth [3].

2.2.2 Foundational period (1800-1910)

This era is the beginning of Endosseous oral implant topology. Maggiolo, in 1809 used gold in the shape of the tooth root. In 1887 Harris reported using teeth made of porcelain into which led coated platinum posts were fitted. In 1890, Zamenski reported the implantation of teeth made of porcelain, gutta-percha, and rubber, and in 1898 R.E Payne placed a silver capsule in the tooth socket. In early 1900, ’s lambaste fabricated implants of aluminium, silver, brass, red copper, magnesium, gold, and soft steel plated with gold and nickel [3].

2.2.3 Premodern era (1901-1930)

In 1901 a technique of capsule implantation was reported in dental cosmos, which R.E Payne presented at the clinics of the third international dental congress. In 1903, Sholl in Pennsylvania implanted a porcelain tooth with a corrugated porcelain root. In 1913, Dr. Edward J. Greenfield introduced the basket of iridium and 24-carat gold into the alveoli. E. J Greenfield also introduced the concept of submerged implant, the healing tissue, and dental implant immobility [3].

2.2.4 Dawn of the modern era (1935-1978)

In this era, synthetic polymers, ceramics, and metal alloys started replacing the naturally derived materials because they have better performance and more predictable results than natural ones. Strock anchored a Vitallium screw within the bone and immediately mounted it with a porcelain crown. He was the first to achieve implant survival for 15 years [3].

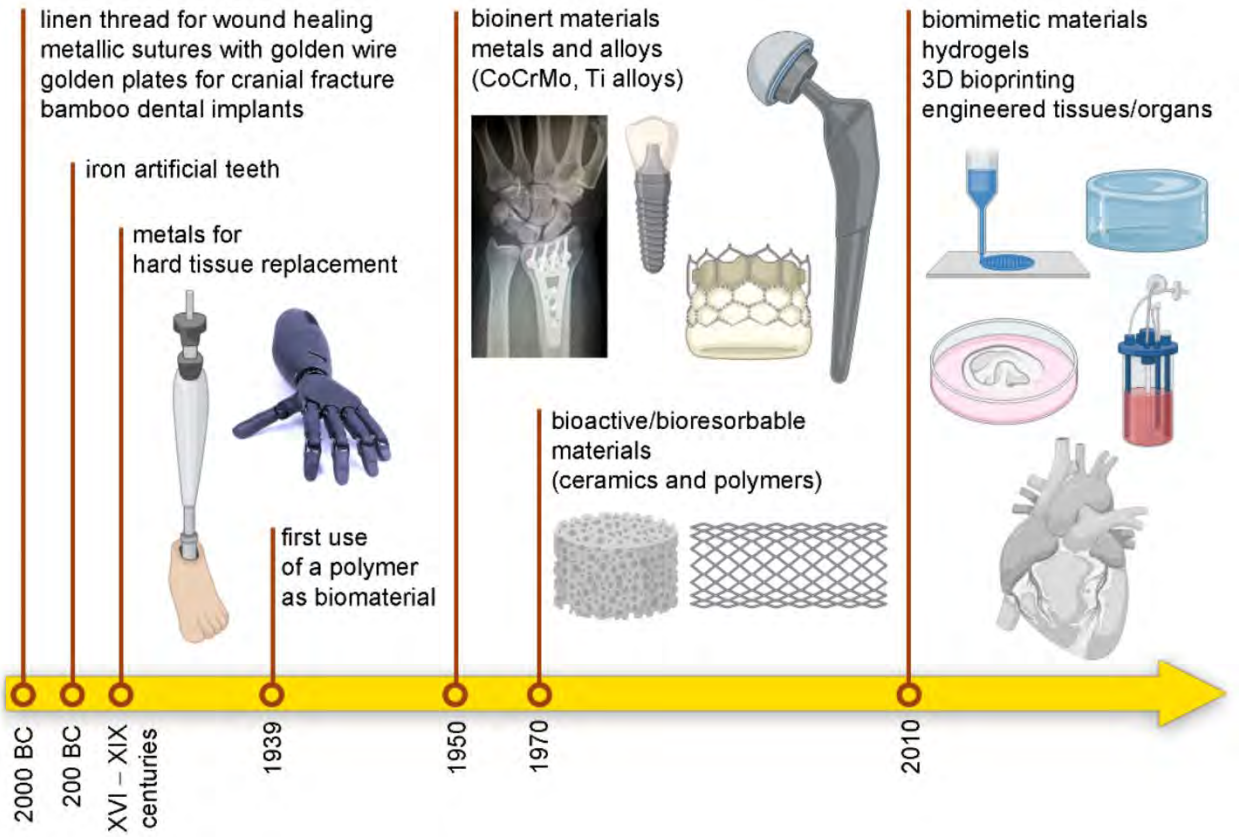

Figure 2.1. Chronology of biomaterials: from replacement to regeneration.

2.2.4.1 Polymers:

The early work with the methyl methacrylate resin implants mainly met with failures. However, polymers were biologically tolerable substances. Research on polymethacrylate tooth-replica implants led to the development of the polymer dental implant. In replacing a natural tooth, the polymer replica proved ideal for restoring function and appearance. Polymers were selected for the following reasons:(1) The physical characteristics of the polymers can be altered based on their use as their composition may be changed easily. Polymers can be transformed into more porous or softer form; (2) Polymers can be manipulated easily and allow better reproduction; (3) Polymers do not generate microwaves or electrolytic current as do metals; (4) They show fibrous connective tissue attachment; (5) They can be easily microscopically evaluated than with metals; and (6) They are more esthetically pleasing. There are some disadvantages: (1) inferior mechanical properties; (2) lack of adhesion to living tissues; and (3) adverse immunologic reactions [4]–[6].

2.2.4.2 Metals and metal alloys:

Metals have biomechanical properties, which makes them suitable as implant material. Besides these properties' metals are also easy to process and have a good finish. Metallic implants can be sterilised by the standard procedure, making them easy to use. But due to advancements with time and low success rates with metals (gold, stainless steel, cobalt-chromium), these materials have

become obsolete and are now replaced by newer ones. Titanium (Ti) and its alloys (mainly Ti-6Al-4V) have become the metals of choice for dental implants. However, prosthetic components of the implants are still made from gold alloys, stainless steel, and cobalt-chromium and nickel-chromium alloys [7]–[24].

Cobalt chromium alloys are used in cast or cast and annealed metallurgic conditions. It allows the manufacture of customised implants, such as subperiosteal frames. The elemental composition of this alloy includes cobalt, chromium, and molybdenum as the significant elements. Cobalt provides a continuous phase for basic properties. Chromium provides corrosion resistance through the oxide surface. Molybdenum provides strength and bulk corrosion resistance. Nickels bio corrosive product and carbon must be accurately controlled to enhance mechanical properties, such as ductility [7], [8], [13], [16], [25]–[27].

Iron-Chromium-Nickel Based Alloys Stainless steel alloys are used for orthopaedic and implant devices. Iron-based alloys are used for ramus blades, ramus frames, stabiliser pins, and mucosal inserts. The alloy is most prone to pitting corrosion. Care must be taken to use and retain the passivated (oxide) surface condition, as this alloy contains nickel as a significant element. Its use in allergic patients must be avoided. They have high galvanic potentials and corrosion resistance. This can result in galvanic coupling and biocorrosion if titanium, cobalt, zirconium, or carbon implant biomaterials are used with it [6], [25].

2.2.5 Implants in the 21st Century:

Titanium has a good record of being used successfully as an implant material. This success with titanium implants is credited to its excellent biocompatibility due to forming a stable oxide layer on its surface.

The commercially pure titanium (cpTi) is classified into four grades which differ in their oxygen content. Grade 4 has the most (0.4%), and Grade 1 has the least (0.18%) oxygen content. The mechanical differences between the different grades of cpTi are primarily because of the contaminants present in minute quantities. Iron is added for corrosion resistance, aluminium is added for increased strength and decreased density, while vanadium acts as an aluminium scavenger to prevent corrosion. The Hexagonal close-packed crystal lattice of Ti is called the α-Ti (α-phase). On heating it at 883 ℃ phase transformation occurs from hexagonal close-packed to body-centred cubic lattice or b- phase. Ti is reactive as it spontaneously forms a dense oxide film at its surface. Ti is a dimorphic metal, i.e., below 882.5 ℃, it exists as α-phase, and above this temperature, it changes from α- phase to b phase. Because of the high passivity, controlled thickness, rapid formation, ability to repair itself instantaneously if damaged, resistance to chemical attack, catalytic activity for several chemical reactions, and modulus of elasticity compatible with that of bone. Ti is the material of choice for intraosseous applications [9], [28].

Disadvantage: There is an esthetic issue due to the grey colour of the titanium. This is more pronounced when the soft tissue situation is not optimal. The dark colour shines through the thin mucosa.

Titanium alloys Ti6Al4V Titanium reacts with several other elements, e.g., silver, Al, Au, Cu, Fe, Ur, Va, and Zn, to form alloys. Titanium alloys exist in three forms alpha, beta, and α-b. These types originate when pure titanium is heated with elements Al, Va in certain concentrations and cooled, these types originate. These added elements play like Phase- condition stabilisers. Aluminium is an alpha-phase condition stabilizer, and it also increases the strength and decreases the weight of the alloy. Vanadium acts as a beta-phase stabiliser. The temperature at which α-to b transformation occurs changes to a range of temperatures as Al or Va is added to Ti. Both α and b forms exist in this range. Temperatures to which the desired form is present can be obtained by quenching alloy at room temperature. For increasing the strength, these alloys may be heat treated. The alloys most used for dental implants are of the alpha-beta variety. The most common contains 6% Al and 4% Va. (Ti 6 Al 4V) [3], [22].

Ceramics were used for surgical implant devices because of their inert behaviour and good strength and physical properties such as minimum thermal and electrical conductivity. Specific properties of ceramics like low ductility and brittleness have limited the use of ceramics [29]–[31].

Aluminium, titanium, and zirconium oxides Root form or endosteal plate form and pin-type dental implants are generally made from High ceramics from aluminium, titanium, and zirconium oxides. The compressive, tensile, and bending strengths exceed the strength of compact bone by 3 to 5 times. These properties combined with high moduli of elasticity and especially with fatigue and fracture strength have resulted in specialised design requirements for this class of biomaterials [3], [32]–[34].

2.2.6 Modern Era:

Modern Implant dentistry is delineated from the mid-1930s to the present. Today's popularity of implants in dentistry is attributed to the developments and the research work which laid the foundation of this field. Because of all this work in the past, we see implant concepts developing into the most sophisticated and popularly utilised systems.

The treatment options and modalities for achieving optimal functional and aesthetic outcomes with implant restorations have changed recently. Pure titanium is generally preferred for a dental implant because of its excellent biocompatibility and mechanical properties. There might be aesthetic problems due to the grey colour of the titanium. There may be a soft tissue recession; there is an unaesthetic display of the metal components in such situations. Therefore, implant research has focused on discovering tooth-coloured implant material that improves the aesthetic appearance of dental implants and, at the same time, is highly biocompatible and able to withstand the forces present in the oral cavity and therefore, zirconia came into being [35].

In the early nineties, zirconia was used for dental prosthetic surgery with endosseous implants. Ceramic implants were introduced for osseointegration, less plaque accumulation resulting in improved soft tissue management and aesthetic consideration as an alternative to titanium implants.

Monoclinic (M), cubic (C), and tetragonal (T) are the three crystal forms in which polymorphic Zirconia structure is present. Zirconia, at room temperature, acquires a monoclinic structure and changes into a tetragonal phase at 1170 ℃, followed by a cubic phase at 2370 ℃. At room temperature, these phases are unstable and break into pieces on cooling. The C-phase of pure Zirconia can be stabilised by adding CaO, MgO, and Y2O3 (Yttrium), resulting in multiphase material called partially stabilised zirconia (PSZ) combining cubic, monoclinic, and tetragonal phases in the order of importance. Tetragonal zirconia polycrystals (TZP) containing tetragonal phase can be obtained by adding Yttrium at room temperature. Yttria stabilised TZP possesses low porosity, high density, high bending, and compression strength and is suitable for biomedical applications [30].

Titanium zirconium alloys (Straumann Roxolid) with 13%-17% zirconium (TiZr1317) have better mechanical attributes, such as increased elongation and fatigue strength than pure titanium. Titanium and Zirconium do not prevent the growth of osteoblasts that are essential for osseointegration. Straumann developed Roxolid that fulfils dental implantologists' requiremens and is 50% stronger than pure titanium. Sandblasting and acid-etching on, TiZr1317 with a monophasic structure results in a topographically identical surface as sterile titanium implant because of its superior mechanical properties. Thin implants and implant components that can be subjected to high strains can be produced using TiZr1317 due to its better mechanical properties, provided that the material shows similar good biocompatibility as pure titanium. [3] Figure 2.2: History and growth of biomaterials as a field and industry have been described briefly.

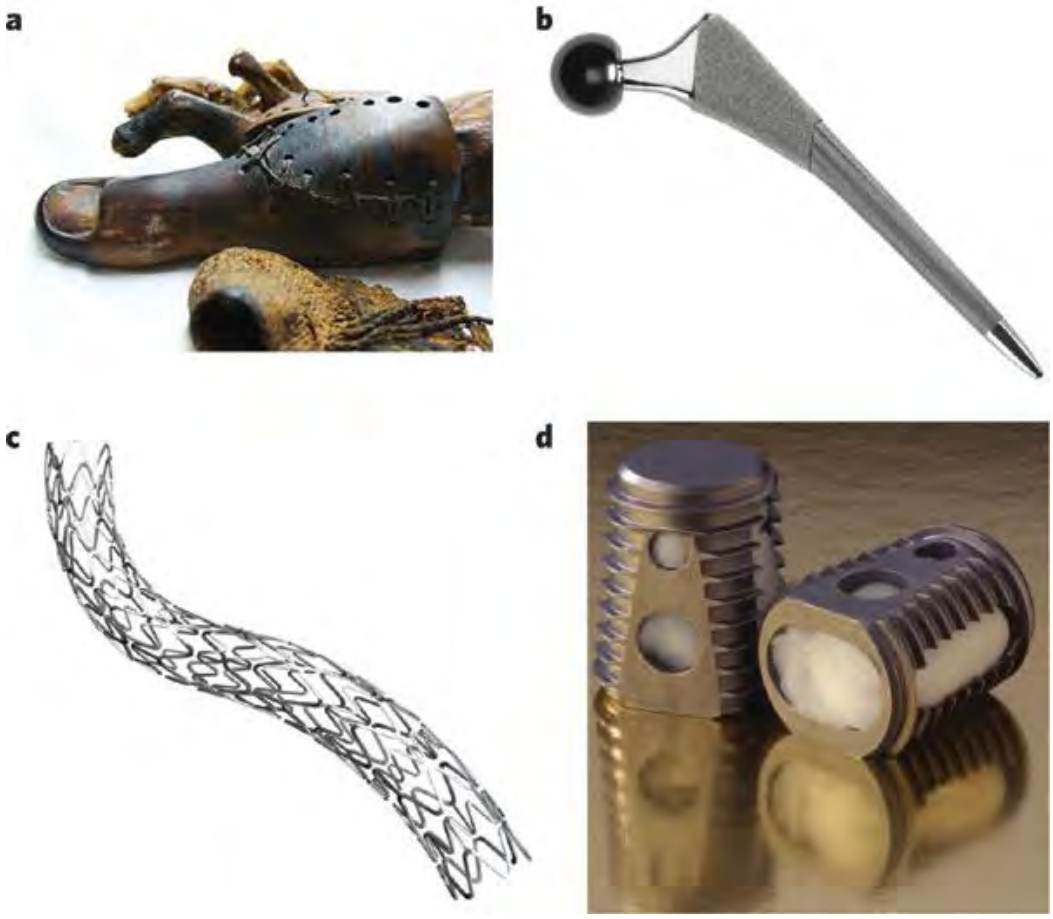

Figure 2.2: History and growth of biomaterials as a field and industry. a Prosthetics fashioned from natural materials: wooden toe, circa 1065–740 BC, used as a prosthetic to replace an amputated toe and identified in an anthropological excavation of the Thebes West tombs, Egypt. (Image courtesy of J. Finch, KNH Centre for Biomedical Egyptology, University of Manchester, UK, and The Egyptian Museum, Cairo.) b, The SYNERGY hip implant is an example of a state-of-the-art prosthetic device that uses synthetic materials fabricated and engineered to meet performance demands. (Image courtesy of Smith and Nephew, London.) c, d, Commercially available combination products with synthetic components and biological activity. c, The TAXUS Express2 Atom Stent, a metal stent from which paclitaxel is eluted into small coronary vessels to prevent restenosis (cell-mediated narrowing of the vessels). (Image courtesy of Boston Scientific Corporation, Massachusetts.) d, The INFUSE Bone Graft device, a combination product that uses standard prosthetic components (a steel cage) and a tissue-engineering approach (a bovine type I collagen sponge from which recombinant human bone morphogenetic protein 2 is eluted) to provide stability while spinal tissues are being regenerated. (Image courtesy of G. K. Michelson and Medtronic, Burlington, Massachusetts.)

2.3 Properties of an Implant Biomaterial:

2.3.1 Bulk properties

Modulus of elasticity: Implant material with a modulus of elasticity comparable to bone (18 GPa) must be selected to ensure a more uniform distribution of stress at the implant and minimise the implant-bone interface's relative movement.

Tensile, compressive, and shear strength: An implant material should have high tensile and compressive strength to prevent fractures and improve functional stability. Improved stress transfer from the implant to bone is reported interfacial shear strength increases and lower stresses in the implant.

Yield strength, fatigue strength: An implant material should have high yield strength and fatigue strength to prevent brittle fracture under cyclic loading.

Ductility: A minimum flexibility of 8% is required for the dental implant. Ductility in the implant is necessary for the contouring and shaping of an implant.

Hardness and Toughness: Increase in hardness decreases the incidence of wear of implant material, and an increase in toughness prevents fracture of the implants [8], [31], [33], [36]–[42].

2.3.2 Surface properties

Surface tension and surface energy: It determines the wettability of the implant by wetting fluid (blood) and cleanliness of the implant surface. Osteoblasts show improved adhesion on the implant surface. Surface energy also affects the adsorption of proteins.

Surface roughness: Alterations in the surface roughness of implants influence the response of cells and tissue by increasing the surface area of the implant adjacent to bone and thereby improving cell attachment to the bone.

Implant surfaces have been classified on different criteria, such as roughness, texture, and orientation of irregularities: (1) The implant surfaces according to the surface roughness: Minimally rough (0.5-1 m), Intermediately rough (1-2 m), Rough (2-3 m); (2) The implant surface can also be classified according to their texture as concave texture (mainly by additive treatments like hydroxyapatite (HA) coating and titanium plasma spraying), convex texture (mainly by subtractive treatment like etching and blasting); and (3) The implant surface can also be classified according to the orientation of surface irregularities: Isotropic surfaces: have similar topography independent of measuring direction; Anisotropic surfaces: have clear directionality and vary considerably in roughness [5], [15], [36], [41], [43], [44].

2.3.3 Corrosion:

2.3.3.1 Clinical significance of corrosion: Implant biomaterial should be corrosion resistant. Corrosion can result in roughening of the surface, weakenithe restoration, releasing elements from the metal or alloy, toxic reactions. Adjacent tissues may be discoloured, and allergic reactions in patients may result due to the release of factors [7], [39], [42], [45]–[49].

2.3.3.2 Influence of Media in Corrosion:

The Body Environment

The water content of the human body ranges from 40% to 60% of its total mass. The whole body water can be subdivided into two major fluid compartments: extracellular and intracellular fluids. Extracellular fluids (ECFs) consist of the plasma found in the blood vessels, the interstitial fluid surrounding the cells, the lymph, and transcellular fluids (e.g., cerebrospinal fluid and joint fluids). Intracellular fluid (ICF) refers to the water inside the cells. The amount and the distribution of body fluids and electrolytes are kept regular and constant. A mechanism is known as homeostasis.

Electrolytes play a significant role in body functionality. Among various functions, they take part in metabolism, determine the cell membrane potentials and osmolarity of body fluids, and so forth. Major cations include hydrogen, sodium, potassium, calcium, and magnesium ions. Major anions include hydroxide, bicarbonate, chloride, phosphate, and sulfate ions. Dissolved salts are probably the most influential components for implant corrosion in vivo. Chloride ions (and other halides) enhance the corrosion of almost all metals and interfere with many corrosion protection methods.

Temperature and pH are two important factors affecting the corrosion bbehaviour of materials. Under normal conditions, body fluids have a temperature of 37 °C. This can be regarded as a constant temperature throughout the lifespan of an implant concerning corrosion. [21], [24], [50], [51]

The hydrogen evolution reaction (HER) and oxygen evolution reaction (OER) are two essential reduction reactions in corrosion in general and in vivo. The HER in acid solutions is.

$2H^{+}+2e^{-}\rightarrow H_2$, (1)

whereas in alkaline solutions, it is written as

$2H_2O+2e-\rightarrow H_2+2(OH)^{-}$. (2)

The Nernst equation for the HER is

$Erev=2.3RT/2F*\log[H+]2[H_2] = -2.3RT/2F*\log[H_2] -2.3RT/F*pH.$ (3)

The OER in neutral or acidic solutions can be written as

$O_2+4H^{+}+4e^{-}\rightarrow 2H_2O$, (4)

whereas in alkaline solutions, it is

$4(OH)^{-}\rightarrow O_2+4e^{-}+2H_2O$. (5)

The corresponding Nernst equation is.

$$E_{rev} = +1.229 + 2.3RT/4F * \log[O_2] - 2.3RT/F * pH, \quad (6)$$

where $[H_2]$ and $[O_2]$ represent the partial pressures of hydrogen and oxygen, respectively.

In addition to the above HER and OER reduction reactions, the following reactions, Equations (7) through (10), are some other possible reduction reactions occurring at implant surfaces. Hydrogen peroxide (H_2O_2) and hydroxide radicals ($HO\cdot_2$ and $OH\cdot$) participate in these reactions. It is thus evident that certain intermediate species, which are known to considerably affect the biological system and prompt oxidative stress in cells, might result from reduction processe—many other possible reduction reactions in vivo, including reducing disulfide bonds and other protein-like molecules. The local redox environment around a metallic implant can influence the redox state of cells [7], [8], [51].

$$O_2 + 2H_2O + 2e^- \rightarrow H_2O_2 + 2(OH)^-, \quad (7)$$

$$H_2O_2 + 2e^- \rightarrow 2(OH)^-, \quad (8)$$

$$O_2 + H_2O + e- \rightarrow HO\cdot_2 + (OH)^-, \quad (9)$$

$$HO\cdot_2 + H_2O \rightarrow H_2O_2 + OH\cdot. \quad (10)$$

Neutrality is defined when $[H^+] = [OH^-]$. Thus, pH = 7 for neutrality at 25 °C. However, because the equilibrium constant (ionic product) is a function of temperature, the pH at neutrality depends on temperature. For example, $K_w = 2.4 \times 10^{-14}$ (mol $L^{-1})^2$ at 37 °C; thus, the corresponding pH value at neutrality in the human body will be 6.81. The acid-base balance is an important part of homeostasis: metabolism depends sensitive to pH. The normal pH range for blood plasma is 7.35 to 7.45. A decrease in blood pH below normal is known as acidosis, whereas an increase in blood pH above normal is known as alkalosis. Buffers resist changes in pH. Two major mechanisms control the body's pH: chemical and physiological. The rapid-acting chemical buffers (e.g., bicarbonate, phosphate, and protein systems) immediately (i.e., in fractions of a second) combine with any added acid or alkali that enters the body fluids, thus preventing drastic changes in hydrogen ion concentration and pH. Suppose the immediate action of chemical buffers cannot stabilise the pH. In that case, the physiological buffers (i.e., respiratory and urinary response systems) serve as a secondary defence against harmful shifts in pH. The physiological buffer system controls the output of acids, bases, or CO_2. The respiratory response system buffers within minutes, whereas the urinary response system requires several hours, but it buffers the greatest quantity.[26], [42]

When an implant is placed in vivo, the disruption of blood supply to the bone is often accompanied by severe pathological infections that might affect the healing and cause electrochemical variations in the equilibrium state. In addition, the pH of the body fluid can drop from 7.4 to 5.5, and it could take 10 to 15 days to recover its expected value. A bacterial infection could result in an even more comprehensive pH range near the implant surface, from acidic to alkaline (4.0 to 9.0, respectively). The pH around a newly inserted implant can drop to as low as 4.0 due to the build-up of hematomas, a condition that could last for several weeks. The local decrease in pH could result in

severe localised corrosion of the metal implant. In addition, H_2O_2 may form during the initial stages of the inflammatory response to implant in vivo. The level of the pathological changes depends on the biological activity of any corrosion products released from the implant and the implant size and shape; it could vary across the implant's surface, possibly leading to the development of electrochemical cells. The risk of localised corrosion due to local variations in pH in the vicinity of titanium alloys has also been reported based on in vitro studies [30], [39], [40].

The most important body fluids that influence the corrosion of metal implants are chloride, dissolved oxygen, and pH levels. Body fluids may seem slightly less aggressive than seawater, based on the lower pitting resistance equivalent number (PREN) of 26 and greater recommended to prevent pitting corrosion of stainless steels in vivo than the value of 40 usually required for stagnant seawater. However, the dissolved oxygen levels in the blood are lower than in artificial solutions exposed to the air atmosphere due to haemoglobin, which is the main component of red blood cells. The partial pressure of oxygen in the blood varies between 100 to 40 mmHg for arterial and venous blood, respectively. The corresponding value in the air is 160 mmHg. Because most biomaterials rely on oxygen to passivate, the passivation of metal surfaces is more difficult under low dissolved oxygen concentration conditions. Indeed, deaeration of the solution with high-purity nitrogen gas to maintain low O_2 concentration was found better to predict the in vivo performance of metal implants. Since the partial pressure of oxygen varies widely within the body, from about 2.67×10^2 to 1.33×10^4 Pa, an implant surface can contact anatomical environments of widely different oxygen partial pressures, thus possibly establishing aeration cells. Another gas, carbon dioxide (CO_2), influences the corrosion in vivo by affecting the pH. Bicarbonate levels are about twenty times higher in blood than in seawater [12], [17], [20], [51]–[53].

The corrosion behaviour of an alloy is rarely, if ever, a linear combination of the corrosion behaviour of its components. Even for a given composition, the corrosion of an alloy usually depends on metallurgical factors such as the material's grain size and heat treatment. An extreme example is the high corrosion resistance of some so-called glassy metals or amorphous alloys compared to crystalline alloys of the same composition.

Dissolved oxygen, dissolved bicarbonate, and other body fluids constituents (e.g., phosphates, cholesterols, and phospholipids) are usually thought to play no role in the corrosion process or exist at insignificant levels. Therefore, most in vitro experiments have been conducted in saline or standard isotonic solutions such as Ringer's or Hank's. The presence of bicarbonate and calcium chloride is the main difference compared to saline. Blood has been used in some corrosion studies, often adding sodium citrate to the blood as an anticoagulant. Nevertheless, sodium citrate has been shown to affect the passivation behaviour of Co-Cr-Mo alloys and stainless steels, among others. Some studies have avoided anticoagulants by performing the tests in blood serum [54]. Compositions of selected body fluids and simulated body fluids (SBFs) are provided in Table-2.2 and Table-2.3, respectively. Phosphate buffered saline (PBS) is mostly recommended because it maintains the constant pH throughout in vitro experiments. A review by Solar [7], [8], [55] concluded that inorganic solutions based on diluted NaCl were indeed satisfactory substitutes for human body fluids when studying the behaviour of passive metals. Thus, many researchers use the simple saline solution (0.9 wt% NaCl in DI water) for in vitro experiments. However, some

differences between in vivo and in vitro corrosion evaluation have been reported, attributed, among others, to the higher concentration of dissolved oxygen in isotonic solutions than venous blood. In addition, accelerated in vivo corrosion may be associated with some minor constituents in blood. For example, sulphur contained in amino acids may enhance crevice corrosion of stainless steels [16], [42], [47], [56]–[58]. Another cause of difference between corrosion data acquired in vivo versus in the laboratory stems from different hydrodynamic conditions affecting the implant surface. For example, blood flow can cause mass transport-limited reactions at noticeably different rates than assessed in the lab.

Table 2. 2- Composition of various body fluids:

Component	**Interstitial Fluid ($mg \cdot L^{-1}$)**	**Synovial Fluid ($mg \cdot L^{-1}$)**	**Serum ($mg \cdot L^{-1}$)**
Na^+	3280	3127	3265
K^+	156	156	156
Ca^{2+}	100	60	100
Mg^{2+}	24	---	24
Cl^-	4042	3811	3581
HCO_3^-	1892	1880	1648
HPO_4^{2-}	96	96	96
SO_4^{2-}	48	48	48
Organic acids	245	---	210
Protein	4144	15,000	66,300

Table 2. 3- Compositions of various simulated body fluids (SBFs):

Component	**PBS ($g \cdot L^{-1}$)**	**Ringer's ($g \cdot L^{-1}$)**	**Hank's ($g \cdot L^{-1}$)**
NaCl	8.00	8.60	8.00
$CaCl_2$	---	0.33	0.14
KCl	0.20	0.30	0.40
$MgCl_2 \cdot 6H_2O$	---	---	0.10
$MgSO_4 \cdot 7H_2O$	---	---	0.10
$NaHCO_3$	---	---	0.35

NaH_2PO_4	1.15	---	---
$Na_2HPO_4 \cdot 12H_2O$	---	---	0.12
KH_2PO_4	0.20	---	0.06
Phenol red	---	---	0.02
Glucose	---	---	1.00

Concerning dental implants, the environment in the oral cavity is not well-defined. Several recipes exist for artificial saliva; the most popular one is that of Fusayama [23], [49], [59], that is, 0.400 $g \cdot dm^{-3}$ NaCl, 0.400 $g \cdot dm^{-3}$ KCl, 0.795 $g \cdot dm^{-3}$ $CaCl_2 \cdot H_2O$, 0.690 $g \cdot dm^{-3}$ $NaH_2PO_4 \cdot H_2O$ and 0.005 $g \cdot dm^{-3}$ $Na_2S \cdot 9H_2O$, at pH 5.5. However, the composition of human saliva varies considerably between individuals, especially in the sulfide content, which can cause tarnishing of both silver- and gold-based amalgams. Many foodstuffs are acidic and have high chloride content; thus, they are significantly more corrosive than saliva. In addition, oral hygiene has a strong effect on the corrosiveness of the oral environment. Finally, many dental products and solutions contain fluoride, which is harmful to the passive layer. Some of the special varnishes used by dentists, for example, contain more than 2 wt% fluorides. Thus, although dental implants are relatively accessible for repair or replacement, there has been a concern that the toxicity of metals leaching out from amalgams, Nitinol, and other dental materials might cause oral cancer [7], [55], [57], [60], [61].

The Effect of Biological Macromolecules

Biological macromolecules can change the corrosion rate by interfering in different ways with anodic or cathodic reactions. Proteins and lipids from the ECF adsorb onto the implant surface and may change their chemical properties through oxidation and hydrolytic reactions.

Many articles report the effects of **proteins** on the corrosion behaviour of different biomaterials, yet the conclusions are ambiguous. This is probably due to varying experimental procedures (e.g., which proteins were used) but also because the effect of a specific protein varies on different metals and alloys. Proteins may have several effects on corrosion behaviour: (1) Proteins can bind to metal ions and transport them away from the implant surface. This will destabilise the equilibrium across the electrical double layer (EDL) and further dissolve the metal. (2) Proteins can affect the electrode potential due to their electron-carrying capability, whereas bacteria can change the pH of the local environment by the generation of acidic metabolic products. (3) The adsorption of proteins onto the surface of biomaterials could limit the diffusion of oxygen to some areas of the surface, thus causing preferential corrosion of oxygen-deficient regions and breakdown of the passive layer. (4) An adsorbed protein layer could act as a barrier between the metal surface and the environment, thus inhibiting corrosion. (5) In the case of wear or wear-assisted corrosion reactions, proteins can act as lubricants on the surface. The procedures used to study protein effects on metals vary greatly, in that either serum (containing many proteins) or single proteins (most frequently–albumin, is the most abundant protein in the blood) are added [5], [13], [36], [52], [62].

Cells can significantly influence the nature of the passive films and the corrosion behaviour of metallic biomaterials. However, the effects observed depend on the type of metal/alloy studied. As typically, the cell-material interactions are cell-specific, it is not possible to draw a general conclusion on the effect of cells on the corrosion behaviour. Like the discussion in the last paragraph, different effects of cells on the corrosion behaviour could be expected when they adhere on surfaces: (1) the cell layer could act as a physical barrier, blocking the surface and thus increasing its corrosion resistance. (2) Cells may release oxidising solid agents and enzymes targeted at decomposing the implant material. Cell metabolism products could influence surface reactions. For instance, macrophages can generate active oxygen species (O_2^-, for example), which can lead to increased metal release from titanium in the absence of wear and fretting [16], [46], [63]–[65].

Bacteria near an implant could consume hydrogen released in cathodic reactions, thus accelerating the corrosion process.

The Effects of Relative Motion and Crevices

The relative motion between an implant and tissue surfaces might accelerate the wear of both surfaces, thus stimulating chronic inflammation and creating an even severer chemical environment. Some implants inherently introduce crevices with local solution chemistry significantly different from the physiological environment of 0.154 M saline at pH 7.4. Examples include modular tapers and metal-on-metal (MoM) hip replacements. Analysis of retrieved implants has indicated that the pH within taper crevices could be lower than 1 and that cation concentrations within tapers could be orders of magnitude higher than in the peri-implant tissues [47], [56], [57], [66].

2.3.3.3 Correlations Between In Vitro and In Vivo Tests

Corrosion of metals in vivo may be regarded as an electrochemical process. While the electromotive force (EMF) series lists metals according to their thermodynamic driving force to undergo oxidation, the practical nobility of metals in vivo may be different either because: (1) the biomaterial is an alloy rather than a pure metal, (2) the pressure-concentration-temperature conditions are not standard, or (3) the implant is surrounded by serum ions, proteins, and cells, which may all affect local corrosion processes. Hence, significantly differenbehaviourson behaviours have been documented in non-physiological in vitro, physiological in vitro, and in vivo studies. Since all metals corrode to some extent in vivo, one should refer to corrosion control rather than corrosion prevention. International standards of metallic implants and medical devices typically include a requirement for corrosion tests. After implantation, raised metal concentrations are often measured even in remote organs. This may be related to ionisation and phagocytosing cells circulating small metal and metal oxide particles [33], [50].

Comparisons between in vitro and in vivo corrosion data concluded that:

- Certain organic species, notably serum, accelerate the corrosion rate in vivo of some metals and alloys under non-fretting (static) conditions. Such species should be included in artificial test environments to better correlate with these metals' in vivo corrosion rates.

- The use of electrochemical test methods for corrosion testing, especially in the presence of complex organic species, simple sulfides, and other possibly electrochemically active compounds, should be avoided if such compounds, by their anodic oxidation, were shown to interfere with the measurement. This is probably most significant with noble metals and more minor with passivating metals.
- Given the slowness of the passivation process for specific metals and alloys, the value of short-term (i.e., less than 1,000 h) experiments is questionable for these materials.
- Electrochemical techniques conducted in simple electrolytes, such as PBS, afford a reasonable means of ranking or screening biomaterials, subject to comments 1 to 3 above.
- The importance of correct specimen mounting to avoid undesired crevice formation and the role of solution agitation effects should be borne in mind.
- The formation in vivo of a soft or hard tissue capsule around an implant may retard corrosion. It should be possible to simulate this in laboratory corrosion tests by applying some sheath around the test specimen.

The corrosion of metallic implants can affect the surrounding tissues in three ways: (i) electrical current may affect the behaviour of cells, (ii) the corrosion process may change the chemical environment, and (iii) metal ions may affect cellular metabolism. One of the issues that arise from the release of corrosion products into the body is systemic and remote effects. Mild corrosion in many cases can also produce symptoms, which range from a local tenderness at the site of the corroded area to acute pain, reddening, and swelling over the whole general area around the device. A systemic reaction to metallic implants stems from this flux of metal ions released by corrosion. Organ-specific accumulations of specific metal ions and the simultaneous ion-specific excretion rates from the body could lead to the establishment of elevated concentrations of typical alloying elements of implants. This could upset the overall balance established by physiological tolerance to toxicity [11], [12], [67]. In animals and patients with either stainless steel or cobalt-base orthopaedic total joint replacement (TJR) components, corrosion and wear produce longer-term changes in blood composition, primarily in its metal content. These include high metallic content in tissue (at both local and remote sites, e.g., kidney and liver) and metal-bearing ion concentrations in serum and urine. However, histology has not provided clear proof of the slow release of metal ions. The discolouration of the surrounding tissue and the FBRs point to implant corrosion as the origin of these metal ions.

Metallosis is the local destruction of soft and hard tissues due to metal implants. It is often associated with significant osteolysis and is sometimes reflected by infiltration of periprosthetic soft tissues and bone by metallic debris resulting from wear of joint arthroplasties.[7], [22], [26], [27], [55] By themselves, metal ions lack the structural complexity required to challenge the immune system. However, when combined with proteins, such as those available in the skin, connective tissues, and blood, a wide variety of metals induce immune responses and thus should be considered harmful. Cobalt, chromium, and nickel are the most common examples, nickel having the most potent effect. Delayed type IV hypersensitivity is the most typical response of a

metal-sensitized individual to such metal ions [7], [68]–[70]. Table-2.4 lists the adverse effects of some metals.

Table 2. 4-The biological effects of specific metal ions that may be leached in vivo due to corrosion.

Nickel (Ni)	The major cause of allergic contact dermatitis. The significant biological parameter is the amount released to the skin during exposure to human sweat. Threshold: 0.5 mg cm^{-2} $week^{-1}$, only a minor part of Ni-sensitive subjects will react. Has toxic effects with cellular damage in cell cultures at high concentrations. Harmful to bone in tissue cultures, although less than Co or V. Has a potency for carcinogenicity. A normal blood level of Ni is about 5 mg L^{-1} [43], [60], [61], [70]–[72]
Cobalt (Co)	Its function is confined to its role in vitamin B12. Anaemia B inhibiting Fe absorption into the bloodstream [7], [8], [13], [16], [25]–[27]
Chromium (Cr)	Ulcers and central nervous system disturbances. Blood level average: 2.8 µg/100 g). Its compounds are only poorly absorbed after oral ingestion, and Cr (III) storage is largely confined to the reticuloendothelial systems. Cr(VI) ion is able to pass the plasma membrane freely in both directions [7], [8], [13], [25], [27], [64], [66]
Aluminium (Al)	Epileptic effects and Alzheimer's disease [14], [30], [33], [73]
Vanadium (V)	Toxic in the elementary state [14], [73]
Molybdenum (Mo)	An essential dietary element. Its highest concentration in the liver: 1–3 ppm. Is necessary for the function of certain enzymes. Is quite readily absorbed from the intestinal tract. It is toxic in large doses; symptoms include diarrhoea, coma and cardiac failure, and inhibition of ceruloplasmin, cytochrome oxidase, glutaminase, choline esterase, and sulfite oxidase. High levels of Mo can also interfere with Ca and P metabolism [3]

Metal ions released into the human body do not permanently harm it; their partner is vital (Figure-2.3figure). Whether an ion will be active and immediately react with water molecules or inorganic anions depends on the number and mass of the molecules. For example, titanium ion is very active. It readily reacts with hydroxyl radicals and anions, forming oxide and salt in body fluids, thus indicating that the possibility of combination with biomolecules is low. However, this does not mean that the reaction of titanium ions with biomolecules will not occur at all. Zirconium, niobium, and tantalum ions behave like titanium ions.

On the other hand, inactive ions, such as nickel and copper, do not immediately combine with water molecules and inorganic anions and last in the ionic state for a relatively long time.

Therefore, these ions have a higher chance of mixing with biomolecules and exhibit toxicity. To conclude, the following factors must be considered when dealing with the toxicity of metallic biomaterials: (1) corrosion resistance of the material, (2) ions released by corrosion and wear, (3) activity of the released ions, and (4) toxicity of the ion itself.

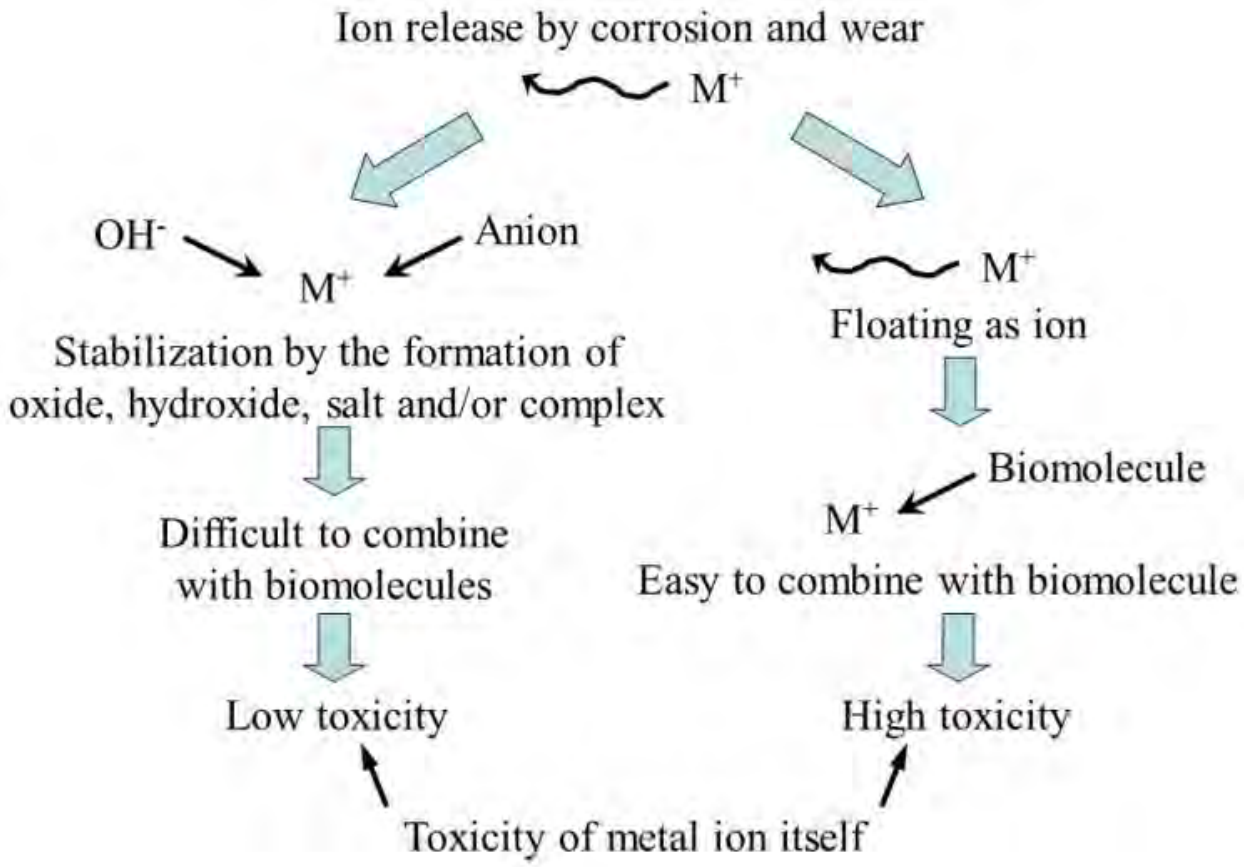

Figure 2.3: Two possible toxicity routes for metal ions released into body fluids due to corrosion and wear. [32], [64], [69]

Figure 2.4 illustrates that the biologic reactivity of implant debris causes local immune responses primarily mediated by macrophages, which produce reactive oxygen intermediates and pro-inflammatory cytokines that affect a host of local cell types and induce a widening zone of soft-tissue damage and inflammation.

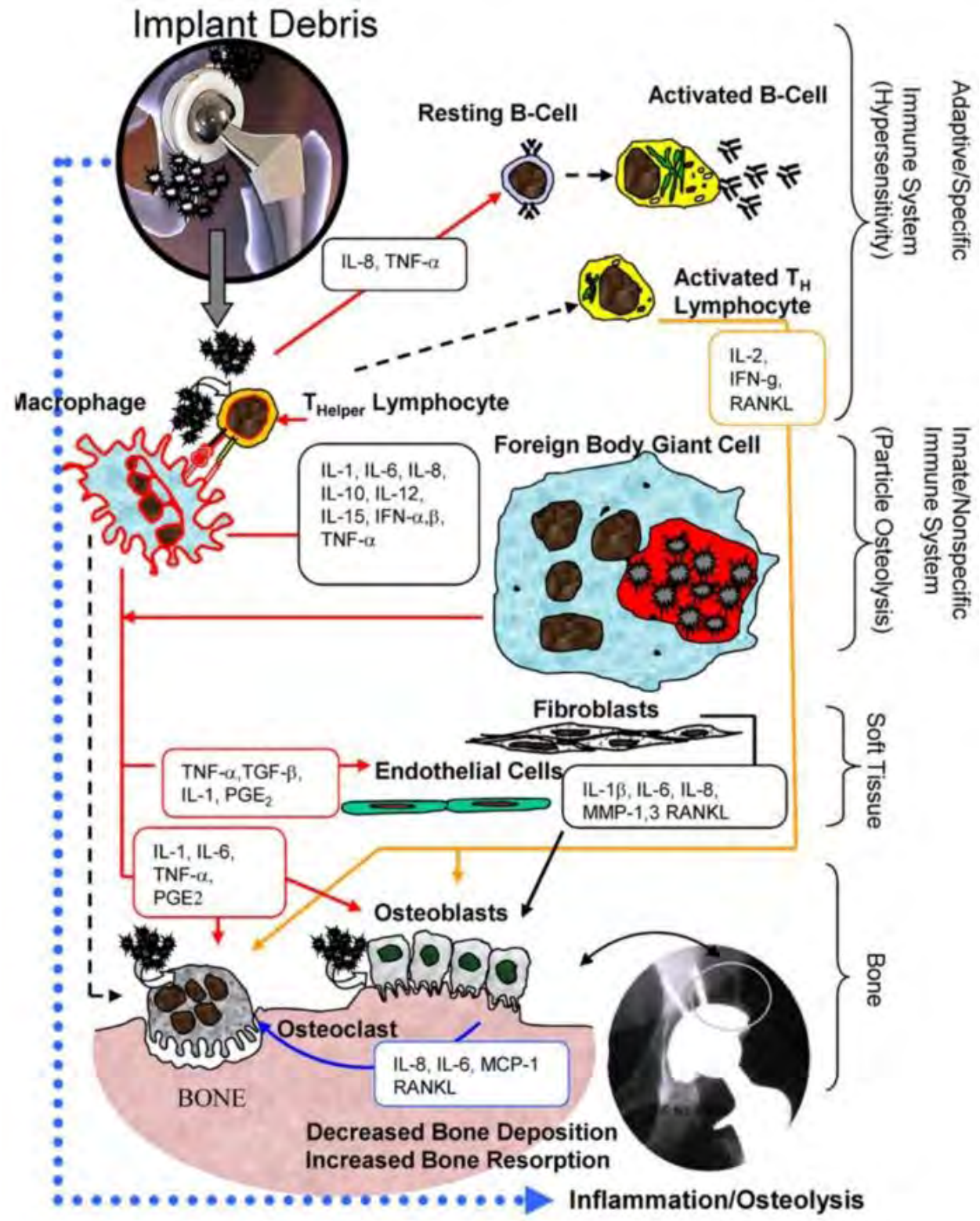

Figure 2.4: The biologic reactivity of implant debris causes local immune responses primarily mediated by macrophages, which produce reactive oxygen intermediates and pro-inflammatory

cytokines that affect a host of local cell types and induce a widening zone of soft-tissue damage and inflammation [19], [55], [74].

While corrosion per se may not be of great concern, when combined with mechanical effects, restricted crevice-like geometries, inflammation, or any combination thereof, considerably amplified corrosion rates might arise, potentially leading to adverse host response or implant failure.

In contrast to the case of metals, immune responses to biopolymers have not been reliably reported, whereas immune responses to bioceramics are unlikely thanks to their exceptionally low solubility.

2.3.4.5 Common Metallic Biomaterials and Their Corrosion Performance

Metals and alloys have an extensive range of biomedical applications, including devices for fracture fixation, partial and TJR, external splints, craniofacial plates and screws, braces and traction apparatus, dental amalgams, cardiovascular surgery (e.g., parts of artificial hearts, balloon catheters and valve replacements) and so forth. The high modulus and yield stress coupled with the ductility of metals make them suitable for high load-bearing without suffering from large deformations and permanent dimensional changes. The compositions most used for load-bearing applications include stainless steels, cobalt-based wrought or cast alloys and titanium-based alloys. In addition, the NiTi SMA has attracted much attention due to its ability to reproduce its original shape upon exposure to body temperature and its pseudoelastic properties ($\mathbf{E}_{\text{eff}} \sim 40$ GPa), which enable, among others, the manufacture of low-stiffness, high spring back, orthodontic wires. Dental implants are frequently manufactured from CP-Ti or titanium alloys, amalgams, and precious metals (e.g., Au). Noble metals such as Pt and Pt-Ir are also used as electrodes in cardiac pacemakers and other neuromuscular stimulatory devices. Copper is used in intrauterine contraceptive devices (IUDs). Magnesium and some other biodegradable metals are considered for bone screws and stents. Small metallic medical devices are used in many other implants, including skin and wound staples, vascular endoprostheses, filters, and occluders. Although metals exhibit high strength and toughness, they have several drawbacks: high modulus of elasticity, E (which might cause stress shielding of bone), and susceptibility to chemical and electrochemical degradation. This susceptibility is usually increased by the action of applied forces and wear. The combination of a relatively corrosive environment and a poor body tolerance to even small concentrations of most metallic corrosion products exclude most metallic materials. This section will discuss the primary metals and alloys currently used as biomaterials. Obviously, given the page limitation and the sizeable global RandD activities in this field, it is impossible to discuss them all. Yet, similar corrosion characterisation and control approaches may be applied to other metals and alloys.

Stainless Steels

the first stainless steel explicitly developed for implantation was the “vanadium steel” in the early 1900s. The early successful devices were fracture fixation plates. However, the surgeons quickly learned that these devices failed due to mechanical corrosion and poor biocompatibility. Iron and steel were found to dissolve rapidly in vivo and caused erosion of the adjacent bone. Thus, an 18Cr–8Ni stainless steel was introduced in 1926 and exhibited improved strength and corrosion

resistance. Later that year, Mo was added to this steel to improve its localised corrosion resistance; this alloy became 316 stainless steel. In 1943, type 302 stainless steel was recommended to the U.S. Army and Navy for bone fixation [9], [75]. During the 1950s, the carbon content was reduced to 0.03 wt%; this alloy is 316L stainless steel (UNS *S31673*). Because type 316L stainless steel is more corrosion resistant in vitro and in vivo than type 316, ASTM recommends the former for implant fabrication.

Austenitic stainless steels have an fcc (γ) structure unless they undergo a phase transformation due to severe plastic deformation. Chromium soluted evenly within the microstructure allows forming a thin (typically 10–50 Å thick), amorphous chromium oxide (Cr_2O_3) layer on top of the steel. The ionic bonding in this layer protects the surface from electrochemical degradation. Hence, stainless steel is often pickled in nitric acid to enhance the growth and thickening of this passive layer. Austenitic stainless steels are used either in the annealed or cold work state. The latter improves the tensile strength and fatigue properties, with some trade-off in corrosion resistance. Advantages of stainless steel include high strength, availability, cost-effectiveness, and good formability (namely, good cold work, machinability, and weldability). Shortcomings, on the other hand, include the possible release of toxic ions (namely, Cr and Ni) due to the combined action of corrosion and wear and stress shielding of adjacent bone due to the high modulus of elasticity (**E** ~ 190 GPa), which is about ten times that of bone. Consequently, stainless steel is used mainly as temporary medical devices or in elderly patients.

Hanawa [13], [17], [76] discussed the chemical composition and reconstruction of the oxide films on austenitic stainless steels briefly. The document was found to comprise of Fe and Cr, small amounts of Mo but no Ni. After mechanical polishing in water, the surface of 316L consisted of iron and chromium oxides containing small amounts of Ni, Mo, and Mn oxides. The surface oxide also contained a large amount of $(OH)^-$. Following immersion in Hank's solution and incubation with cells, CaP was formed on and within the film. Sulfate was also adsorbed on the surface of the oxide film and was reduced to sulfite and/or sulfate in the cell culture medium.

Stainless steels are susceptible to pitting corrosion in saline. Depending on the type of alloy used, the pitting potential of stainless steels may be set in a potential region relevant to biomedical applications.

The corrosion performance of stainless steel has been investigated both in vitro and in vivo. It was found that only one antibiotic, oxytetracycline, exerted a significant effect on the electrochemical behaviour, generating an anodic shift of 120–250 mV in $\mathbf{E}_{corr}$. Shih et al. [57] showed that while the amorphous oxides on either 316L stainless steel or Nitinol wire were resistant against localised corrosion both in vitro and in vivo, their counterpart polycrystalline oxides experienced severe pitting or crevice corrosion. Sutow et al. [47] showed that the in vitro crevice corrosion of cold-worked 316LVM steel could be reduced following passivation in 30% HNO_3. Bundy et al. [8], [48]conducted in vitro tests and showed that cyclic anodic polarisation tests with highly loaded fracture mechanics samples resulted in a lower $\mathbf{E}_b$ and disruption of the passive films. The current density increased by more than an order of magnitude in the presence of plastic deformation, compared to loading to below yield stress. Brown and Merritt [37], [62]studied the fretting

corrosion of stainless-steel plates in vitro. The results showed a tenfold decrease in fretting corrosion when 10% solution of fetal calf serum was added to saline. In a later publication, proteins increased the corrosion rate of 316L in the static mode while decreasing the corrosion rate in a fretting way. The presence of proteins caused an increase in the anodic Tafel constant and decreased the cathodic Tafel constant of this material.

During the last decades, the role of sulfide inclusions in initiating pitting corrosion in stainless steels was recognized [3], [8], [24], [29], [33], [37], [43], [75], [77]–[79], leading to the development of type 316LVM stainless steel. This steel is vacuum melted (VM) to reduce the non-metallic inclusions content. Because biomaterials are more prone to localised corrosion in dental applications, a further improvement has been made, forming ultraclean high nitrogen austenitic stainless steels. Adding nitrogen to 316L stainless steel increases the PREN of this alloy to above 26 and increases the ultimate tensile strength (UTS). However, the trade-off is some loss of ductility (as observed by elongation to fracture).

Mudali et al. [19], [56] identified different failure mechanisms in stainless steel orthopaedic devices and suggested routes to improve the corrosion behaviour of these steels. Alloy modification was carried out by adding titanium and nitrogen as alloying elements. A super-ferritic stainless that was commercially introduced in 1979 to provide high strength and high resistance against localised corrosion and SCC in seawater was also characterised for comparison. A second comparison was made to SAF 2205 (UNS S31803) duplex stainless steel [42]. This steel acquires a ferrite/austenite two-phase microstructure and is characterised by good weldability and an attractive combination of high strength, high toughness, and excellent corrosion resistance (PREN = 35; high resistance to SCC in chloride-bearing environments, as well as to erosion corrosion and corrosion fatigue). The resistance of the different stainless steels to pitting corrosion was ranked as follows: super-ferritic > duplex > 316L with 1600 ppm nitrogen > 317L with 1410 ppm nitrogen > 317L with 880 ppm nitrogen > 316L with 680 ppm nitrogen > Ti-modified 316L > reference 316L. With respect to crevice corrosion resistance, however, the order slightly changed, as follows: super-ferritic > duplex > 317L with 1410 ppm nitrogen > 316L with 1600 ppm nitrogen > 317L with 880 ppm nitrogen > 316L with 680 ppm nitrogen > Ti-modified 316L > reference 316L.

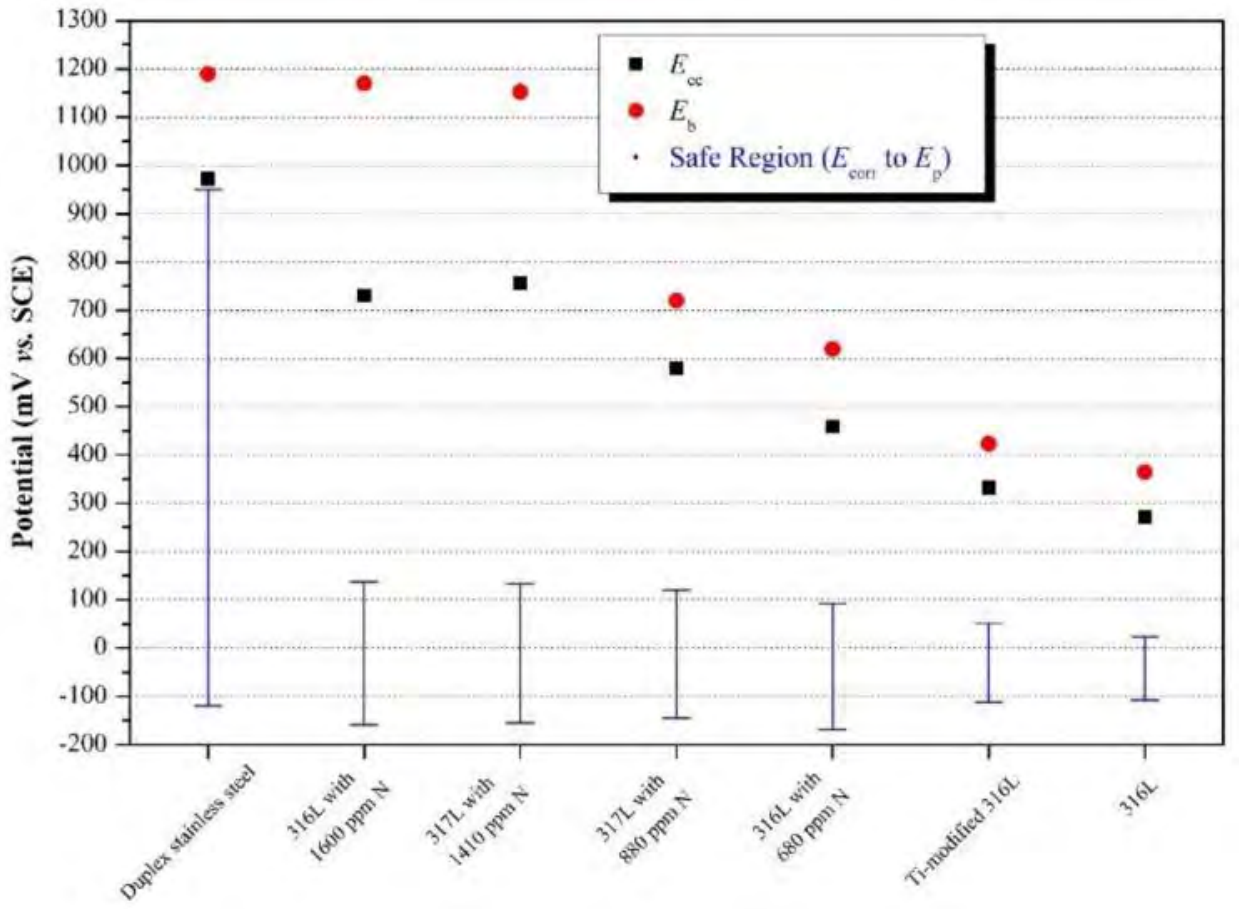

Figure 2.5: Comparison between selected corrosion resistance characteristics of several stainless steels in Hank's solution, illustrating the effect of nitrogen concentration in the steel.

Advanced stainless steels for surgical implants include the low-nickel (or nickel-free) austenitic stainless steels [*151*]. One example is UNS S29108 [*152*], also known as BioDur® 108, from Carpenter Technology Corporation (see *Table 2.5*). This alloy was designed to minimise problems associated with Ni toxicity and is produced by the electro-slag re-melting (ESR) process to guarantee its microstructural integrity and cleanness. It has better mechanical properties (both static and fatigue) and localised corrosion resistance than type 316L alloy.

Cobalt-Chromium Alloys

The industrial use of pure cobalt dates to the 20th century. However, it is not sufficiently ductile and corrosion-resistant in the form of pure metal. Between 1907 and 1913, Haynes developed a series of cobalt-chromium and cobalt-chromium-tungsten alloys with good corrosion resistance. During the early 1930s, an alloy called Vitallium, with Co–30Cr–7W–0.5C, was used to prepare metallic dental castings. Since these alloys were marketed in dentistry as an alternative to the expensive gold ones, the dentists quickly adapted them widely, particularly for tsizeablerge partial denture castings requiring considerable metal. More recently, cast Vitallium started to find use

also in artificial joints. Wrought Vitallium is used to manufacture the stems of heavily loaded joints, such as femoral hip stems. Porous coated Co–Cr implants have been extensively used for bone ingrowth applications. Different coatings applied on Co- Cr orthopaedic implants are sintered beads, plasma flame, sprayed metal powders, and diffusion bonded fibre metal pads [*74*,*75*].

Cobalt-based alloys are highly resistant to corrosion, including chloride-induced crevice corrosion. Galvanic corrosion is also of less concern compared to stainless steel. Cobalt-based alloys are relatively resistant to fatigue and environment-induced cracking (EIC). They have reasonable toughness and elongation of more than 8% to fracture. However, wear processes can lead to toxic Cr, Co, and Ni ions releasing into the body. Another drawback of these alloys is their high modulus of elasticity, enhancing stress shielding compared to other alloys, including stainless steel and titanium-based alloys.

Hanawa [13], [76] described the composition of the surface oxides on CoCrMo alloys. Typically, these are oxides of Co and Cr without Mo. However, after mechanical polishing in DI water, there were also oxidic species of Mo, and the overall film thickness was about 2.5 nm. The surface film also contained high $(OH)^-$ content; it was hydrated or oxyhydroxide. After dissolution in Hank's solution, the surface oxide consisted of chromium oxide (Cr^{3+}), which contained molybdenum oxides (molybdenum having +4, +5, and +6 valences). Chromium and molybdenum were more widely distributed in the inner layer than the outer layer of the oxide film. It was also argued that Co is entirely dissolved in body fluids, and the surface oxide converts to chromium oxide containing a small amount of molybdenum oxide. CaP is also formed on the top surface.

There are two primary cobalt-chromium biomedical alloys–cast CoCrMo and wrought CoNiCrMo alloys. While the former has been used for years in dentistry and more recently in orthopaedics (for TJR), the latter is used for manufacturing hip stems and knee joints. The abrasive wear properties of the wrought alloy are like those of the cast alloy. However, the superior fatigue and UTS of the wrought alloy make it suitable for applications that require long service life without fatigue or fracture. The CoCrMo alloy is particularly susceptible to work hardening; hence, the standard manufacturing procedures selected for other metals are not applicable.

Titanium Alloys

Titanium and its alloys are the most widely used materials for medical implants. Titanium is light ($\boldsymbol{\rho}$ = 4.51 $g \cdot cm^{-3}$), biologically and chemically inert, biocompatible and has low electrical and thermal conductivity ($\boldsymbol{\sigma}$ = 2.3 × 10^4 $\Omega^{-1} \cdot cm^{-1}$ at 22 °C, $\boldsymbol{\kappa}$ = 22 $W \cdot m^{-1}$ K^{-1} at 27 °C, respectively) in comparison to other metals. Since it is weakly paramagnetic, image interference in magnetic resonance imaging (MRI) or computed tomography (CT) scan is not observed. In addition, MRI testing complications due to thermal expansion and distortion are minimised because it has a coefficient of thermal expansion like that of the bone. The modulus of titanium and its alloys elasticity is closer to the bone than the moduli of stainless steel and cobalt-based alloys. Thus the concern over stress shielding is reduced. The oxide layer on the titanium surface and its alloys is formed due to the high affinity of titanium to oxygen, provides corrosion resistance and allows for histological osseointegration. This oxide layer, typically several nanometres thick, is thermodynamically stable and repairs itself rapidly if there is a low concentration (several ppm) of

oxygen or water in the environment. However, because osseointegration of titanium implants takes a long time (typically three to six months), they are often coated with hydroxyapatite (HAp) and other calcium phosphates [9], [14], [19], [21], [22], [31], [55], [58], [65], [80].

Typical mechanical properties of selected Ti-based alloys are summarised in Table 2.6 compared to some other common biomaterials.

Table 2. 5- Mechanical properties of selected biomaterials.

Material	**UNS Designation**	**σ_{UTS} (MPa)**	**σ_{YP} (MPa)**	**E (GPa)**	**ε (%)**
316L, annealed	S31673	min 490	min 190	190	min 40
316L, cold worked	S31673	min 860	min 690	190	min 10
BioDur® 108 stainless steel, annealed	S29108	min 827	min 517	--	min 30
Co-28Cr-6Mo, as-cast	R30075	min 655	min 450	210	min 8
Co-28Cr-6Mo, forged	R31537	min 1172	min 827	210	min 12
Co-20Cr-15W-10Ni, annealed	R30605	min 860	min 310	210	min 30
Co-35Ni-20Cr-10Mo, solution annealed	R30035	793–1000	241–448	232	min 50
CP-Ti, grade 1	R50250	min 240	min 170	110	min 24
CP-Ti, grade 4	R50700	min 550	min 483	110	min 15
Ti–6Al–4V ELI, annealed	R56401	min 825	min 760	116	min 8

Ti–6Al–7Nb, annealed	R56700	min 900	min 800	114	min 10
Ti–13Nb–13Zr, capability aged	R58130	min 860	min 725	75	min 8
Ti–12Mo–6Zr–2Fe, solution-annealed	R58120	min 932	min 897	74–85	min 12
Ni-Ti, annealed	--	min 551	--	40	min 10
Cortical bone	--	70–150	30–70	10–30	0–8

Titanium and its alloys are used in various applications, including fracture fixation devices (plates and screws), spinal fixation devices, THR femoral components, ligament anchorage screws, dental implants, and maxillofacial surgery heart pacemaker housings and artificial heart valves and components in high-speed blood centrifuges. Generally, alloys are used for joint replacement components because of their better mechanical properties than CP-Ti.

The Ti–6Al–4V alloy combines good workability, heat treatment ability, weldability, high corrosion resistance, high strength, and good biocompatibility. Interstitial atoms such as oxygen, nitrogen, and carbon significantly increase the power, nitrogen having an almost double effect per atom. The extra-low interstitials (ELI) grade, containing small amounts of oxygen, carbon, nitrogen, and hydrogen, is commonly used for biomedical applications (e.g., for stems of artificial hip joints). The Ti–6Al–4V ELI alloy has excellent toughness because the impurities decrease the fatigue strength with a notch effect. Its yield strength in the forged and annealed condition is very high (896 MPa), much higher than that of 316L stainless steel (331 MPa) or wrought Co-Cr alloys in the annealed condition (448–648 MPa), making plastic deformation of the titanium alloy limited even under a large load.

Drawbacks of titanium and its alloys include high price, high susceptibility to friction and wear (as reflected by a high coefficient of friction), and low shear strength. Machining of titanium is not cost-effective. Although precision casting reduces the manufacturing costs, cast titanium alloys exhibit low fatigue strength and low elongation compared to wrought alloys due to the coarse microstructure of the cast alloys. Therefore, supplement microstructural refinement is often required to improve the mechanical properties while preserving the product's shape. Thermomechanical processes with post-heat treatment have increased the strength, elongation, and fatigue of $\alpha + \beta$ titanium alloys. Another cost-effective process is powder metallurgy (PM). This

process is beneficial in producing more homogenous β alloys containing alloying elements with high melting points, such as Nb and Ta [31], [78].

The presence of Zr and Nb in titanium has been found to significantly reduce the modulus of elasticity and improve the corrosion resistance in vivo. In 1986, the dual-phase Ti–6Al–7Nb was introduced into clinical use (this alloy was first synthesised in 1977) as a possible alternative for Ti–6Al–4V, realising that Nb is both cheaper and more biocompatible than V. In this regard, VO_2 generated by passivation of the metal surface is thermodynamically unstable; some V could be released into the human body and cause toxic effects. Ti–6Al–7Nb has been produced by casting, hot rolling, hot forging, and PM methods. Current applications of this alloy include artificial hip and knee joints, bone plates, screws for fracture fixation, dental applications, cardiac valve prostheses, pacemakers, and artificial hearts.

Another alloy, Ti–13Nb–13Zr, exhibits higher adhesion of osteoblasts and lower bacterial adhesion than CP-Ti and Ti–6Al–4V. This alloy helps design cardiovascular implants because the ZrO_2 passive film is thrombogenically compatible with blood. The corrosion resistance of this alloy is also improved due to the presence of ZrO_2 and Nb_2O_5, which strengthen the TiO_2 film formed on the surface.

The $\mathbf{E}_{corr}$ of the titanium alloy is nobler than that of 316L stainless steel and Co-based alloys, and the material enters a stable passive behaviour directly from the active regime without exhibiting an active-to-passive transition.

An interim summary of the corrosion characteristics of stainless steels, Co-based alloys and Ti-based alloys can be made with the aid of a study of Gurappa [16]. 316L stainless steel, Co-Ni-Cr-Mo alloy, CP-Ti, Ti–6Al–4V, and a new Ti-based alloy (IMI 834) containing Al, Sn Zr, Nb, Mo, and Si, were tested in deaerated Hank's solution at 37 °C. Figure 2.6a shows the OCP of these materials, while Figure 2.6b shows their cyclic polarisation curves. The OCP is the working electrode's potential relative to the reference electrode when no potential or current is applied to the cell. The OCP is also the equilibrium potential in a reversible electrode system. Otherwise, it is called the resting potential, $\mathbf{E}_r$, or the corrosion potential, depending on the studied system. Metals with nobler (more positive) OCP are more thermodynamically stable than those with more negative OCP; the former will be less susceptible to uniform corrosion. The first step in most electrochemical tests is to measure the OCP. Before beginning the following experimentsteady-state, the OCP can reach a steady-state (which indicates that the various corrosion reactions have assumed a constant rate). This could take between minutes and days. From Figure 2.6a, it is thus evident that for all materials, the formation of a passive film is prominent from the shift in the positive direction of the OCP over time. Hysteresis loop in the potentiodynamic curve is evident only in 316L stainless steel, indicating its high susceptibility to pitting and crevice corrosion.

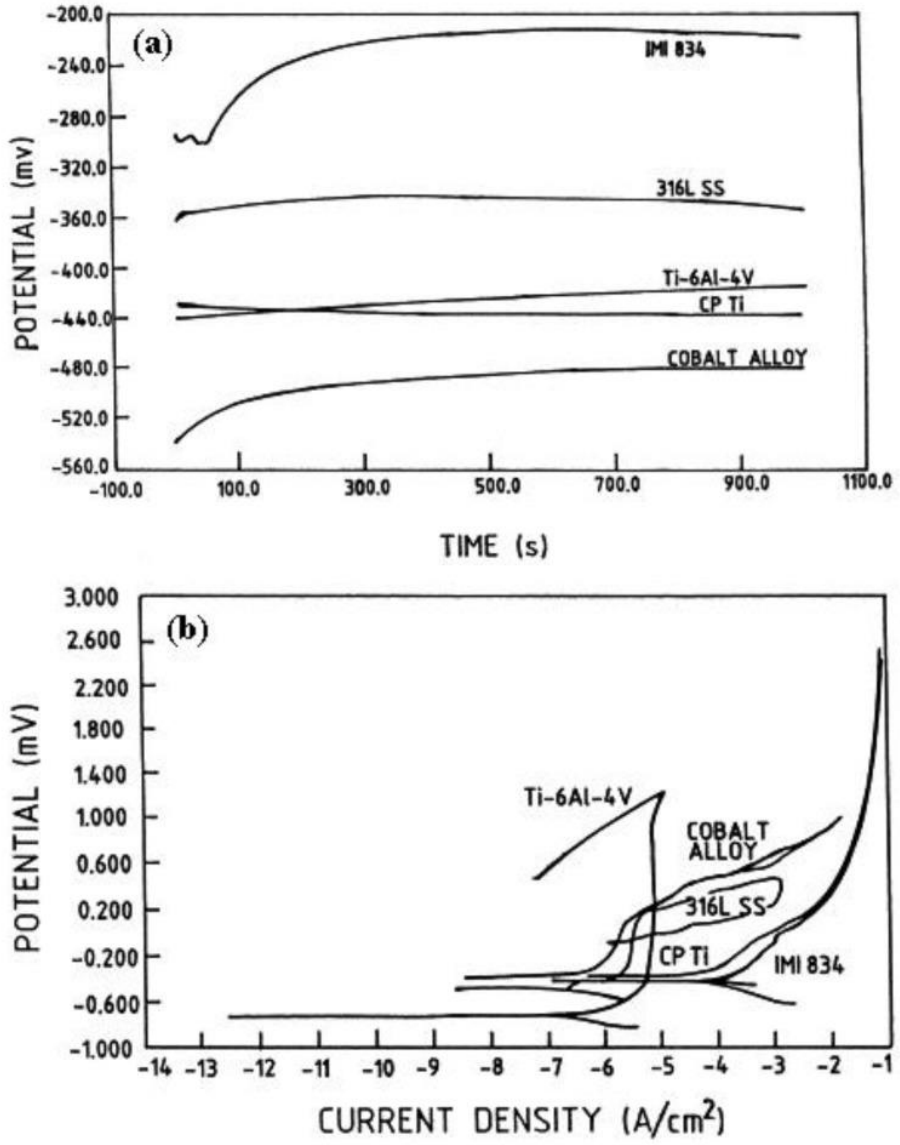

Figure 2.6: (a) OCP versus time and (b) cyclic potentiodynamic polarization curves of 316L stainless steel, Co-Ni-Cr-Mo alloy, CP-Ti, Ti–6Al–4V, and IMI 834 T-based alloy. Tests were conducted in deaerated Hank's solution at 37 °C [185] and reprinted with the permission of Elsevier.

When exposed to synthetic physiological solutions, titanium naturally forms a few nanometres thick passive film, containing a relatively high concentration of oxygen vacancies. A freshly abraded titanium surface immediately passivates, forming low-crystalline rutile and anatase oxide layer. The oxygen concentration in the titanium oxide gradually decreases, from TiO_2 at the outer surface to Ti_2O_3 and TiO closer to the metal/oxide interface. Depending on the environment, this oxide may be covered with an amorphous or hydrated surface oxide, thus exhibiting a bilayer oxide

structure. The thickness of the oxide layer can be increased by anodising or thermal oxidation. The former process can yield an oxide layer several thousand angstroms thick, depending on the applied potential [5], [23], [40], [54], [63], [81], [82].

The environment's temperature plays a significant role in the incidence of crevice corrosion of Ti and its alloys. The critical temperature for crevice corrosion is typically observed at around 70 °C. Nevertheless, at 37 °C, the degradation behaviour changes compared to room temperature. For example, the passive dissolution rate in neutral physiological saline solutions was found to slightly increase in the case of Ti–6Al–4V alloy (in contrast to CP-Ti) at body temperature compared to room temperature. In more aggressive acidic solutions, the temperature effect is even more distinct because, at a higher temperature, less acidic solutions can result in surface activation; in this regard, the product is more substantial for the Ti–6Al–4V alloy than for CP-Ti. Temperature increase also has a very pronounced effect on the metastable pitting activity of CP-Ti and Ti–6Al–4V. It should be noted that, at 37 °C, the frequency of pit nucleation does not decline to zero over time; hence, during long-term exposure, even a few activation/passivation events could cumulatively contribute significantly to metal ion release, apart from influencing the passive dissolution behaviour, raising the temperature to 37 °C influences the adsorption of Ca^{2+} and PO3−4 ions on the surface of passive Ti or Ti alloys. It is thus evident that to assess Ti alloys' chemical, electrochemical, andbehaviourtion behaviour properly, experiments should be conducted at 37 °C couplings of either CP-Ti or Ti–6Al–4V with seven different Au-, Ag-, Pd- or Co–Cr-based dental alloys. In all cases, the level of corrosion was found low.

Nitinol Shape Memory Alloy (SMA)

What makes the NiTi SMA unique is its ability to exist in two different reversible crystalline phases in its solid state at clinically useful temperatures: the austenite (A) phase prevails at a higher temperature, whereas the martensite (M) phase prevails at a lower temperature. A gradual transition between the A and M phases occurs between these two temperatures. The phase transformation takes place by sheer lattice distortion. Each martensite crystal has two different forms: twinned martensite and detwinned martensite. When martensite NiTi is heated, it starts transforming into austenite. The temperature at which this transformation begins is called austenite start temperature, $\mathbf{A}_s$. The temperature at which this transformation is completed is called austenite finish temperature, $\mathbf{A}_f$. When austenite NiTi is cooled, it starts transforming to martensite. The temperature at which this phenomenon begins is called martensite start temperature; Ms. The temperature at which martensite is completely reverted to martensite is called martensite finish temperature, $\mathbf{M}_f$. The temperature range for the martensite-to-austenite transformation upon heating is higher than for the reverse transformation upon cooling. Hysteresis is the difference in the transition tempers upon heating and cooling. In practice, an alloy designed to be completely transformed by body temperature upon heating ($\mathbf{A}_f < 37$ °C) would require cooling to about 5 °C to fully retransform into martensite ($\mathbf{M}_f$). Composition and metallurgical treatments have intense effects on these transition temperatures [8], [43], [71], [72], [83].

NiTi can have three different forms concerning real biomedical applications: martensite, stress-induced martensite (superelastic) and austenite. Martensitic NiTi is soft and ductile and easily

deformed, superelastic NiTi is exceedingly elastic (rubber-like), and austenitic NiTi is relatively robust, hard and rigid (similar to titanium). The NiTi alloy combines all these properties, their exact manifestation dependent on the temperature at which it is used. The SME, superelasticity and sound damping properties make the NiTi SMA an attractive material for surgical applications, such as self-locking, self-expanding and self-compressing implants [71], [72].

The term shape memory effect (SME) [71] reflects the ability of an alloy to revert its original shape following deformation at low temperatures and subsequent heating above its transition temperature. This effect is based on the temperature-dependent austenite-to-martensite phase transformation on an atomic scale. As can be seen in Figure 2.7, the SME occurs when the SMA is deformed in the twinned martensite phase and unloaded while at a temperature below $\mathbf{M}_s$. While having this martensitic phase, the SMA can accommodate a significant amount of plastic strain, which results from the low-stress plateau, and then displays high residual strain upon unloading. Subsequently, when the SMA is heated above $\mathbf{A}_f$, it will recover its original shape by phase transformation from detwinned martensite to austenite. The SMA will regain the twinned martensite structure upon cooling, thus completing one phase transformation cycle due to the SME [72], [83].

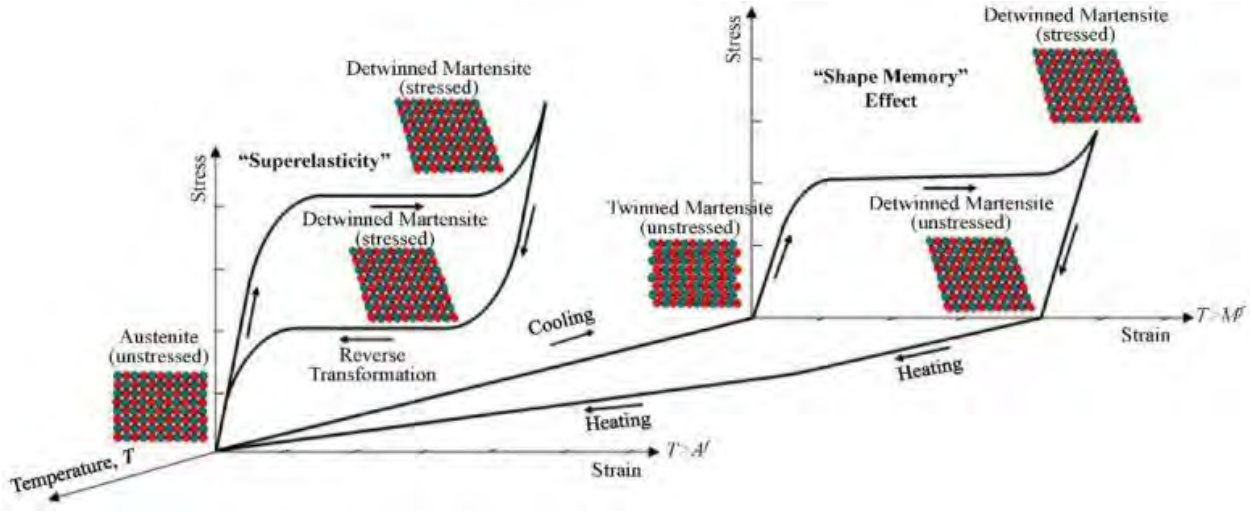

Figure 2.7: Stress-strain–temperature diagram of SMAs, illustrating both the shape memory and superelasticity phenomena.

Nowadays, most self-expanding implants such as stents and filters employ the thermal SME of Nitinol to allow deployment into the body. The implant is usually compressed at low temperature to fit into a delivery catheter. It is not essential to retain the implant cold during introduction into the body since it remains constrained inside the delivery catheter to avoid early release. The original shape of the implant is restored when it is released and reaches body temperature [7], [55], [57], [60], [61].

Nitinol thus has remarkable advantages in applications requiring kink resistance, flexibility, crush resistance, constancy of applied stress and significant expansion or deformation ratios. Most Nitinol stents are superelastic at body temperature and can be crushed fully flat and still recover

their original shape. Superelasticity is a significant feature in treating superficial vessels, such as carotid and femoral arteries, subjected to external crushing. To date, the most successful medical applications of Nitinol using the superelasticity property are guidewires, baskets, snares, needles, coils, soft tissue anchors, intramedullary canal reamers, anastomotic devices, self-expanding stents and stent-grafts, filters and occlusive distal protection devices and several catheters used for radiofrequency ablation, brachytherapy, atherectomy, thrombectomy and laser therapy [7], [43], [55], [57], [72].

Some unique properties of NiTi may be valuable in surgery. NiTi is capable of being vastly damped and vibration-attenuated below $\mathbf{A}_s$. In orthopaedics, this property can be helpful, for example, for dampening the peak stress between bone and an articulating implant. The low elastic modulus of NiTi (**E** ≅ 40 GPa, much similar to that of bone than any other metallic biomaterial) may also be beneficial. NiTi possesses enhanced fatigue and ductility properties and very high wear resistance. It is nonferromagnetic and has lower magnetic susceptibility than stainless steel; therefore, it generates fewer artefacts during MRI examination. The mechanical properties of NiTi are susceptible to the chemical composition and the thermomechanical history. Typical chemical composition is provided in Table 3, whereas typical mechanical properties are given in Table 4.

Due to the high nickel content of NiTi, a concern has been raised that nickel ions might be released from this alloy due to corrosion and cause undesirable effects. Fortunately, however, the surface of NiTi consists mainly of TiO_2, smaller amounts of NiO and Ni_2O_3 and metallic Ni, while nickel-titanium constitutes the inner layer. Because its surface oxide is primarily TiO_2, Nitinol is sometimes regarded as a Ti alloy [*45*]. The thickness of the oxide layer is between 2 and 20 nm. During implantation, this oxide layer grows and picks up minerals (e.g., CaPs) and other constituents of biofluids, which results in remodelling of the surface. Several surface treatments have been employed to enhance the corrosion properties of NiTi, including titanium nitride coating processes by an arc ion plating method, chemical modification with human plasma fibronectin via aminosilane and glutaraldehyde as coupling agents, plasma-polymerized tetrafluoroethylene (PPFTE) coating, laser surface treatment, electropolishing and nitric acid passivation [45], [47].

Most of the information on the corrosion behaviour of NiTi stems from investigations of dental archwires under in vitro conditions. Although more studies and for longer exposure periods, are still necessary, the resistance of NiTi to pitting corrosion is apparently similar to (or better than) 316L stainless steel [8], [13], [14], [16], [25], [46], [47], [76]. NiTi induces no toxic effects, decrease in cell proliferation or inhibition in the growth of cells in contact with the metal surface. The muscular tissue response to NiTi was non-toxic and non-irritating, as were also the neural and perineural responses. The overall inflammatory response and the presence of immune cells, macrophages and foreign body giant cells were like those around 316LVM stainless steel, CP-Ti and Ti–6Al–4V. After eight-week implantation, histomorphometry revealed that the fibrous capsule around NiTi was thicker than around stainless steel. However, at 26 weeks post-surgery, the capsule thickness was the same. Determination of trace metals in several distant organs showed no statistically significant differences in Ni concentration between the NiTi and 316LVM stainless steel. Thus, Ryhänen concluded that the biocompatibility of NiTi is like or better than that of

stainless steel or Ti–6Al–4V alloy. Yet, it was recommended that when NiTi is intended to be used in long-term implants, an optimal surface treatment should be considered [10], [41], [84].

Some surface modification processes have been shown to improve the corrosion performance of Ni-Ti alloys and avert nickel dissolution. These include titanium nitride coating and chemical modification with coupling agents to improve corrosion resistance. Nevertheless, when the coating on a Ni-Ti alloy is damaged, corrosion is accelerated compared to an uncoated alloy. Laser surface treatment of Ni-Ti leads to an increase in the oxide layer's superficial titanium concentration and thickness, improving its cytocompatibility to CP-Ti. Electropolishing and nitric acid passivation can improve the corrosion resistance of Ni-Ti alloys thanks to the enhanced uniformity of the oxide layer [17], [84], [85]

Dental Amalgams

In widespread use for over 150 years, dental amalgams are among the oldest materials used in oral healthcare. They are still the most useful restorative material for posterior teeth. They are formed by mixing liquid mercury (45–55 wt% Hg) and a powder made of Ag, Sn and Cu (sometimes–also smaller amounts of Zn, Pd, In or Se). Mixing occurs via mechanical vibration and results in a putty-like material that is easy to manipulate (e.g., filling cavities). Dental amalgam has been broadly used as a direct filling material due to its advantageous mechanical properties, low cost, and easy placement. Amalgams possess high compressive strength and high dimensional stability; however, shrinkage and corrosion remain of concern [7], [8], [23], [59].

The oral environment triggers corrosion. The mouth is permanently moist and is routinely subjected to temperature variations. Food and liquids ingested have a wide pH range. Acids are released during the breakdown of foodstuffs. Dental alloys with high contents of Au and other precious metals, used for crowns and inlays amalgams, have high corrosion resistance in almost all oral environments. An exception may be when high fluoride levels develop in the mouth during some dental cleaning procedures. In some patients, both Ag- and Au-based alloys might undergo tarnishing, in which a thin black layer (most likely a sulfide) grows across the surface [7], [22], [69], [86]. In the oral cavity, tarnish frequently results from hard and soft deposits on the restoration surface. The soft deposits are plaques and films consisting mainly of microorganisms and mucin. Surface discolouration may also occur on metal due to the formation of thin films, such as oxides or sulfides. Tarnish is an early sign of corrosion. Amalgam restorations often tarnish and corrode in the oral environment. Corrosion of dental amalgam may establish galvanic couples. Ion release due to corrosion is of most sig significant importance. Humans are exposed to mercury and other dental metals via vapour or corrosion products in swallowed saliva and direct absorption into the blood from oral mucosa. In recent decades, the use of dental amalgam has been considered regarding the potential toxicity of mercury components. The main toxic effects are neurotoxicity, kidney dysfunction, reduced immunocompetence, oral and intestinal bacterial flora, foetal and birth effects, and general health. The clinical challenge is that corrosion often occurs below the surface of restorations. Evaluating the internal corrosion state of an amalgam restoration is challenging for current clinical diagnostic tools and techniques. Instead, alleged recurrent decay is the dominant reason for replacing amalgam restorations [59], [87].

Several sulfides, including hydrogen sulfide or ammonium sulfide, corrode silver, mercury and other metals in the amalgam. Water, oxygen, and chloride ions are present in saliva and accelerate the corrosion attack. Various acids such as phosphoric, acetic, and lactic are sometimes present. At the right concentration and pH, these can result in corrosion. Ions may play a vital role in the corrosion of certain alloys. For example, oxygen and chlorine are involved in the corrosion of amalgam at the tooth interface and within the bulk of the alloy.

Because dental amalgams are multiphase alloys, localised, galvanic or intergranular corrosion between the different phases might develop [64]. In the conventional silver amalgams, the Ag-containing phases are nobler and accelerated corrosion attacks the γ_2 phase (Sn_7Hg). Corrosion results in the formation of tin oxychloride from the tin in the γ_2, releasing toxic mercury to the body. The reaction of the released mercury with unreacted γ can form more γ_1 and γ_2 [6], [8], [10], [29], [59], [69], [88]. On the other hand, the high-copper amalgams do not contain any γ_2 phase in the final set mass. Although these amalgams are also susceptible to intergranular corrosion, the most susceptible phase is η' (Cu_6Sn_5), which does not release Hg into the body when it corrodes. Yet, because the high copper content shifts $\mathbf{E}_{corr}$ to more positive values, high Hg release might still be observed. Electrochemical tests of pure phases have revealed that the Ag_2Hg_3 phase has the highest corrosion resistance, followed by Ag_3Sn, Ag_3Cu_2, Cu_3Sn, Cu_6Sn_5 and $Sn_{7-8}Hg$. The following compounds have been detected on dental amalgams in patients: SnO, SnO_2, $Sn_4(OH)_6Cl_2$, Cu_2O, $CuCl_{2.3}Cu(OH)_2$, CuCl, CuSCN and AgSCN. A galvanic shock is well known in dentistry. A postoperative pain due to galvanic shock can rarely be a real source of discomfort to the patient [7].

Hg release rates from conventional silver amalgams were similar to those from high-copper amalgams, with the preparation method being acute [7], [8]. Moreover, it was shown that, for most people, the primary source of Hg uptake is food, with less than 10% originating from dental amalgams. High-copper amalgams are processed from either a mixture of silver-tin and silver-copper alloys or a ternary silver-copper-tin alloy. The high-copper amalgams have superior clinical properties, including a higher corrosion resistance [7], [8], [69]. Nevertheless, too much copper might cause a positive shift in the corrosion potential, resulting in increased corrosion rates.

Gold

Gold and its alloys are used in electrode materials in medical devices and dentistry due to their durability, immunity to corrosion, desired electrical and thermal properties, and aesthetic appearance. Alloying of gold with copper or platinum results in increased strength, while silver is added to compensate for the colour of copper. Although gold is standard in dental cast restoration applications, it is unsuitable for orthopaedic applications due to its high density, poor strength, and high cost.

Under most environments, gold is immune to corrosion. However, introducing a small amount of chloride ion into the system allows for regions of stability of soluble gold(I)-chloride complexes, thus making it prone to corrosion. Gold(I)-chloride is volatile in aqueous environments. Analysis of antibody sensitization indicates that AuCl quickly decomposes in vivo into $AuCl_3$ [7], [59], [67], [89], [90]. From a kinetics point of view, gold exhibits a typical passive metal behaviour in

the presence of chloride. The gold corrosion rate in chlorides is a strong chloride concentration and solution velocity. These effects are attributed mainly to the depletion of chloride ions at the anodic surface, leading to a diffusion-limited current density. This suggests that the corrosion rate is unlikely to be significantly affected by cathodic reactions [21], [23], [90].

Rosenberg studied the electrochemical performance of gold membranes covering drug-filled wells in implantable drug-delivery devices. Comparisons were made between b PBS, calf serum and a rat model. Results showed that PBS solutions could match the thermodynamic environment of biological media but not the kinetics. The kinetics of gold corrosion in calf serum was significantly limited by modifying the gold surface by the media. Gold samples treated in serum and subsequently corroded in PBS exhibited similar kinetics to those in serum alone. It was suggested that the kinetic variation was primarily due to protein modification of the gold surface. Gold samples corroded in serum exhibited protein hydrogels. Gold chloride was shown to prevent the serum from modifying the gold surface.

Biodegradable Metals

The typical paradigm of metallic biomaterials entails good corrosion resistance in vivo. However, a new class of degradable materials—the so-called "biodegradable metals"—has been breaking this paradigm in recent years [36], [37], [90]. Biodegradable metals can be defined as metals expected to corrode gradually in vivo, with an appropriate host response stimulated by released corrosion products and then dissolve entirely upon achieving the goal of promoting tissue healing, with no implant residues. Thus, the main characteristics of a biodegradable metal are reasonable degradation rates and degradation modes in vivo and metallic elements that can be metabolised by the human body [5], [36], [38], [39], [81], [91].

Interest in Mg-based alloys for biomedical applications has been rapidly growing. But Mg was suggested as a biodegradable implant material in 1878 in a report about absorbable ligature for the closure of bleeding vessels. Pure iron had been used in implants long before. The first studies on biodegradable metals in the musculoskeletal field were published at the beginning of the last century based on experience with osteosynthesis implants made of Mg alloys. Metal allergies were not accounted for due to the more significant surgical complications at that time, such as infection or implant failure. Skin sensitising reactions to metal implants were described more often after the introduction of aseptic surgery and less corrosive osteosynthesis materials, such as stainless steel; they are still apparent clinically in 10–15% of all implanted metals. In contrast, biodegradable Mg alloys have demonstrated no skin sensitising potential in animal studies. Higher tensile strength and Young's modulus that is closer to that of bone make biodegradable metals advantageous for load-bearing applications compared to other biodegradable materials such as polymers, ceramics, or bioactive glasses [32], [33], [39], [41], [81].

During the last 20 years, the Mg alloy technology has been advancing, and both the mechanical and corrosion properties have been improved. Hence, the interest in degradable metals as temporary implant materials has grown. To this aim, various fundamental issues related to biodegradable metals have been investigated, for example, the selection of alloying elements, tuning of microstructural and mechanical properties, biodegradation mechanisms and the factors

affecting them, control of degradation rates and ion release profile and in vitro and in vivo biocompatibility of biodegradable metals [6], [7].

The control and adaptation of the implant degradation rate are vital since the resorption capacity of the tissue is limited. Moreover, the local physiology of the implant environment governs the maximal degradation rate of a temporary implant [36]. Many factors contribute to the corrosion of metals when implants are placed in vivo. For Mg corrosion, the most critical factor is the local pH, while Fe corrosion seems to be mainly dependent on the local oxygen concentration. Following surgery, the pH around the implant is lowered to a value of 5.3–5.6, mainly because of trauma. This process might initially accelerate the Mg corrosion, while infectious microorganisms and crevices formed between components can reduce the local oxygen concentration. Mg corrosion is commonly too fast in vivo, while the foremost challenge in Fe implants is to accelerate corrosion. A possible design of appropriate Mg alloys would decrease the initial implant corrosion by the proper alloying elements, microstructure, processing, and coating. However, it should be borne in mind that the corrosion rate would be further reduced in vivo following implantation because of adherent proteins and inorganic deposits such as CaPs. If so, an Mg implant with an initially lowered corrosion rate could eventually lead to an arresting corrosion process in vivo. Therefore, the right balance between reduced corrosion rate and guaranteed complete corrosion in vivo will establish a valuable biodegradable Mg implant; otherwise, parts of the implant might be preserved locally, acting as long-term biomaterials [21], [27].

Magnesium is essential to human metabolism and is the fourth most abundant cation in the human body. Moreover, magnesium is also a co-factor for many enzymes and stabilises the structures of DNA and RNA [6], [7], [36], [38], [41], [69]. Magnesium and its alloys are light metals with a density of about 1.74 g cm 3, 1.6 times less than aluminium and 4.5 times less than steel. The fracture toughness of Mg is higher than bioceramics such as HAp. At the same time, its elastic modulus and compressive yield strength are closer to those of natural bone than other commonly used metallic osteosynthesis materials. Moreover, magnesium has low corrosion resistance, as evident from its very negative electrochemical standard potential, $E^0 = -2.363$ V versus SHE. or $E^0 = -2.159$ V versus SHE if magnesium oxides or magnesium hydroxides are formed. According to Pourbaix [20], these potentials may be shifted if the Mg ions are complex in the corrosion layer. It is evident that magnesium carbonates and phosphates are formed during Mg corrosion under cell culture conditions; they have also been detected in the complex corrosion layer in vivo. Hence, complex Mg changes the local potential and stimulates pitting in vivo. When exposed to air, the surface of magnesium is passivated by a thin grey layer of magnesium hydroxide, which is further reduced by chemical reactions. Magnesium hydroxides are marginally soluble in water; however, severe corrosion occurs in saline SBF and in vivo, where high chloride ion concentrations of about 150 mM exist. In water, corrosion-protective magnesium hydroxide forms on the surface. Still, when the chloride concentration in the corrosive environment exceeds 30 mm, magnesium chloride becomes exceedingly soluble. Thus, severe pitting corrosion can be identified on magnesium alloys in vivo. Notably, is Mg correlatively insensitive to different oxygen concentrations around implants in different anatomical locations [56]? The overall corrosion reaction of magnesium in aqueous environments is

$$Mg+2H_2O \rightarrow Mg(OH)_2+H_2. \quad (15)$$

Magnesium corrosion can be determined in vivo using microtomography. Synchrotron-based microtomography (SRμCT) is a non-destructive method with a high density and high spatial resolution. Element-specific SRμCT allows determining the spatial distribution of the alloying elements during in vivo corrosion. The remaining non-corroded metal volume and the surface morphology can be determined by 3D non-destructive testing (3D-NDT) on a micrometre scale. [33], [50], [64], [78], [91], [92]

During the corrosion process, magnesium ions are released from the magnesium implant. These ions can be quickly removed from the body by the blood serum and the kidneys. Magnesium can also be stored in muscle (39% of total Mg) or bone (60%), which are the natural storages of the 21–35 g of elemental Mg of an average adult person who weighs about 70 kg. The concentration of magnesium ions in the ECF is maintained constant at 0.7 to 1.05 mm. While serum magnesium levels above 1.05 mM might result in muscular paralysis, hypotension, and respiratory distress, cardiac arrest happens only at exceptionally high serum levels of 6–7 mM.

In magnesium and its alloys, impurities and cathodic sites with a low hydrogen overpotential facilitate hydrogen evolution, thus causing considerable galvanic corrosion and potential local gas cavities in vivo. However, the reports of these gas cavities are ambiguous. Following subcutaneous implantation, gas cavities have been observed, whereas intranasal application exhibited no local gas build-up. This finding may be explained in terms of the diffusion and solubility coefficient of hydrogen in biological tissues. The solubility of hydrogen in tissues is affected by the content of lipids and proteins and by salinity. Still, the solubility seems to be almost independent of temperature in the physiological range in fat and oils. Viscosity and different tissue components and structures like lipids, proteins, and glycosaminoglycans influence the value of the hydrogen diffusion coefficient. Depending on the experimental setup, the diffusion coefficient may be underestimated in both stagnant and flowing media due to a boundary layer formation, which increases the effective diffusion distance. This observation may be necessary for intravascular magnesium applications. Correlating the hydrogen diffusion coefficients in various biological media with fractional water contents from about 68% to 100%, it is found that the diffusion coefficient of hydrogen increases exponentially with the increasing water fraction of the tissue. The tissue water content in animals increases from adipose tissue to skin and from bone to muscles, and humans are similar for the same tissue regardless of the species. This can explain why different corrosion rates and gas cavities were observed for Mg alloys in various anatomical implantation sites. The local blood flow and the water content of the tissue surrounding the implant are essential parameters, which need to be considered when designing biodegradable Mg alloys with a proper corrosion rate. Concurrently, it can be anticipated that local hydrogen cavities occur when more hydrogen is generated per unit time than can be dissolved in the neighbouring tissue or diffuse from the implant surface into the extracellular medium, which is renewed depending on the local blood flow. This implies that Mg alloys corrode in vivo with an appropriate corrosion rate when no local gas cavities are observed during the implantation period in a specific anatomical site [2], [36], [93].

Magnesium corrosion in vivo can be controlled by alloying, processing, and coating. The first empirical approach in biodegradable stent development has successfully led to Mg alloys containing rare-earth elements. However, a more systematic approach is necessary. For humans, it may be better to select Al-free Mg-alloy systems. In contrast, Al-containing Mg-alloys may be

used for research purposes, for example, to investigate corrosion control by certain coatings by measuring the release rate of aluminium [5], [38], [86], [92].

The second type of biodegradable metal is based on iron. Iron is an essential trace element in the human body, and due to its highly toxic potential–its pathways are heavily regulated in mammals. Iron in its Fe^{2+} state can only be absorbed in the intestine. In contrast, iron in its Fe^{3+} form should be reduced before absorption. Several other metals and ligands (e.g., oxalic acid) formless soluble iron complexes and thus inhibit iron absorption. The protein transferrin transports iron in its Fe3+ state. Approximately 70% of iron is bound to haemoglobin; the rest is myoglobin or stored as ferritin or hemosiderin. Most of the iron released from the degradation of haemoglobin and myoglobin will be reused, and only a tiny portion of ~10% will be excreted via faeces, urine, or sweat. Haemoglobin contains Fe^{2+}, forms an unstable, reversible bond with oxygen in the erythrocytes (oxyhemoglobin) and appears bright red, while the oxygen-unloaded form appears purple-blue and is called deoxyhemoglobin. If the iron in the haemoglobin is oxidised, ferrihaemoglobin (methemoglobin) is formed, which cannot bind oxygen. In erythrocytes, the methemoglobin reductase reactivates haemoglobin ($Fe^{3+} \rightarrow Fe^{2+}$). Otherwise, haemoglobin will be enzymatically degraded and eliminated from the body.

Iron is generally bound to proteins and is intensely regulated in mammals; hence, there are several known iron storage diseases. Most of these diseases are based on genetic defects and result in the pathological storage of iron in the liver, heart, skin, endocrine organs, and the reticuloendothelial system. Suppose the natural storage capacity of free iron is surpassed, and transferrin cannot bind any more iron. In that case, iron causes oxidative stress, leading to cell and tissue damage, and the excess iron will be pathologically stored in the heart, liver, and endocrine. In this case, free iron ions harm cells by forming reactive free radicals, for example, hydroxyl radicals, which have a powerful oxidation capacity. The hydroxyl radical reacts with organic molecules on the cell membrane and initiates a lipid-peroxidation process, which eventually leads to cell death [6], [7], [16], [33], [38], [44].

Thus, it is essential for biodegradable iron implants that the local storage capacity and the amount of iron released per time interval do not exceed the local and general transport and storage capacities. Moreover, iron implants may need to be used only in individuals without any iron-related disease. However, the slow degradation of an iron stent that weighs ~40 mg will unlikely cause system toxicity, taking into account the high iron load of normal blood (about 447 mg L^{-1}) [11], [12].

During the last five years, interest has emerged in biodegradable zinc and Zn-based alloys as a third type of biodegradable metals for the fabrication of degradable stents and orthopaedic implants [31], [32], [38], [94], [95]. This is due to their excellent biodegradability, absorbability, and adaptability to tissue regeneration [13], [36], [44] and because their corrosion rates are between those of iron and magnesium in physiological conditions. Zinc and magnesium are chemically similar in that both elements have only one oxidation state (+2), and both cations are of equal size (0.74 and 0.72 Å, respectively). Zn^{2+} is well regulated within physiological systems and plays a critical role in numerous fundamental cellular processes [7], [37], [96]–[99]. Zinc is an antioxidant and an endothelial membrane stabiliser. The maximum daily intake of Zn is 10 mg per day for adults [6], [77], [81], [100], [101], although some variance may be found in the literature. Zn^{2+} released from an implant may suppress harmful smooth muscle cells and restenosis in arteries

while stimulating beneficial osteogenesis in bone [7], [37], [41]. In addition, it can inhibit acute inflammation and increase the expression of collagen and VEGF in colorectal tissues. The toxicity of and tolerance to zinc and its alloys depend considerably on the type of biological cells and zinc concentration. Concerning mechanical properties, porous zinc has recently been prepared using spark plasma sintering and exhibited both compressive yield strength and compressive modulus similar to those of trabecular bone [7], [33], [37], [102]. It can thus be concluded that Zn-based biodegradable metals may become more attractive than magnesium and iron to fabricate specific medical devices. However, further research is required to comprehensively tailor their corrosion rates and mechacharacteriseties and characterise their biocompatibility and toxicity in different anatomical sites.

Type of Corrosion	Material	Implant Location	Shape of the Implant
Pitting	304 SS, Cobalt based alloy	Orthopedic/ Dental alloy	
Crevice	316 L stainless steel	Bone plates and screws	
Stress Corrosion cracking	C0CrMo, 316 LSS	Only in *in vitro*	
Corrosion fatigue	316 SS, CoCrNiFe	Bone cement	
Fretting	Ti6Al4V, CoCrSS	Ball Joints	
Galvanic	304SS/316SS, CoCr+Ti6Al4V, 316SS/Ti6Al4V Or CoCrMo	Oral Implants Skrews and nuts	
Selective Leaching	Mercury from gold	Oral implants	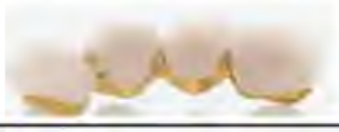

Figure 2.8: Types of corrosion in common implants [3], [8], [31], [38], [95].

2.3.4.6 Mechanisms of Corrosion In Vivo

Some forms of corrosion are most typical of implants and other medical devices (see Figure 2.8). These include localized (both pitting and crevice), intergranular and galvanic corrosion [13], [19], [43], [64], [68]. On the other hand, uniform (general) corrosion occurs in vivo very seldom.

Crevice Corrosion

As its name indicates, crevice corrosion occurs in narrow spaces where an electrolyte can creep, usually by capillary forces, between two metal parts or between a metal and an insulator. It is a form of localised corrosion typically related to a stagnant solution on the microenvironment level. As oxygen diffusion into the crevice is restricted, a differential aeration cell is established between the crevice (microenvironment) and the external surface (bulk environment). Oxygen depletion occurs in crevices, joints and under corrosion deposits, metallic or non-metallic deposits. Localised corrosion will take place at the area of low-oxygen concentration, which acts as an anode. Thus, crevice corrosion is often observed under riveted lap joints, bolt heads, gaskets, and O-rings. The susceptibility to crevice corrosion increases with increasing hysteresis of the polarisation curve, that is, the difference between $\mathbf{E}_b$ and $\mathbf{E}_p$. Therefore, a higher value of $\mathbf{E}_p$ reflects higher resistance to crevice corrosion. If the metal does not passivate until a potential below the resting potential is reached, it is susceptible to crevice corrosion. Two concerns with this type of corrosion are that: (1) the damage is concentrated within a small hidden area. Thus inspection is challenging, and (2) the extent of damage cannot be monitored by mass loss/gain measurements [55], [56], [58], [92].

The mechanism of crevice corrosion can be described as follows. An oxygen reduction reaction accompanies the metal oxidation reaction. Initially, these reactions occur uniformly all over the surface, including in crevices; the oxygen concentration in the solution inside a crevice is equal to the level of soluble oxygen and is the same everywhere. However, oxygen in the crevice is depleted due to mass transport limitations. Thus its reduction in this area ceases. Because the crevice area is usually minimal compared to the overall surface area, we will not observe any significant drop in the overall reduction rate; thus, the corrosion rate almost does not change. However, to compensate for the positive charge associated with metal cations continuously forming within the crevice, anions diffuse into the crevice; these are often chloride ions. The chloride anion is associated with the metal cation, and the metal chloride reacts with water to form metal hydroxide and hydrochloric acid. The pH in a crevice can reach very acidic values, occasionally as those of pure acids. The acidification of the microenvironment can lead to a significant increase in the corrosion rate of most metals. The dissociated chloride ion can react again with the metal ion, and the series of reactions repeat. This is an autocatalytic process. The solid corrosion products seal even further the crevice microenvironment. Because the anodic area is localised and small in comparison to the cathodic site, yet both should transfer the same current, the anode current density increases, together with the corrosion rate [16], [47], [58], [66].

Metals susceptible to pitting corrosion also suffer from crevice corrosion. The presence of crevices on the surface often triggers localised corrosion under conditions where stable pitting would not occur (e.g., at lower concentrations of halides). In the case of medical devices, failures in this

mechanism have been observed at the interface between bone plates and screws made of 316L stainless steel (Figure 2.9), as well as in cemented Ti-based hip implants [27] [103]. Because a porous matrix provides inherent crevices, it is not surprising that porous titanium sand porous CoCrMo alloys have been shown to exhibit much higher corrosion rates compared to their dense counterparts.

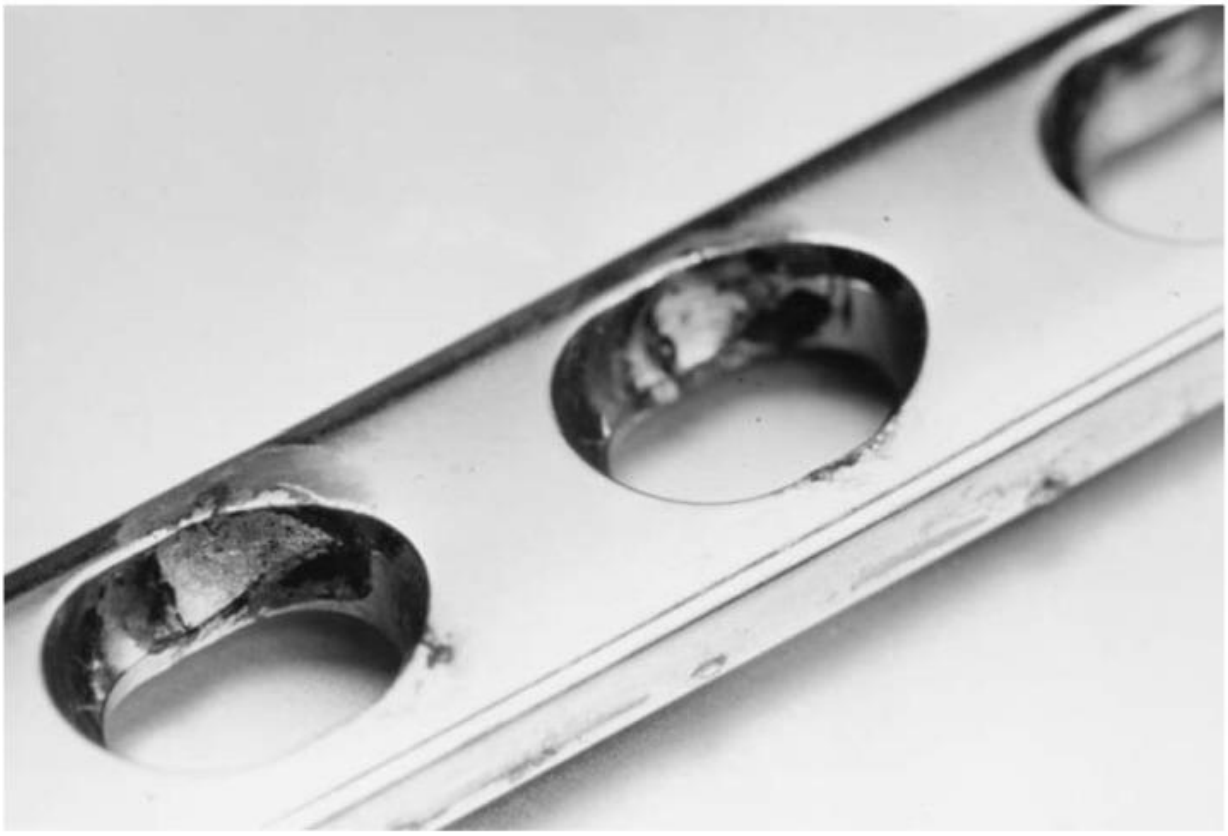

Figure 2.9: Crevice corrosion in a screw hole in fracture fixation plate.

Guindy et al.[7] studied six dental implants whose late failure was related to superstructure metal corrosion at the marginal gap. The superstructures (crowns) were porcelain fused to a gold alloy containing Pt, Pd, Ag, Co, In, and Sn. Extensive corrosion lesions and areas of oxidation were observed on all implants and inner crown surfaces. Bone tissue from around five implants showed higher contents of metal ions in comparison to physiologic baseline values. It was concluded that corrosion was initiated by the bonding oxides, which are necessary for fusing porcelain to gold, and rapidly propagated at the gap crevices. The pH in these regions is locally reduced due to decreased oxygen flow and bacteria colonisation at the marginal gap spaces. To avoid failure recurrence, the authors suggested designing a single-unit implant abutment as well as crowns made of a homogeneous, biocompatible Ti. In addition, all conditionally removable superstructures should be cemented or sealed to avoid bacterial colonisation and possible crevice corrosion.

Pitting Corrosion

Pitting corrosion is a highly localised corrosion of a metal surface confined to a small area and takes cavities. This is generally a process of local anodic dissolution, for example, at regional breakdowns of the passive layer, where metal loss is exacerbated by the presence of a small anode and a large cathode. Pitting is commonly observed on surfaces with little or no general corrosion. It is often initiated at MnS inclusion sites, surface scratches, dislocations or other defects, local breakdown of the passive layer due to chloride, fluoride, and other halide ions, or arbrandomcal variations in the composition of the electrolyte solution.

After their initiation, pits either keep growing, or passivation may occur. An alloy with a high pitting corrosion resistance should ideally combine low susceptibility to pit initiation, low pit propagation rate, and fast passivation. For metals with electron-conducting passive films such as stainless steels, the number of pits usually correlates inversely with their average depth since the cathodic current consumed by the large passive surface area fosters anodic dissolution inside the pits. The pits may grow at different rates, depending on the number of active pits [19], [22], [23], [61], [70].

An increase in the resistance to pitting corrosion is concomitant with an increase in $\mathbf{E}_b$. While pitting will occur on a pit-free surface above $\mathbf{E}_b$, only in the range of potentials between Ep and Eb will occur if the surface is already pitted. Increasing the temperature usually increases the susceptibility to pitting. All metals susceptible to pitting corrosion are also vulnerable to crevice corrosion but not vice versa. Stainless steels are susceptible. The pits usually grow in the direction of gravity. They can have different shapes, such as deep and narrow, shallow and wide, elliptical, undercutting, subsurface, horizontal or vertical grain attack. ASTM G46 describes the selection of procedures that can be used to identify and examine pits and evaluate pitting, including a standard rating chart [7].

The most common mechanism of pitting corrosion of stainless steel is as follows. In an alkaline chloride solution, anodic dissolution of stainless-steel produces Fe^{2+}, which attracts negative anions such as Cl^- to the initiation site. Hydrolysis occurs following the reaction.

$$\underline{Fe_2}{+}{+}2\underline{H_2O}+2\underline{Cl}^-\rightarrow\underline{Fe(OH)_2}+2\underline{HCl}. \quad (16)$$

Consequently, the pH drops in the initiation site. An autocatalytic mechanism of pit growth occurs. The acidic chloride solution rushes anodic dissolution, concentrating more Cl^- in the pit. The insoluble cap of the corrosion product, $Fe(OH)_3$, forms at the entrance to the pit; Fe^{2+} diffuses from inside to outside of the pit, where it is oxidised to Fe^{3+} and precipitates in the neutral bulk solution. The cap inhibits the escape of Fe^{2+} but is amply porous to allow Cl^- migration into the pit, thus preserving high acidic chloride concentration within the pit. Anodic polarisation of the inner pit occurs by coupling to the outer passive cathodic surfaces. The reduction of a solute oxidiser such as oxygen consumes the electrons that are generated by the anodic reaction in the pit [23], [25], [41], [68], [75].

Pitting corrosion was a common problem with the early 304 stainless steel implants. However, the addition of 2–3 wt% Mo in 316L stainless steel has dramatically reduced the number of failures

due to pitting corrosion [19], [61], [70], [104]. Mudali et al. Alloying annealed 316L stainless steel with 0.05–0.22 wt% nitrogen significantly increased the pitting corrosion resistance in a 0.5 M NaCl electrolyte.[56], [70] A synergistic effect of nitrogen alloying and cold working of up to 20% improved pitting resistance. However, the pitting resistance decreased at higher cold working levels, more pronounced at higher nitrogen contents. These synergistic effects were attributed to the role of nitrogen in increasing the density of fine deformation bands [41].

Cobalt-based alloys have been found resistant to pitting corrosion under static conditions[16], [26] but exposed to pitting corrosion under cyclic loads or following severe cold work [47], [71], [72], [105]. In addition, in vivo pitting of CoCrMo is a common characteristic of corrosion damage near or within modular tapers. It indicates the likelihood that the electrode potential of this alloy can be shifted very positively compared to its rest potential in physiological solutions, probably due to exposure to reactive oxygen species (ROS) associated with inflammation [19], [68], [76].

Titanium is susceptible to passivity breakdown in chloride-containing solutions only at very high anodic potentials not met in any in vivo environment. For example, for CP-Ti, pitting potentials higher than 10 V have been documented in chloride-containing solutions. Ti is an interesting exception in that the chloride ion is the least pit-triggering anion among the halides, in contrast to other materials with a passive layer [13], [23]. Although titanium alloys may be less resistant than CP-Ti due to discontinuities in the protective oxide film, in vivo pitting-related failures have not been reported to the best of my knowledge.

It is worth noting. However, metastable pitting corrosion has been reported for both CP-Ti and Ti–6Al–4V in NaCl and SBFs far below the pitting potential, even at the OCP. This means that local passivity breakdown events can occur in the passive region of titanium. Instead of pit propagation, the small pits do not remain active; instead, fast passivation occurs. Such events of metastable pitting can be witnessed experimentally as current transient bursts within the passive region in potentiodynamic or potentiostat polarisation curves if the experiments are conducted with sufficient current and time resolutions and no noise filtering is imposed. For Ti in chloride-containing solutions, these events can typically only be resolved using microelectrodes. Although metastable pitting does not result in a complete deterioration of the system, it nevertheless indicates that the passivity of the metal is not fully stable in the environment, and the small activation/passivation events contribute to passive dissolution modes. Furthermore, in contrast to the metastable pitting behaviour of stainless steels, where the number of pit initiation events typically drops to virtually zero over time, for titanium, the metastable pitting activity remains high throughout the experiment (namely, for some hours). This behaviour may be non-desirable with respect to metal ion release from Ti-based implants [19], [21], [65], [80].

The risk of pitting corrosion in the oral cavity is much higher due to the availability of oxygen and acidic foodstuffs. However, the development of ultraclean grades, such as 316LVM and/or nitrogen additions, have reduced this risk for stainless steel. On the other hand, in vitro experiments have shown that titanium alloys might suffer from pitting at high potentials in saline or the high fluoride solutions used in dental cleaning procedures [82]. CP-Ti exposed to various static

immersion tests has also shown a significant increase in ion release (by approximately four orders of magnitude) in the presence of fluoride.

ASTM F746 [7], [55], [58] describes a laboratory screening test for the determination of the resistance of passive metals and alloys from which surgical implants are manufactured to pitting or crevice corrosion or both. Figure 2.10 shows two examples of pitting corrosion in vivo. Figure 2.10a shows micro-pitting on an oxidised tubing (OT) Nitinol stent after six months implantation into the iliac artery of a minipig [7], [55], [58]. Figure 2.10b shows the surface of an Mg–Y–Ca–Zr WX11 alloy in the as-cast condition after potentiodynamic polarisation test in Dulbecco's Modified Eagle Medium (DMEM) with 10% FBS at 37 °C and cleaning with $CrO_3/AgNO_3$ solution to remove the corrosion products. Pitting corrosion, a commonly observed phenomenon in Mg alloys, is evident along with corrosion at grain boundary regions (arrow) prone to corrosion due to higher secondary phase localisation [106].

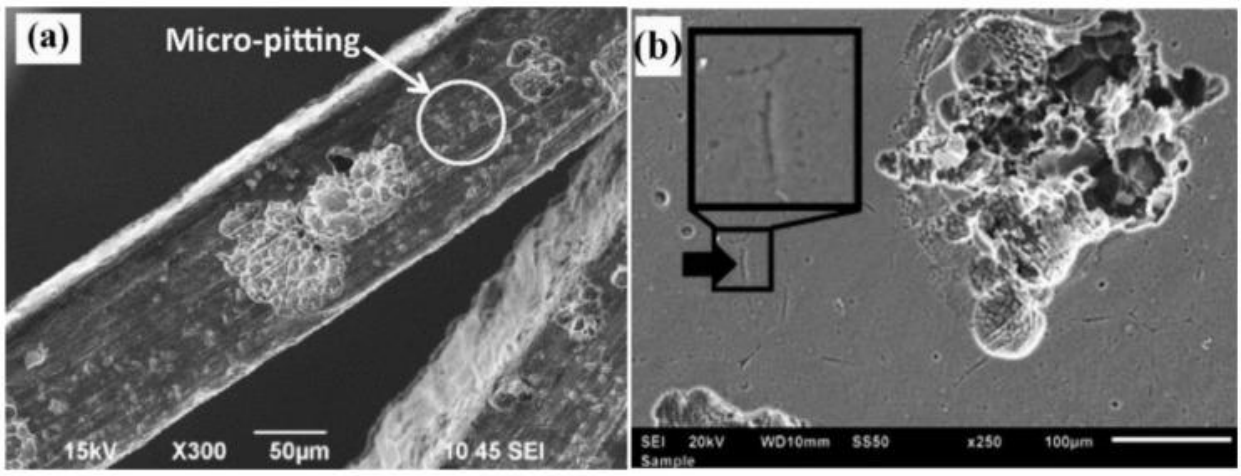

Figure 2.10: Pitting corrosion. (a) Aoxidiseded tubing Nitinol stent after six months of implantation into a minipig's iliac artery. (b) An Mg–Y–Ca–Zr WX11 alloy in the as-cast condition following potentiodynamic polarization test in DMEM with 10% FBS at 37 °C and cleaning with CrO3/AgNO3 solution. (b) also shows corrosion at prone grain boundary regions (arrow).

Intergranular Corrosion

Intergranular corrosion occurs at grain boundaries due to a second phase, contaminants, or atom segregation. A galvanic cell is then established, with the anode around/at grain boundaries. Two examples of intergranular corrosion in engineering materials are sensitisation and exfoliation. Since the carbon content in 316 stainless steel was lowered in the 316L and 316LVM grades, sensitisation of this steel is no longer a problem as it used to be. Intergranular corrosion has been observed primarily in CoCrMo alloy in modular taper junctions [61] and in some Ti–6Al–4V. Figure 2.11 shows intergranular pitting corrosion of a CoCrMo alloy [7], [31], [45], [66]. Electrochemical corrosion tests were conducted in a bovine calf serum (BCS) solution with protein, which was buffered at pH 7.4 and kept at 37 °C. The attack was localised at phase

boundaries and grain boundaries of high energy (namely, high-angle and low lattice coincidence, Σ11 or higher). In contrast, grain boundaries of lower energy did not seem to rust.

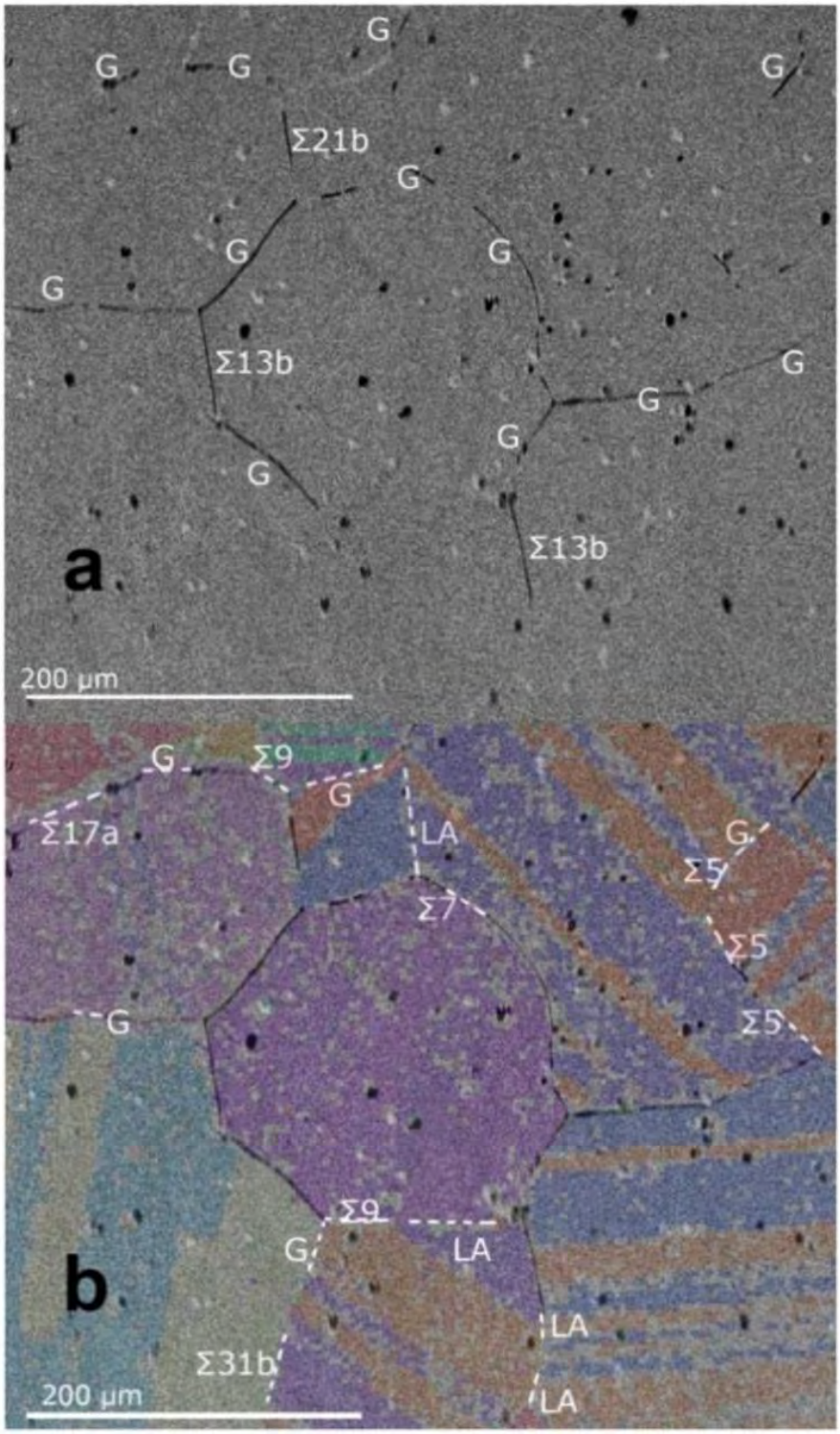

Figure 2.11: (a) Indexing of corroded grain boundaries based on orientational image mappings (OIM) established by electron backscatter diffraction (EBSD). (b) Indexing of uncorroded grain boundaries based on OIM (overlaid). "G" indicates general grain boundary geometry with no lattice site coincidence, "LA" indicates low angle [287]. Reprinted with permission from John Wiley and Sons, Inc.

Galvanic Corrosion

Galvanic corrosion, also known as bimetallic corrosion, is accelerated corrosion of a relatively active metal (anode) when it is brought in electrical contact with a more noble metal (cathode) in a common electrolyte. This form of corrosion may be either uniform or localised. It can be particularly severe under conditions where protective corrosion films do not form or where needs of erosion-corrosion remove them. ASTM G71, ASTM G82, and ASTM F3044 are three applicable standards.[7]

Metals such as Au and Pt are very noble. They have a low driving force for oxidation in aqueous solutions; hence, they maintain their metallic form in vivo. Other metals at the bottom of the EMF series, including titanium, have a high driving force for oxidation. Fortunately, the practical nobility, rather than thermodynamic nobility, matters in service. From a practical standpoint, the nobility is higher as the immunity and passivation regions in the Pourbaix diagrams extend below and above the water stability region. These regions overlap with the pH range of 4–10. As discussed before, titanium and its alloys serve very well in vivo. This is because they become passive (i.e., essentially inert) under most service conditions due to the spontaneous, rapid formation of a dense, fully covering, well-adhered oxide layer that serves as a **kinetic** barrier to the transport of metal ions and electrons. Other alloys that rely on forming a passive film to prevent oxidation are based on iron, zirconium, cobalt, tantalum, niobium, and so forth.

Dissimilarity of electrodes may also result from the non-uniform chemical composition of the electrode material, local changes in solution chemistry or dissolved oxygen concentration, different processing routes (e.g., wrought versus cast Co alloys), and surface defects.

The EMF series, though, has several limitations: (1) it reflects standard conditions, while in situations of practical interest, the system is rarely, if ever, under standard conditions; (2) it lists only pure metals, not alloys; (3) it does not reflect kinetic effects such as passivity [13], [55], [76], [104].

The **Galvanic series**, Figure 2.12, is more appropriate than the EMF series to describe actual corrosion problems as alloys and not pure metals are often coupled. The metals undergo corrosion rather than equilibrium with their ions at standard concentrations. Usually, the further apart two metals are in the series (i.e., the more significant the potential difference between them), the greater is the driving force for galvanic corrosion, and the greater the damage to the anode will often be [7], [50]. Often, the maximum allowable potential difference between the metals is 200 mV.

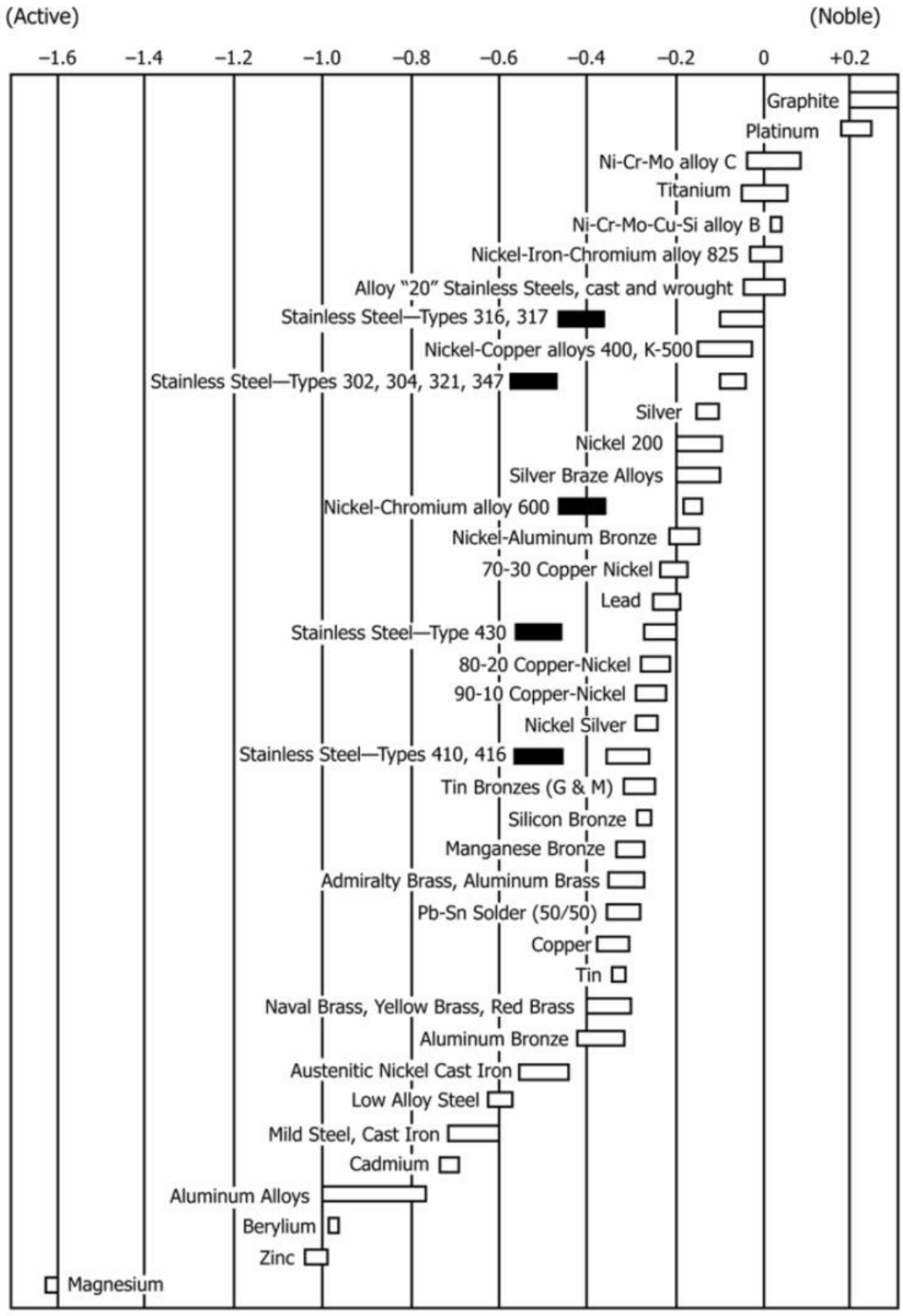
(Active)
(Noble)
−1.6
−1.4
−1.2
−1.0
−0.8
−0.6
−0.4
−0.2
0
+0.2
Graphite
Platinum
Ni-Cr-Mo alloy C
Titanium
Ni-Cr-Mo-Cu-Si alloy B
Nickel-Iron-Chromium alloy 825
Alloy "20" Stainless Steels, cast and wrought
Stainless Steel—Types 316, 317
Nickel-Copper alloys 400, K-500
Stainless Steel—Types 302, 304, 321, 347
Silver
Nickel 200
Silver Braze Alloys
Nickel-Chromium alloy 600
Nickel-Aluminum Bronze
70-30 Copper Nickel
Lead
Stainless Steel—Type 430
80-20 Copper-Nickel
90-10 Copper-Nickel
Nickel Silver
Stainless Steel—Types 410, 416
Tin Bronzes (G & M)
Silicon Bronze
Manganese Bronze
Admiralty Brass, Aluminum Brass
Pb-Sn Solder (50/50)
Copper
Tin
Naval Brass, Yellow Brass, Red Brass
Aluminum Bronze
Austenitic Nickel Cast Iron
Low Alloy Steel
Mild Steel, Cast Iron
Cadmium
Aluminum Alloys
Berylium
Zinc
Magnesium

Figure 2.12: A galvanic series of various metals and alloys in flowing seawater at 2.4 to 4.0 m s–1 for 5 to 15 days at 5 to 30 °C. Dark boxes indicate the dynamic behaviour of active-passive alloys. Values of principal axis: volts versus SCE.

The anode-to-cathode surface areas ratio is also important: the lower this ratio is, the higher the current density on the anode is, and the higher the corrosion rate is. The maximal damage will occur near the plane of contact between the two metals because the driving force farther along is diminished by the potential drop across the solution resistance. Low conductivity of the electrolyte solution and low polarisation usually focus the galvanic attack closer to the contact zone. The nature of the environment is also important [23], [69], [107].

In principle, strategies for preventing galvanic corrosion include selecting materials with as similar electrode potentials as possible, using insulators between dissimilar metals, and using coatings or unique designs to limit the cathode area relative to the anode area.

Contact between dissimilar metals immersed in an electrolyte is common in orthopaedic, dental, and other biomedical applications. Examples include hip prostheses with the ball made of 316L stainless steel, a socket made of Ti–6Al–4V, and a CoCrMo femoral head in contact with a Ti–6Al–4V femoral stem, and a gold crown coupled to an amalgam core in the oral cavity.

When titanium- and cobalt-based alloys are coupled together in vivo, it may be anticipated that the passive titanium alloy would become the cathode. In contrast, the less tolerant cobalt alloy would undergo accelerated corrosion. However, in practice, the kinetics of the oxygen and water reduction reactions are slow on titanium surfaces. Because the passive current of titanium is virtually independent of potential, so it is easily polarised, titanium is a poor cathode. This means that the extent of accelerated corrosion caused to any metal from coupling to titanium should be small. Thus, titanium-cobalt combinations have been found stable both in vitro and in vivo, at least as long as no relative motion (fretting) occurs [14], [47], [54], [55], [58]. On the other hand, 316L stainless steel is susceptible to pitting corrosion when coupled to either Ti- or Co-based alloys. Mellado-Valero et al.[7] analysed the galvanic corrosion of CoCr, CoCr-c, NiCrTi, Au-Pd and Ti–6Al–4V dental alloys for implant superstructures when coupled to Ti grade 2 implants in artificial saliva (AS), with and without fluorides in different acidic conditions. It was concluded that NiCrTi is not recommended for implant superstructures due to the risk of Ni ion release to the body and that fluorides should be avoided in acidic media because Ti, Ti–6Al–4V and CoCr-c superstructures show galvanic corrosion. Ti/Ti–6Al–4V and Ti/CoCr were the best combinations as an alternative to noble gold alloys. Arslan et al.[7], [31] compared the galvanic couples Ti–6Al–4V/Au, Ti–6Al–4V/CoCr, and Ti–6Al–4V/CrNi in Ringer's solution by the use of Tafel plots, Evans diagrams, and EIS Nyquist plots. It was concluded that the Ti–6Al–4V/Au couple was most suitable for dental applications, whereas the corrosion behaviours of Ti–6Al–4V/CoCr and Ti–6Al–4V/CrNi couples were similar. Zitter and Pauluzzi [66] reported galvanic corrosion of an implant consisting of almost equal parts of iron and brass, where brass was cathodically protected until the iron part was completely dissolved. British/ISO standard 21534 [7] defines acceptable and non-acceptable combinations of materials for either articulating or non-articulating contacting surfaces of implants.

2.3.4 Radiopacity of Biomaterials:

2.3.4.1 Radiopaque: Opaque to one or another form of radiation, such as X-rays. Radiopaque objects block radiation rather than allow it to pass through. Metal, for instance, is radiopaque, so metal objects that a patient may have swallowed are visible on X-rays. Radiopaque dyes are used in radiology to enhance X-ray pictures of internal anatomic structures. The opposite of radiopaque is radiolucent. [6]

Radiopacity generally refers to the ability of a material to absorb X-rays, which contrasts it against other materials surrounding it in an X-ray image [15], [67], [71]. High X-ray visibility of surgical devices is critical during minimally invasive surgery for the exact placement of the minimally invasive surgical instruments within the targeted anatomical site while keeping the X-ray exposure of the patient to a minimum [37], [60], [67], yet radiopacity of common biomedical materials are generally low. Radiopaque markers, bands, or fillers made of heavier and expensive elements such as Pt, tantalum (Ta) and gold (Au) have been used to improve the X-ray visibility of surgical devices [67] [71], [72].

2.3.4.2 XMuDat software for measuring mass attenuation coefficient vs photon energy:

The photon mass attenuation coefficient, adequate atomic number, and electron density are the fundamental quantities required in determining the penetration of X and γ-ray in the matter. The mass attenuation coefficient measures the probability of the interaction between incident photons and the importance of the unit mass per unit area. The knowledge of the mass attenuation coefficients of X and γ-ray in biological and other vital materials is of significant interest for industrial, natural, agricultural, and medical applications. Additionally, the mass attenuation coefficient provides a wide variety of information about the fundamental properties of the matter at the atomic and molecular levels. Accurate values of the photon mass attenuation coefficients are required to provide essential data in diverse fields such as nuclear diagnostics (computerised tomography), radiation protection, nuclear medicine, radiation dosimetry, gamma-ray fluorescence studies, and radiation biophysics. The mass attenuation coefficients are also widely used to calculate the photon penetration and the energy deposition in biological shielding and other dosimetric materials. An organism requires biomedically essential elements to maintain its normal physiological function. Without biomedically crucial elements, the organism cannot complete its expected life cycle or achieve average healthy growth; such elements are the critical components of the metalloenzymes and are involved in crucial biological functions, such as oxygen transport, free radical scavenging, and hormonal activity. Biomedically, essential elements deficiency or excess concerning the human physiological level are found in patients with certain diseases, including cancer [108].

In the applications of X-ray photons for medical diagnostic and therapeutic purposes, the number of X-ray photons that are absorbed and transmitted after interaction within the human tissue and materials of biological interest can be theoretically evaluated by using linear (or mass) attenuation coefficients. The parameterisation of these interaction data has been reported to promote the ease

of use in theoretical simulations of transport and dosimetry of photons in medical and biological applications [109]. Specifically, for optimal assessments of the use of X-rays for medical purposes, accurate and appropriate X-ray photon interaction coefficients of various normal and diseased body tissues are required. In theoretical simulation exercises, researchers often need radiation-interaction data for tissues or 'tissue substitutes' of elemental composition and weight percentages, which differ from those reported in the literature [67], [109]. Significant disparities exist in the percentage values by weight of elements reported in the literature for body tissues and substitutes for individuals of different ages, genders, and health states. Often, interested parties need these radiation interaction data for body tissues or substitutes with the percentage by weight of elements and intermediate energies that are not tabulated in literature. To provide more precise values of these radiation interaction data and parameters, XMuDat is used with Windows 95 or Windows NT [109] to present and calculate various photon interaction coefficients. Six absorbing materials can be set up individually. Each material can be composed of components chosen from the elements and several compounds and mixtures of dosimetric interest. Data for mass attenuation-, mass-energy transfer- and mass-energy absorption coefficients in a photon energy range of 1 keV to 50 MeV can be retrieved [72], [86], [101], [110].

2.3.5 Biocompatibility of material

This is the property of implant material to show a favourable response in the given biological environment in a particular function. It depends on the corrosion resistance and cytotoxicity of corrosion products [2], [6], [31], [68], [69], [111], [112].

2.3.5.1 Definition:

• 'The quality of not having toxic or harmful effects on biological systems [69].

• 'The extent to which a foreign, usually implanted, material elicits an immune or other response in a recipient' [79].

• 'The ability to coexist with living organisms without harming them'[113].

• 'A material may be said to be biocompatible when it has the quality of being non-destructive in the biological environment. It is important to appreciate that this interaction works both ways. The material may be affected somehow by the biological environment, and, equally, the biological environment may be affected by the material' [114].

• 'Biocompatibility refers to the ability of a material to perform with an appropriate host response in a specific situation' [69].

• 'The ability of a material to elicit an appropriate response in a given application [69].

Historically, evaluating the biocompatibility of medical devices and biomaterials has been a complex task. This complexity arises because the machines are made from an extensive, diverse range of materials and have numerous intended uses, with body contact ranging from quick skin

contact to contact with blood and to permanent implantation. Biocompatibility is usually demonstrated by testing the device, materials, and leachable chemicals, using toxicological principles [69]. When reviewing over 50 years of experience with medical devices, it has been shown that in most cases, the sole requirement for biocompatibility in a medical device, intended for extended-term contact with tissues in the human body, is that the device and the materials from which it is constructed shall do no harm to the tissues it contacts and that it shall achieve this through chemical and biological inertness. It was found that rarely had an attempt to introduce physical activity into a biomaterial been clinically successful in these cases. It was shown that there is a need for specific and direct interaction between biomaterials and tissue components [17]. Williams et al. concluded that we should perhaps redefine biocompatibility as: 'The ability of a biomaterial to perform its desired function concerning a medical therapy without eliciting any undesirable local or systemic effects in the recipient or beneficiary of that therapy, but generating the most appropriate beneficial cellular or tissue response in that specific situation and optimising the clinically relevant performance of that therapy'.

The International Organization for Standardization (ISO) 10993 (1997–2009) plays an essential role in assessing the biocompatibility of a medical device. Theoretically, many tests need to be carried out depending on the medical device's intended use. The standard describes tests for toxicity, carcinogenicity, hemocompatibility, etc. Some of the tests are simple in vitro tests, but others require animal experiments.

In general, three categories of contact with a human being are distinguished [69]:

• Surface devices, where contact is made with the skin, intact mucosal membranes, and breached or compromised surfaces, for example, electrocardiography (ECG) electrodes.

• External communicating devices, where indirect contact is made with blood, tissue, or bone, for example, dental filling materials.

• Implant devices, where direct contact is made with blood, tissue, or bone, for example, breast implants.

A biocompatible material disrupts the normal body function as little as possible. Many factors influence implant biocompatibility, such as implant size, shape, material composition, surface wettability, surface roughness, and charge. The biomaterial must not: (1) change plasma proteins (including enzymes) to activate adverse reactions; (2) cause thrombus formation, adverse immune response, or cancer; (3) destroy or sensitise the cellular elements of the blood; (4) produce toxic or allergic responses; (5) deplete electrolytes; (6) be affected by sterilisation. In turn, the environment should not cause degradation (e.g., biological or mechanical) or corrosion of the biomaterial, resulting in loss of physical and mechanical properties. In practice, no synthetic material is entirely harmonious with the living environment; however, materials have different inertness levels.

Following implantation of biomaterials and medical devices, the following sequence of local events occur injury, blood-material interactions, provisional matrix formation, acute inflammation, chronic inflammation, granulation tissue development, foreign-body reaction (FBR), and fibrosis

(fibrous capsule development). The initial inflammatory response is activated by injury to vascularised connective tissue. Blood clot formation and thrombosis also occur since blood, and its components are involved in the initial inflammatory responses, blood clot formation and/or thrombosis also occur. Acute inflammation is of relatively short duration, lasting from minutes to days, depending on the extent of the injury. Its main characteristics are the exudation of fluid and plasma proteins and the emigration of leukocytes. Chronic inflammation is less uniform histologically than acute inflammation. It is generally characterised by mononuclear cells (i.e., monocytes and lymphocytes) at the implant site, with blood vessels and connective tissue proliferation. Chronic inflammation is typically short duration and is confined to the implant site. The persistence of the acute and/or inflammatory responses beyond three weeks usually indicates an infection. After the acute and chronic inflammatory responses are resolved, granulation tissue can be identified by the presence of macrophages, the infiltration of fibroblasts, and neovascularisation in the new healing tissue. Granulation tissue may be seen as early as 3–5 days post-implantation depending on the degree of injury. The essence of FBR (a particular form of nonimmune inflammation) is that the presence of an implant changes the healing process. FBR involves protein adsorption, macrophages, multinucleated foreign body giant cells (i.e., fused macrophages), fibroblasts and angiogenesis. FBR can result in fibrosis, scar or even biomaterial rejection. The FBR with the development of granulation tissue is considered the normal wound healing response to implanted biomaterials. For most inert biomaterials, the late tissue reaction is encapsulation by a relatively thin fibrous tissue composed of collagen and fibroblasts. The cellular components of the FBR separate this fibrous capsule from the granulation tissue.[7]

A significant factor influencing the host reaction to a biomaterial is the latter's surface because it is the one that the body "senses" first. The specific reactions at the surface determine the FBR, the healing process's path and speed, and the long-term development of the biomaterial/body interface. The chemical composition, structure and morphology of a surface are all critical in this regard. Hence, the nature of the initial interface between an artificial material and the adjacent tissue determines the ultimate success or failure of the implant.

Osteolysis (i.e., active resorption of bone matrix) and forming a thick fibrous layer between the implant and bone indicate poor biocompatibility. Furthermore, normally non-toxic materials (e.g., polyethene) might trigger an inflammatory response when they are in the form of microparticles of a certain size. These particles irritate phagocytic cells and activate them to produce and release cytokines, proteinases, growth factors, and other pro-inflammatory factors, eventually leading to chronic inflammation, fibrosis, osteolysis, and porosis in bone. In the case of aseptic loosening of the prosthesis, the presence of wear particles could lead to the formation of a poorly vascularised, synovial-like interface membrane between the prosthesis and bone. The formation of necrotic focuses, granulomas, and osteolysis may finally result in the prosthesis loosening. The increase of metallic wear also increases the total surface area of the metallic biomaterial, and consequently, the concentration of metal ions. The porous surface increases the surface area but also particular wear.[2], [7], [22], [26], [27], [29], [30], [56], [68], [103]

2.3.5.2 Biocompatible use of several metals for clinical purposes:

The following metals have been and are currently being used in the body and are either permanently or temporarily implanted: platinum, iridium, gold, silver, zinc, palladium and ruthenium, magnesium, cerium, erbium [69]

Platinum

Platinum-based drugs, cisplatin, and carboplatin have been used since the 1970s to treat testicular, ovarian, lung, and head and neck cancer. Platinum works by affecting the RNA and DNA of the cancer cells, ultimately destroying them [9]. Platinum is also used to make essential components for a range of medical devices, including pacemakers, implantable defibrillators, catheter stents, neuromodulation devices, replacement heart valves, and the treatment of an aneurysm. The properties that make platinum suitable for medical applications include biocompatibility and inertness within the body, durability, electrical conductivity, and radiopacity [69]. It is also used extensively in dentistry with other precious and non-precious metals to form alloys, which can be veneered with ceramic to replace damaged or missing teeth. Platinum is used to increase strength and melting temperature of the [29], [41], [68], [113] . The alloying addition of platinum to gold significantly reduces the rich yellow colour of gold [59], [102].

Iridium

Irradiated iridium wire, sheathed in platinum, is implanted into the body to deliver doses of radiation for cancer therapy. The platinum's radiopacity shields the healthy tissues from the radiation, but the exposed iridium tip irradiates the tumour [3], [6], [69]. Platinum- iridium electrodes are used in pacemakers and neuromodulation devices. Iridium is commonly added to platinum to reduce costs.

Gold

Gold is used for a wide variety of applications in the body. Gold was used in the nineteenth century for the treatment of depression, epilepsy, migraine, amenorrhea, and impotence [6], [67], [69], [107]. Gold is used to coat stents because its radiopaque nature makes it easier for surgeons to locate stents in the body. Gold coatings are also claimed to increase stent biocompatibility and hemocompatibility. Gold alloys can be used for radiopaque marker beads, electrode tips, electrode rings, tip coils, pacemakers, and defibrillators [67]. Rheumatologists use injections of weak solutions of sodium aurothiomalate or aurothioglucose to treat rheumatoid arthritis [34], [69]. Gold is also used to treat osteoarthritis of the knee to slow down damage to cartilage and bone, reducing joint pain. Tiny seeds of gold are used to treat prostate cancer, their opacity to X- rays helping clinicians target their radiotherapy treatment. Radioactive gold is used in diagnosis as a beta emitter as it passes through the body. Particles of a radioactive gold isotope have been implanted into the tissue to serve as a radiation source in treating certain cancers [34], [69]. In treating a condition called Lagophthalmos, an inability to close the eyelids, gold has been implanted in the upper eyelid to add weight and aid closure of the lid. Gold is used extensively for dental purposes, being alloyed with other precious and non-precious alloys to produce crowns and bridges to repair broken-down teeth and replace missing teeth. Novel developments in gold use involve gold

nanoparticles (GNPs), which are being studied because of their unique optoelectronic and electrochemical properties [117]–[120]. They have shown potential for biological applications, including sensors [69], catalysts [6], [69], optical probes [69], and tumour photothermal therapy [69].

Silver

Before the 1940s, silver was used to kill dangerous bacteria but lost favour with the discovery of antibiotics. However, scientists are currently rediscovering the benefits of colloidal silver in sticking plasters, burn dressings, water filter systems, the treatment of stomach ulcers, and treating eye infections in newborn babies [69]. It is used extensively in dentistry, being alloyed with other precious and nonprecious metals to produce crowns and bridges for the repair of broken-down teeth and the replacement of missing teeth, where it acts to strengthen and counteracts the reddish tint of copper [3], [32], [59], [81]. It is the main constituent in dental amalgam, alloying with tin, copper, and mercury. Silver- platinum coatings on orthodontic brackets have recently provided good antimicrobial activity [69]. Silver nanoparticles have also shown potential to prevent and treat asthma [69].

Zinc

While the full extent of some critical properties (e.g., mechanical properties, corrodibility, and biocompatibility) of biodegradable Zn is only recently being discovered, Zn's benefits to human physiology are relatively well known. Egyptians (2000 BCE) and medieval Romans already used Zn in medicinal creams [61]. Zinc is an essential trace element and plays catalytic, structural, and regulatory roles in the human cell. Zn has many physiological functions, including (i) having a direct signalling function at different cellular levels; (ii) is necessary for the function of more than 300 enzymes involved in diverse physiological processes such as wound healing, brain development, and cell membrane stability; (iii) is vital to the structure of several proteins, plays a regulatory role by inhibiting and activating enzymes and proteins; (iv) is an essential component in chromatin structure; (ii) plays a role in DNA replication and repair; (v) acts as an antioxidant via the stabilisation of DNA and cell membranes; (vi) is antiatherogenic, and (vii) improves endothelium integrity and prevents atherosclerosis.

A wide range of compositions has already been studied, namely, (i) pure Zn, (i) binary, (iii) ternary, and (iv) quaternary combinations of Zn with other elements. The following section describes the development of these Zn and Zn alloys for biomedical applications.[119]

Pure Zn: The first study on biodegradable Zn (99.95%) and other Zn alloys essentially started the formal research on using this metal for bioabsorbable implant applications. They observed from in vitro biodegradability tests that Zn indeed corrodes in a physiological fluid. Also, though they did not perform any biocompatibility tests, they noted that the dose of Zn ions released via corrosion is negligible compared to the maximum tolerable biological limit. They then concluded that Zn will not likely elicit a toxic response if used as an implant and is, therefore, a possible alternative to Mg-based biodegradable alloys.[119]

Binary alloys: The primary purpose of adding alloying elements to Zn is to alter two properties: (i) mechanical properties and (ii) biocorrosion properties. The most logical approach to Zn alloying for biomedical application is to combine it with elements known to be biocompatible or essential to human function, such as Mg, Ca, and Cu. Magnesium is the most well-known and the most studied biodegradable metal. Therefore, it is not surprising that a substantial number of studies looked at the combination of Mg and Zn. [119]

Ternary alloys: Studies on other ternary combinations were similarly pursued, with most of these based on the Zn-Mg combination. Some of the reported Zn-Mg-based ternary alloys include zinc-magnesium iron (Zn-Mg-Fe), zinc-magnesium-strontium (Zn-Mg-Sr), zinc-magnesium-calcium (Zn-Mg-Ca), and zinc magnesium-manganese (Zn-Mg-Mn). Again, using Zn-Mg as a base for the ternary alloy makes sense since this binary combination is the most studied owing to its expected good biocompatibility.[119]

Commercial alloys: Some commercially available Zn alloys have also been studied as a possible biodegradable implant material. Commercial alloys offer the distinct advantage of good accessibility and predictable composition. Wang et al. investigated the biodegradability and biocompatibility of ZA4-1 (3.5–4.5 Al, 0.75–1.25 Cu, 0.03– 0.08Mg), ZA4-3 (3.5–4.3Al, 2.5–3.2 Cu, 0.03–0.06Mg) and ZA6-1 (5.6–6.0 Al, 1.2–1.6 Cu) Zn alloys, while Kannan et al. studied similar properties in Zn-5Al-4 Mg.[119]

Palladium

Palladium has similar properties to platinum and has good mechanical strength, biocompatibility, radiopacity, and corrosion resistance. Palladium-103, a radioactive isotope of palladium, is showing promising results in the treatment of prostate cancer and is being investigated as a potential treatment for breast cancer. Palladium is also used extensively in dentistry with other precious and non-precious metals to form alloys capable of being veneered with ceramic to replace damaged or missing teeth. Adding small amounts of palladium to silver-containing 42 Precious Metals for Biomedical Applications alloys prevents the rapid corrosion of such alloys in the oral environment [40], [120].

Ruthenium

Ruthenium is being used to develop anticancer drugs. Two ruthenium anticancer drugs have recently entered clinical trials. Like iridium, ruthenium is also used in small amounts in dental alloys as a grain refiner to keep the grain size small [121].

Magnesium

Magnesium has a long history of successful use as an implant material, though early applications considered biodegradability a disadvantage. Magnesium offers excellent biocompatibility, as indicated by its high RDI. It has good mechanical properties, particularly having an elastic modulus approximating human bone. The boom in Mg research came about with the renewed interest in the idea of degradable metals. Magnesium and its alloys (e.g., Mg-Ca, Mg-Zn, Mg-Si, Mg-Sn, Mg-Zr, Mg-Al, Mg-Y, and Mg-REE) are the most widely studied and considered most

promising among the bioabsorbable metals. In fact, in 2016, BIOTRONIK released the first commercially available, clinically proven, sirolimus-eluting bioabsorbable magnesium stent. [119]

Erbium

The effects of Er modification were investigated on the microstructure, mechanical, and corrosion characteristics of extruded Mg-Al alloys[122]. From the structure-property relationship, Er addition can improve Mg-Al alloys' purity levels and marginally reduce the average grain size by well-defined Mg17Al12 and Al3Er grain boundary intermetallic. The Young's modulus and dimensional stability of Er modified alloys also improved marginally and were attributed to the formation of delicate Al3Er phases. Other mechanical properties under indentation, tension and compression loads of Mg-Al alloys were improved after Er modification [122].

Cerium

Rare earth elements are promising alloying element candidates for magnesium alloys used as biodegradable devices in biomedical applications. Rare earth elements significantly affect the high-temperature strength and the creep resistance of alloys and improve magnesium corrosion resistance. The higher Ce addition can have a better protective effect with cerium in the surface film. Interestingly, Mg–Ce alloy seems to be more susceptible to corrosion in vivo [123].

2.3.6 Mechanical property- Hardness

To perform successfully in vivo, an implant material must possess particular and well-controlled properties suited to each application. Insignificant load-bearing situations, such as joint replacement, may be emphasised on the strength of the material and its ability to withstand repeated loading and unloading cycles. The focus in repairing minor bone defects, on the other hand, may lie on the chemical composition of the material and whether it can bond with surrounding bone tissue or trigger new growth. While the emphasis may be placed on one area, say strength, the situation is not so simple as choosing the most robust available material and implanting it. We must first understand what microstructural properties influence that strength and control them. We must consider how susceptible that material's chemistry is to alterations in the body's environment. What, at first glance, may seem like the ideal material could fail catastrophically when placed in the body. The better choice may be a weaker material that is inherently less susceptible to degradation in vivo but whose microstructure can be altered to make it stronger and thus the more successful implant material for that application. The essential things to understand are (1) how to manipulate a material's characteristics through changes in chemistry, microstructure, and processing; (2) the relevant techniques to characterise the material's properties thoroughly and (3) the interrelationship between different levels and types of material properties. Figure 2.13 illustrates this concept, showing how mechanical microstructural and physiological effects interact and come together to determine the in vivo success of the material. Indeed, examples of relationships between any two of these property types can be given. It is necessary to consider these associations and how all three interrelate and control the performance of implant

material. When selecting a material for an implant, one of the primary considerations is its required mechanical performance in the skeletal application [79], [124].

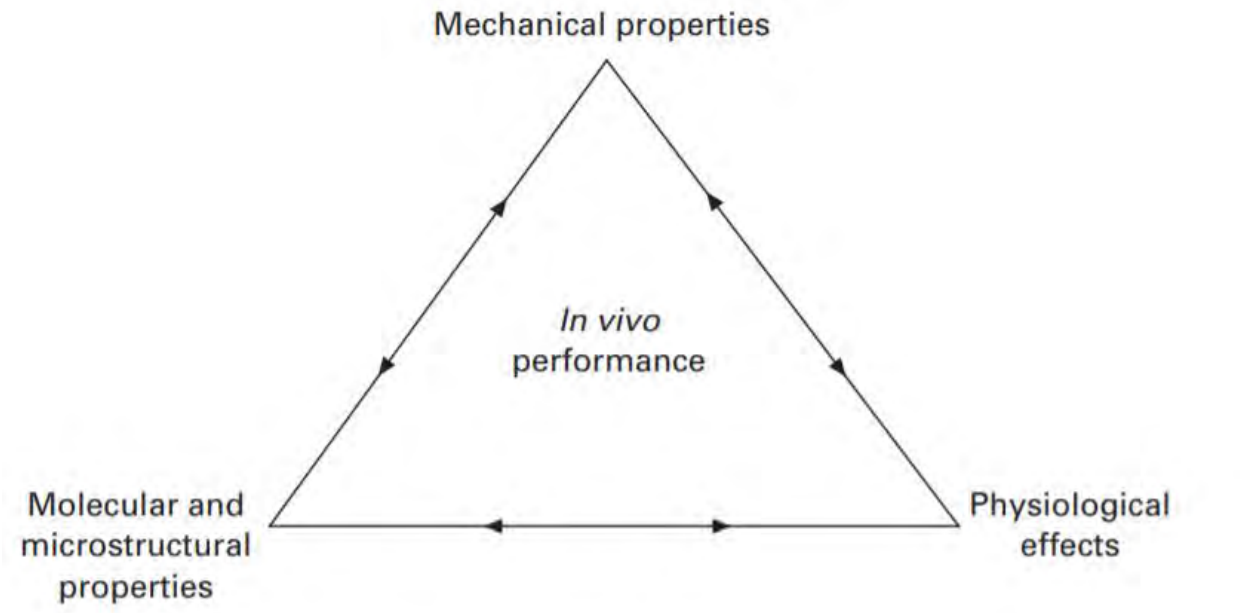

Figure 2.13: Interdependent relationship between different biomaterial properties and in vivo performance.

Hardness is a measure of plastic deformation and is defined as the force per unit area of indentation or penetration; Hardness is one of the essential parameters for comparing properties of materials. It is used for finding the suitability of the clinical use of biomaterials and has a positive effect on mechanical degradation resistance. Higher hardness resulted in minor abrasion. Biomaterial hardness is desirable as equal to bone hardness. Because if it is more than the biomaterial, it penetrates the bone. As above said, biomaterials samples are tiny; therefore, micro and nanoscale hardness tests (Diamond Knoop and Vickers indenters) are used. It is rather challenging to use a traditional hardness test for ceramics and glasses due to their nonyielding nature (no plastic deformation) [59][79].

Hardness tests measure resistance to indentation and are notable for being fast, easy, and non-destructive. A force is applied to an indenter, such as a steel ball or diamond pyramid. The resulting size or depth of the indentation in the material's surface is measured using a microscope. There are several different types of hardness tests, varying in the shape and material of the indenter and the scale of the load applied. Some of the more common tests are Brinell and Rockwell to measure microhardness, Knoop to measure microhardness, and Vickers to measure macro- and microhardness. Nanoindentation can also be performed with a Berkovich test. Specific hardness formulae match each type of hardness test. Lower numbers indicate the material is easily scratched or dented, whereas higher numbers mean more resistance to indentation. Hardness is often related to other properties, such as tensile strength. For steels, cast irons, and brass, hardness, and tensile strength have a linear relationship [37], [105], [122], [125].

2.4 Spark Plasma Sintering

Sintering makes objects from powder by heating the material in a furnace below its melting point so that bonding occurs by diffusion of atoms. This leads to individual powder particles adhering to each other in a dense compact. The process is usually used for ceramics. Sintering can be done using conventional Spark Plasma Sintering (SPS), Microwave Sintering, etc. Spark Plasma Sintering is one of the processing routes to process biomaterials in the laboratory [126].

Spark plasma sintering (SPS) or pulsed electric current sintering (PECS) is a sintering technique utilising uniaxial force and a pulsed (on-off) direct electrical current (DC) under low atmospheric pressure to perform high-speed consolidation of the powder. This natural way of heating allows the application of very high heating and cooling rates, enhancing densification over grain growth-promoting diffusion mechanisms (Figure. 2.14), allowing maintaining the intrinsic properties of nanopowders in their fully dense products [127].

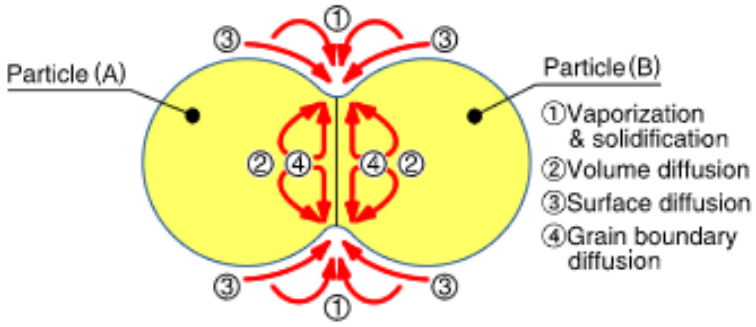

Figure 2.14: Material transfer path during sintering

It is regarded as a rapid sintering method in which the healing power is not only distributed over the volume of the powder compact homogeneously in a macroscopic scale but moreover, the heating power is dissipated precisely at the locations in the microscopic scale, where energy is required for the sintering process, namely at the contact points of the powder particles (see Figure 2.15). This resulted in a good sintering behaviour with less grain growth and suppressed powder decomposition. Depending on the powder type, additional advantageous effects at the contact points are assumed by a couple of authors [127].

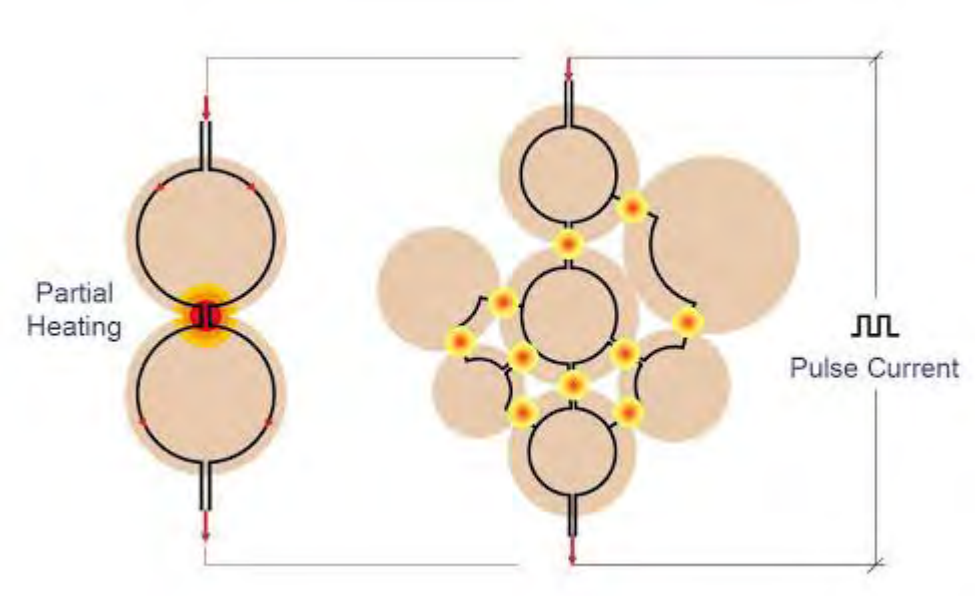

Figure 2.15: Energy dissipation in the microscopic scale

2.4.1 Advantage over Conventional Sintering

Spark Plasma Sintering is a new technique that takes only a few minutes to complete a sintering process compared to conventional sintering, which may take hours or even days for the same. This high sintering rate is possible in SPS since high heating rates can be easily attained due to internal heating of the sample instead of external heating seen in conventional sintering. Also, sintering time is reduced in SPS due to smallholding time at the sintering temperature, usually 5 to 10 minutes, while traditional sintering may extend to hours. The heating rates usually attained in conventional furnaces are 5 to 8°C/min, going maximum up to 10°C/min. So, to reach a temperature of 1200°C, we usually require 2 to 4 hours or more, whereas, in SPS, heating rates exceeding 300°C/min are easily obtained; hence a temperature of 1200°C can be obtained in only 4 minutes. Simultaneous application of temperature and pressure leads to high densification, and hence a dense compact at sintering temperatures lower by 200 to 250°C than in conventional sintering is easily obtained. Since no coarsening and grain growth could occur in SPS, high relative densities were reached quickly, and nano-sized powders can be sintered without considerable grain growth, which is impossible in the conventional sintering process. Hence, SPS can easily prepare nanostructured ceramics or nanocomposites with more densification and fewer defects. These nano-structured composites exhibit excellent mechanical properties like high strength, hardness, etc. A green compact usually needs to be prepared externally using a suitable die and hydraulic machine to apply the necessary pressure for conventional sintering. After this, the green compact is sintered in a furnace. In SPS, the powder is directly fed into the graphite dies, and the die is enclosed with the right punches. This assembly is directly put into the SPS chamber, and spacers are used if necessary. The chamber is now closed, and the atmosphere (vacuum, Argon, etc.) in

which sintering is to be carried out is applied in the section. The program is set into the control unit, and sintering is carried out. Atmosphere control is much easier in SPS than in conventional furnaces. All materials, even those difficult-to-densify, can be easily sintered in SPS. Due to the advantage of high heating rate and less holding time, SPS can restrict the unwanted sintering reactions in highly reactive systems instead of conventional sintering. Hence, the formation of undesirable product phases can be avoided [126].

SPS systems offer many advantages over conventional methods: hot press (HP) sintering, hot isostatic pressing (HIP), or atmospheric furnaces, including ease of operation and ac- curate control of sintering energy and high sintering speed, high reproducibility, safety, and reliability. While similar in some aspects to HP, the SPS process is characterised by applying the electric current through a power supply, leading to very rapid and efficient heating (Figure. 2.16). The heating rate during the SPS process depends on the geometry of the container/sample ensemble, its thermal and electrical properties, and the electric power supplier. Heating rates as high as 1000 °C/min can be achieved. Consequently, the processing time typically takes minutes depending on the material, dimensions of the piece, configuration, and equipment capacity.

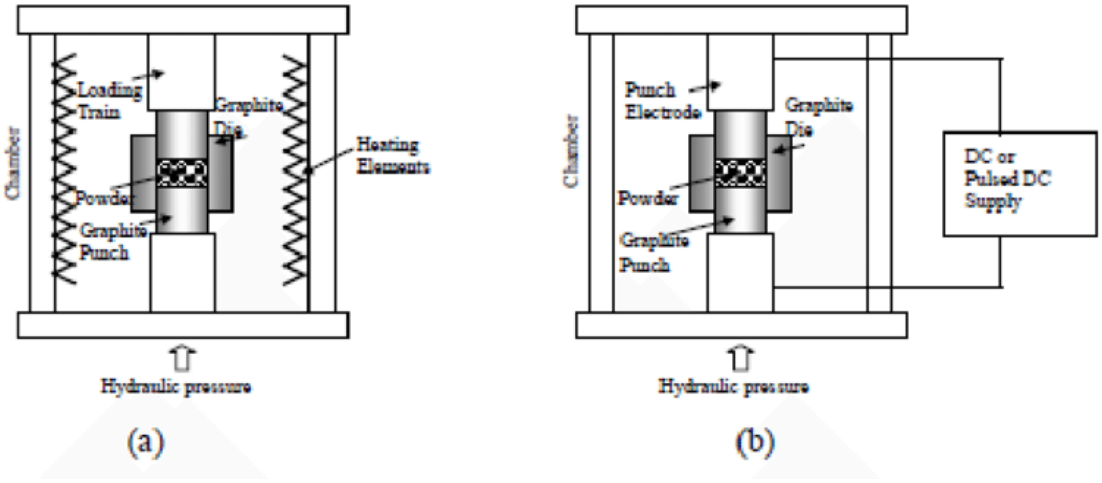

Figure 2.16: Schematic representation of (a) HP and (b) SPS

On the contrary, in conventional HP techniques, the powder container is typically heated by radiation from the enclosing furnace through external heating elements and convection of inert gases if applicable. Therefore, the sample is heated because of the heat transfer from the container's exterior surface to the powders. The resulting heating rate is typically slow, and the process can last hours. In addition, a lot of heat is wasted as the whole volume of space is heated, and the compact indirectly receives heat from the hot environment. On the other hand, SPS processes are characterised by the efficient use of the heat input, mainly when electrically insulating powders are used, and the pulsed electric current is applied. However, it should be mentioned that in the SPS process s, the problem of adequate electrical conductivity of the powders and the achievement of homogenous temperature distribution is particularly acute. In this way, the electric current delivered during SPS processes can generally assume different intensities and waveforms,

depending on the power supply characteristics. To permit a homogeneous sintering behaviour, the temperature gradients inside the specimen should be minimised. Important parameters that drastically determine the temperature distribution inside the sample are the sample material's electrical conductivity, the die wall thickness, and the presence of graphite papers used to prevent direct contact between graphite parts and the specimen and used to guarantee electrical contacts between all parts [127]. Figure 2.16 shows the materials covered by SPS processing [128].

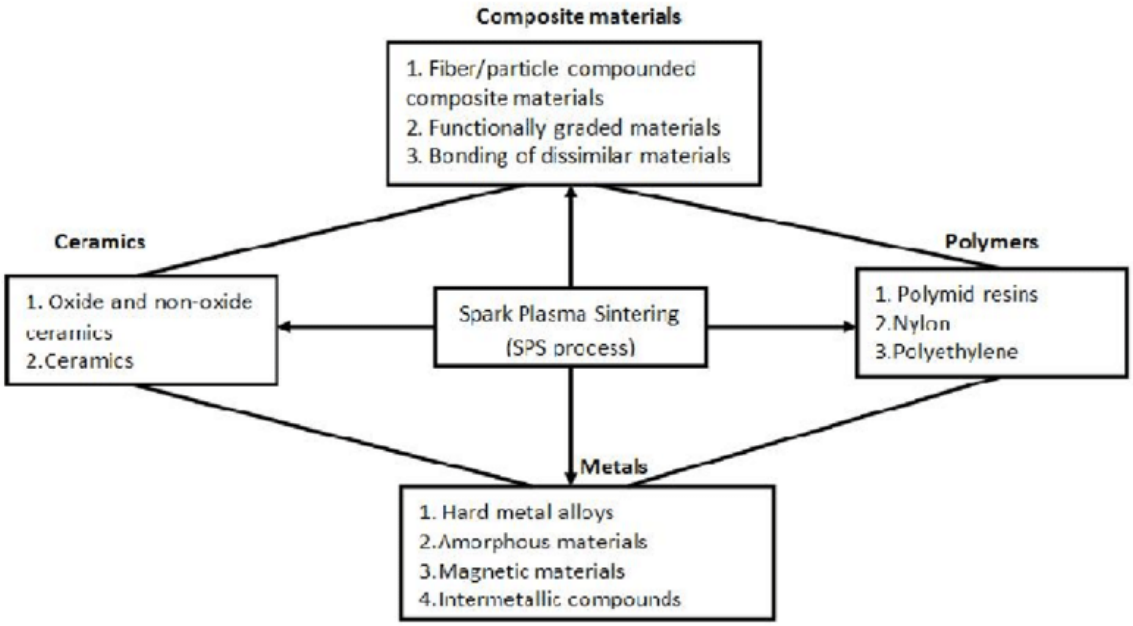

Figure 2.17: Typical examples of materials covered by SPS processing.

2.4.2 The basic SPS configuration and process:

Spark plasma sintering (SPS), also called pulse discharge sintering (PDS), is pressure and the current assisted sintering method, which lowers the sintering temperature and shortens the sintering time. SPS operational temperatures are typically 200-500^{o}C lower than conventional sintering methods. Lower temperatures and shorter holding times allow densifying nanometric powders and prevent the developing grain from coarsening fully. SPSed materials often exhibit improved physical and mechanical properties compared to conventional methods. Noteworthy features resulting from SPS include superplastic behaviour of ultrafine ceramics, the increased permittivity of ferroelectric materials, improved magnetic properties of magnetic materials, enhanced product-scale bonding, augmented thermoelectric properties, superior mechanical properties, and reduced impurities segregation at grain boundaries [129].

The basic configuration of a typical SPS system is shown in Figure 2.18. The system consists of an SPS sintering machine with vertical single-axis prespressurisation built-in water-cooled unique

energienergisingnism, a water-cooled vacuum chamber, atmosphere controls, a vacuum exhaust unit, and a selective sintering DC pulse generator, and an SPS controller. The powder materials are stacked between the die and punch on the sintering stage in the chamber and held between the electrodes. Under pressure and pulse energised, the temperature quickly 322 rises to 1000~2500 °C above the ambient temperature, resulting in the production of high-quality sintered compact in only a few minutes [127].

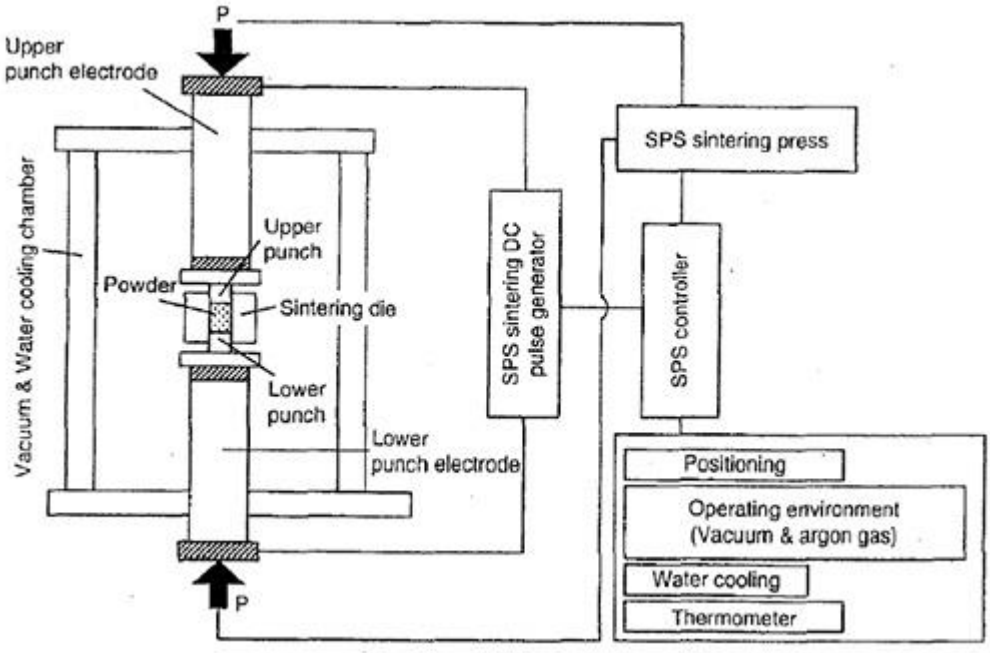

Figure 2.18: SPS system configuration and vacuum chamber

2.4.3 Principles and mechanism of the SPS process

The SPS process is based on the electrical spark discharge phenomenon: high energy, low voltage spark pulse current momentarily generates spark plasma at high localised temperatures, from several to ten thousand ℃ between the particles resulting in optimum thermal and electrolytic diffusion. SPS sintering temperatures range from low to over 2000 ℃, 200 to 500 ℃ lower than conventional sintering. Vaporisation, melting, and sintering are completed in short periods of approximately 5 to 20 minutes, including temperature rise and holding times. Several explanations have been proposed for the effect of SPS:

1. Plasma generation
2. Electroplastic effect
3. Joule heating
4. Pulsed current.
5. Mechanical pressure

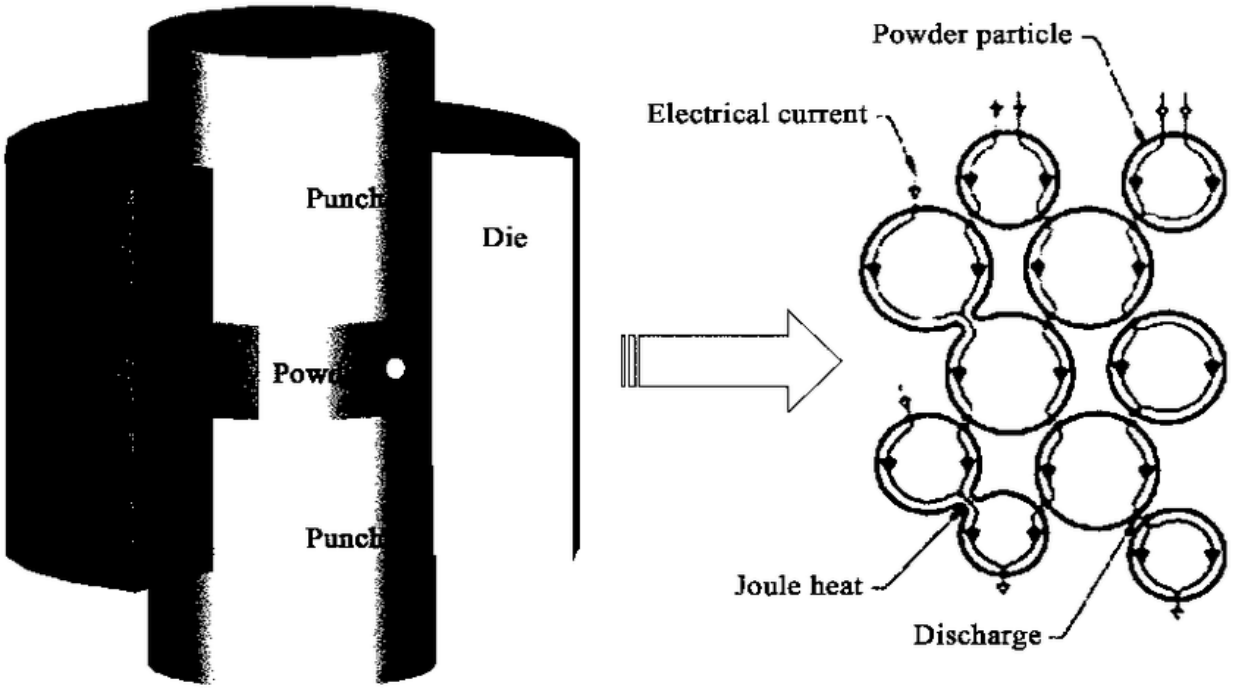

Figure 2.19: Sintering mechanisms among conductive powder particles during spark plasma sintering (SPS).

Figure 2.19 shows the sintering mechanisms on the conductive powder particles. The surface of the particles is cleaned by the formation of plasma and sparking phenomena at particles' contact points which cause the vaporisation and/or melting due to the localised high temperature up to 10000oC. Consequently, the neck formation is greatly enhanced by current effects. At last, the densification is accelerated by plastic deformation induced by the elastoplasticity effect given by the combination of applied pressure and electric current. The process from powder to fully dense bulk sample is fast in time. In the case of non-conductive specimens, the formation of plasma is challenging to be hypothesised. The non-conductive powders are heated from the die and punches [129].

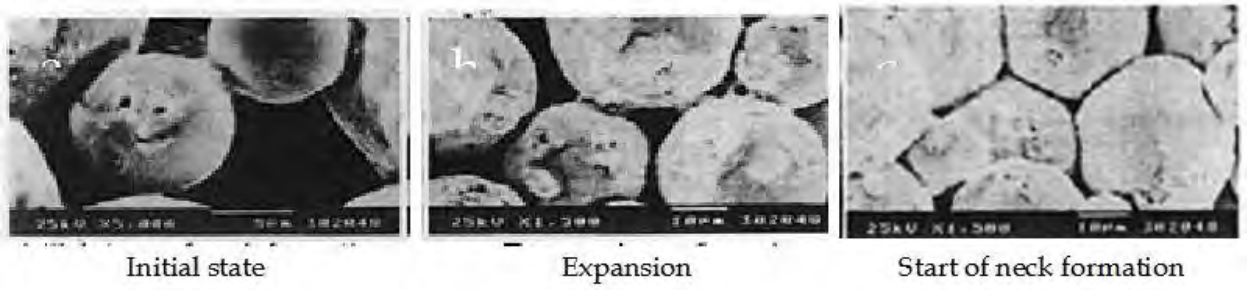

Figure 2.20: (a), (b), (c) Powder property during SPS sintering steps.

Figure 2.20a shows the behaviour in the initial stage of neck formation due to sparks in the plasma. The heat is immediately transferred to the centre of the spark discharge column to the sphere surface and diffused to quickly cool the intergranular bonding portion. As seen in Figure 2.20b, which shows several necks, the pulse energising method causes spark discharges one after another between particles. Even with a single particle, the number of positions where necks are formed between adjacent particles increases as the releases is repeated. Figure 2.20c shows the condition of an SPS sintered grain boundary plastically deformed after the sintering has progressed further.

2.4.4 Spark Plasma Sintering for Magnesium Alloy:

The properties of the Mg alloys produced by conventional production methods such as casting have been restricted due to constraints posed by limited grain refinement and solid solubility of the desired alloying elements, and formation of intermetallic phases, etc. Non-conventional manufacturing technologies have the potential of producing alloys exceeding the strength of alloys produced by conventional methods, which open up avenues for cost saving in automotive, aerospace, and several other industrial applications by developing lightweight materials with higher achievable strength [125], [130], [131].

Non-conventional manufacturing techniques such as sputter deposition and rapid solidification benefit from achieving high solid solubility of the alloying elements and high corrosion resistance and strength. However, engineering applications of these techniques are limited because of challenges in upscaling the production. Several processing techniques involving severe plastic deformation (SPD) for material strengthening are equal-channel angular pressing (or extrusion), high-pressure torsion, and surface mechanical attrition treatment [130]. SPD techniques produce alloys with refined grains (<1 μm), containing a significant fraction of grain boundaries that hinder dislocations' movement and improve strength. Mechanical alloying or high-energy ball milling (HEBM) has been used to synthesise many materials, including oxide dispersion strengthened materials, ceramics, intermetallic compounds, nanocomposites, and high entropy nanocrystalline alloys. HEBM has also been reported to induce grain refinement below 100 nm and produce supersaturated solid solutions [130]. Recent work on Fe and Al-based alloys have demonstrated that HEBM could improve corrosion resistance and strength. Grain refinement below 100 nm, extended solid solubility of alloying elements, and uniform dispersion of refined second phases was attributed to enhanced corrosion resistance and mechanical strength.

High-energy ball milled (HEBMed) alloys are often in powder form, which needs to be consolidated into fully dense alloys to investigate their properties and further engineering applications. Most of the consolidation methods need exposure to high temperatures. Grain growth and decomposition of a supersaturated solid solution to the thermodynamically stable phases upon high-temperature exposure is inevitable; however, the kinetics can be impeded by choosing lower temperatures [130], [131]. Therefore, consolidation methods requiring low temperature and short time seek to consolidate the HEBMed alloys.

Spark plasma sintering (SPS), a widely used technique in consolidating powder materials including metals, ceramics, and composites, results in densification in a shorter time and lower temperatures. The process of SPS involves the densification of powder materials by applying an electric current

in the range of 100 A/cm^2; however, only a fraction of it flows through the material. The electric current heats the material due to the resistance offered by the powder contacts and the space between them. It allows a heating rate of up to about 1000 K.min^{-1} compared to hot pressing, which offers 5–10 K.min^{-1}. SPS allows fast densification at lower temperatures in contrast to conventional sintering methods, resulting in the retention of nanocrystalline structure, non-equilibrium alloys produced by HEBM and associated properties [130]. The rapid heating rates allow densification by minimising any surface diffusion of the materials during heating that is suggested to hinder densification. This process also helps retain the refined grain size, obtained after significant refinement is achieved due to milling [81], [131]. The grain growth can be minimised by controlling the consolidation parameters, e.g., time and temperatures. Therefore, there is merit in optimising the SPS process parameters to produce fully dense nanocrystalline alloys with extended solid solubility. SPS has been applied to commercial Mg alloys such as AE42, AZ3, and AZ91. Bautista et al. investigated the role of sintering temperature on density and corrosion properties. They reported that an alloy with the highest sinter density (at higher sintering temperature) showed the best corrosion resistance. [132] investigated the effect of pore characteristics on microstructure, mechanical properties, and corrosion resistance of selective laser sintered porous Ti-Mo alloys and reported a lower corrosion resistance for high porosity samples.

2.5 Scope of Work

In the present study, a complete new Mg alloy was developed by SPS combining the personal effects of alloy elements such as Zn, Er, and Ce. It is expected to improve mechanical behaviour, corrosion properties, and x-ray visibility keeping in mind its application in implantable biomedical devices and looking into the design criteria, e.g., hardness, radiopacity, and accelerated corrosion rate.

Chapter 3

Material Selection and Alloy Design

3.1 Introduction:

Material selection is an essential phenomenon for theoretical and practical interest. For designing new alloys, the properties of all the materials need to follow the requirements, but some are not acceptable. Generally, for material selection methods, it is necessary to have a unique synergy of theoretical knowledge and practical experiences data. A systematic study on a quantitative approach for material selection, including analytical and computer-aided processes (in this case Xmudat software), is provided in this section.

3.2 Material selection :

Selection of material and there solubility limit is very important for the implat material as the solubility of each material affects the toxicity of the final product. The selection route is described below:

a. Mg exhibits non-toxicity and can even stimulate hard tissue recovery after implantation in the human body. This characteristic makes Mg and some alloys promising candidates for biodegradable implant applications. So, 67 wt% of Mg is alloyed with three different elements.
b. The utilisation of Er gives excellent biocompatibility and a high mass X-ray absorption coefficient. Moreover, Er has recently become the focus of attention because it exhibits good X-ray attenuation properties and is inexpensive compared to gold. Er can improve strength and corrosion resistance by forming a solid solution, and it has a solubility of 18.5 wt% (Figure: 3.2a) in Mg. Here 20 wt% Er was used for getting good visibility under x-ray.
c. The tensile strength and elongation achieved from Mg–Zn alloys are suitable for implant applications. Moreover, no adverse effects of hydrogen generated by degradation in vivo had been observed. Also, no adverse effects caused by the release of zinc were detected, and Zn can Transform impurities (Fe, Cu, Ni) into the harmless intermetallic compound. It has a solubility of 6.2 wt% in Mg (Figure: 3.2b) and is toxic above 2.5wt%. So, 2 wt% Zn was selected for minimising the harmful effect by maximising the mechanical suitability.
d. The second phase of Ce exhibits a continuous network along the grain boundaries. It tends to be thermodynamically stable than the Mg matrix, leading to an acceleration in the cathodic reaction and inhibition in the anodic reaction. It has a solubility of 25wt% Ce in Mg (Figure: 3.2c), but only one wt% Ce was used to improve strength by ppt hardening in the Mg matrix**.**

(a)

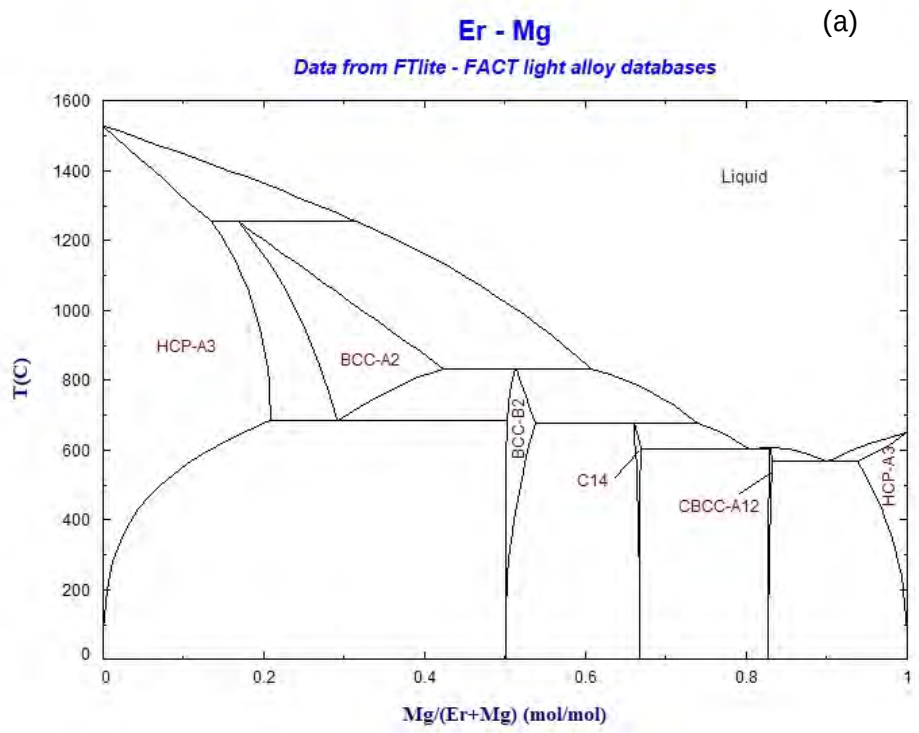
Er - Mg
Data from FTlite - FACT light alloy databases
T(C)
Mg/(Er+Mg) (mol/mol)
Liquid
HCP-A3
BCC-A2
BCC-B2
C14
CBCC-A12
HCP-A3

(b)

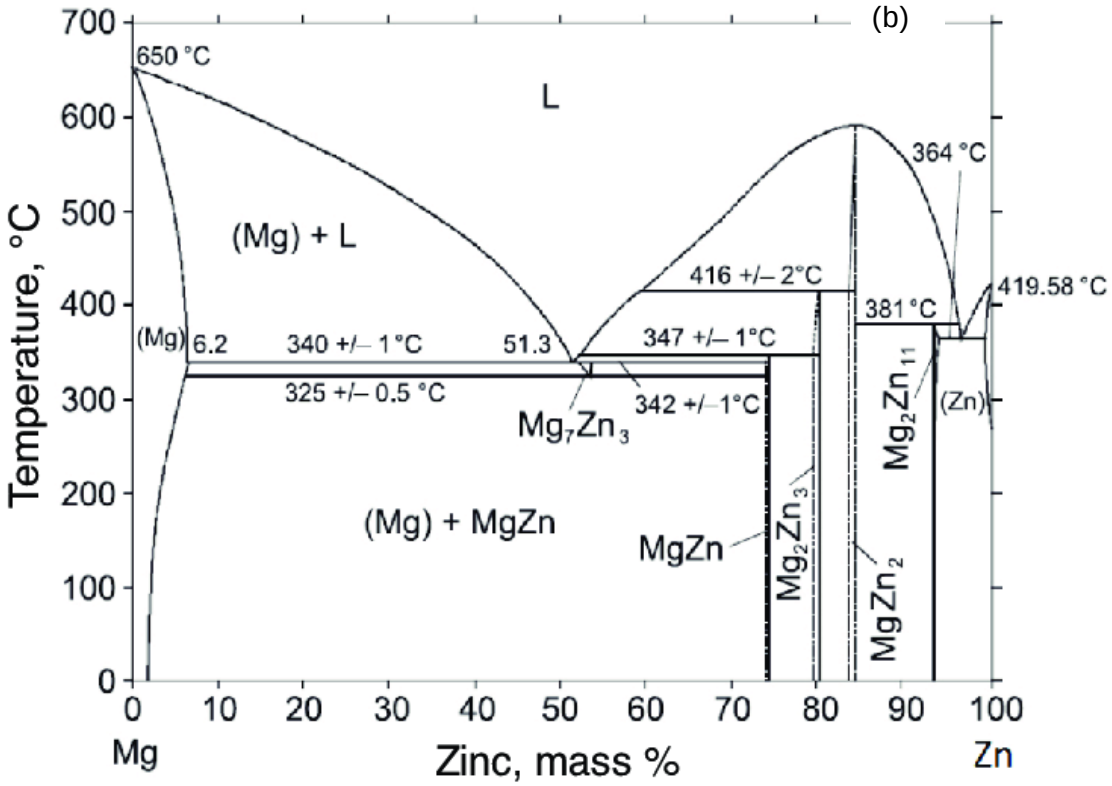
Temperature, °C
Zinc, mass %
Mg
Zn
650 °C
L
(Mg) + L
(Mg)
6.2
340 +/– 1 °C
325 +/– 0.5 °C
51.3
342 +/– 1°C
347 +/– 1°C
416 +/– 2°C
364 °C
381 °C
419.58 °C
(Zn)
Mg7Zn3
(Mg) + MgZn
MgZn
Mg2Zn3
MgZn2
Mg2Zn11

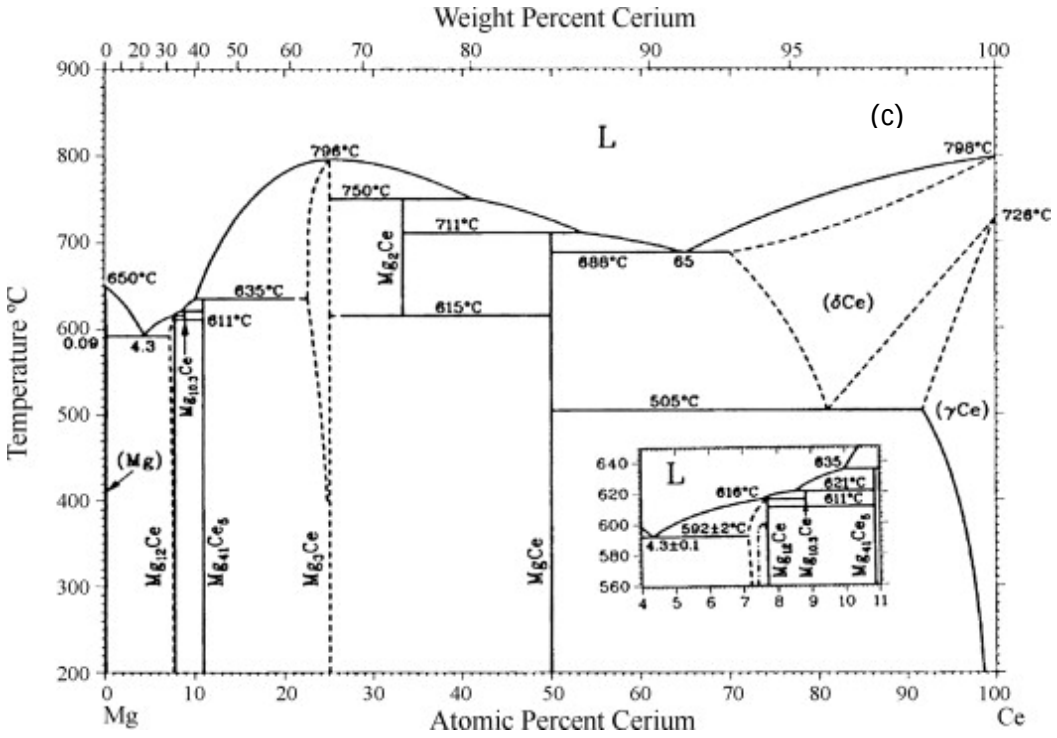

Figure 3.1: Phase diagram (a)Mg-Er, (b)Mg-Zn, (c)Mg-Ce

Table 3. 1- Composition and Powder Weight

Material	Weight Percentage	Powder weight (multiplying factor 15) for 15 samples
Ce	1%	0.15
Zn	2%	0.3
Er	20%	4.5
Mg	67% (Balanced)	10.05
Total	100%	15 gm

Table 3.1 explains the powder quantity for the preparation of 15 samples . All powders' weight percentages were taken depending on their cytotoxic behaviour, alloying characteristics, corrosion properties, and x-ray attenuation coefficient from xmudat software. The rest of the percentage was balanced by magnesium powder.

3.3 Measuring attenuation coefficient using xmudat:

For comparing total attenuation (cm^2/g) concerning photon energy (keV), graphs were plotted for all individual elements in xmudat software. As the maximum material limit for this software is up to six (06), curves of four elements were calculated very quickly. This entire process is described in this section as follows.

1. The application file was first run from the zip folder, and data setup was selected.

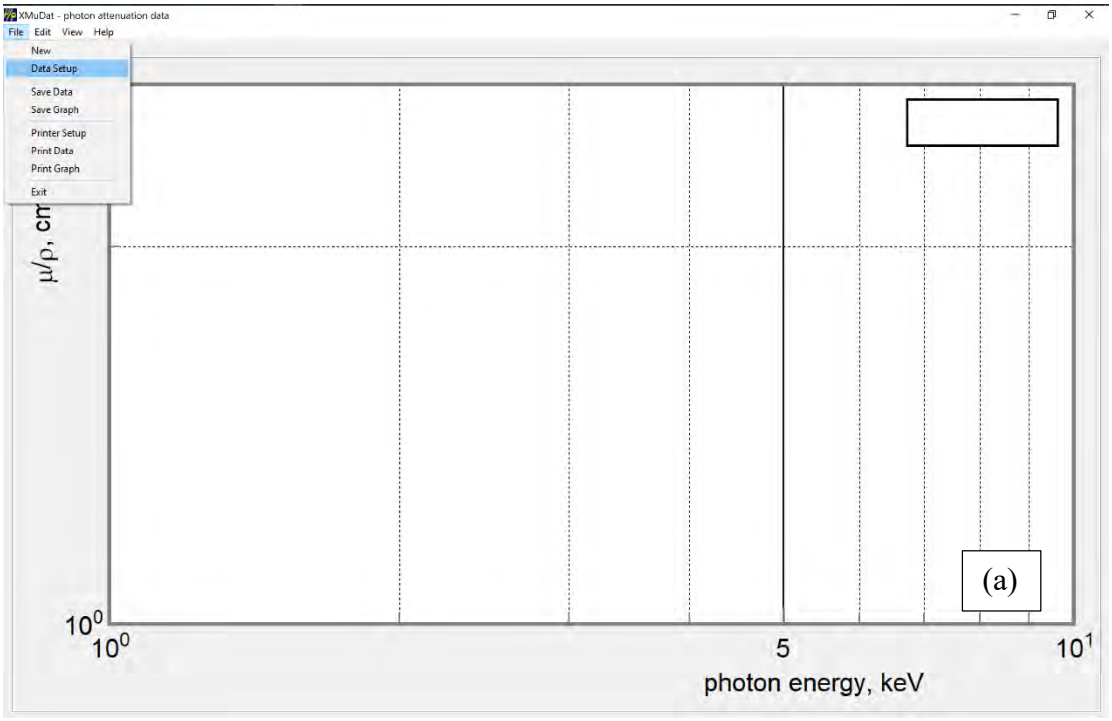

2. Then, the add option was selected from tab #1

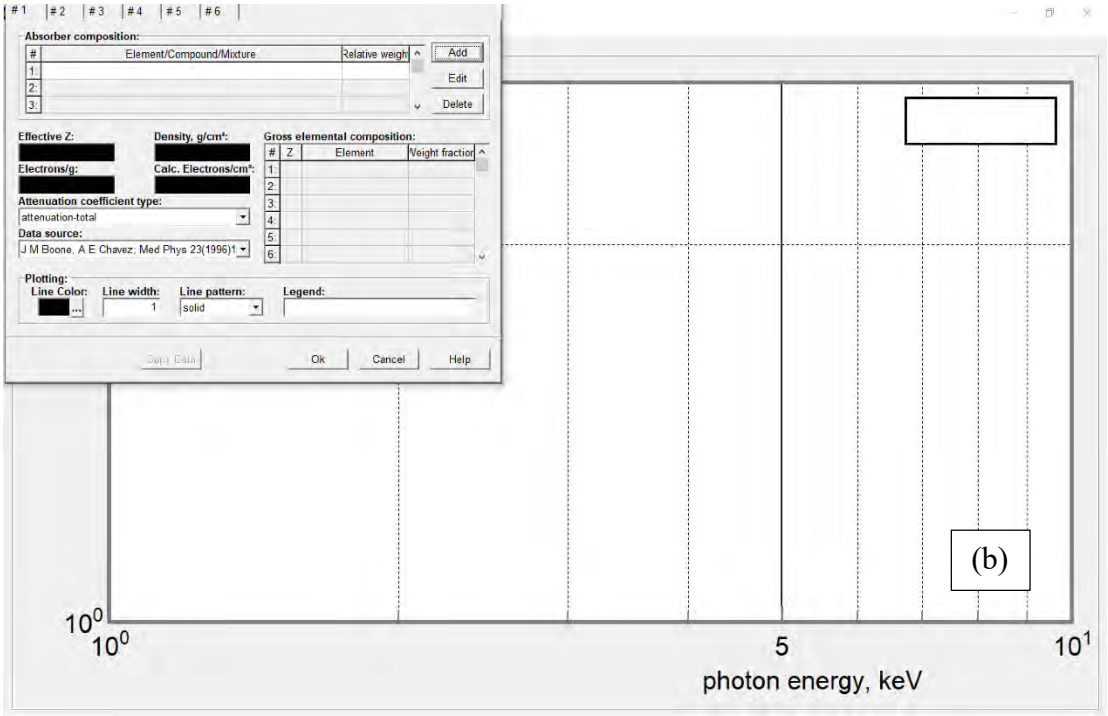

3. The total attenuation Magnesium was selected from the element/compound/mixture option.

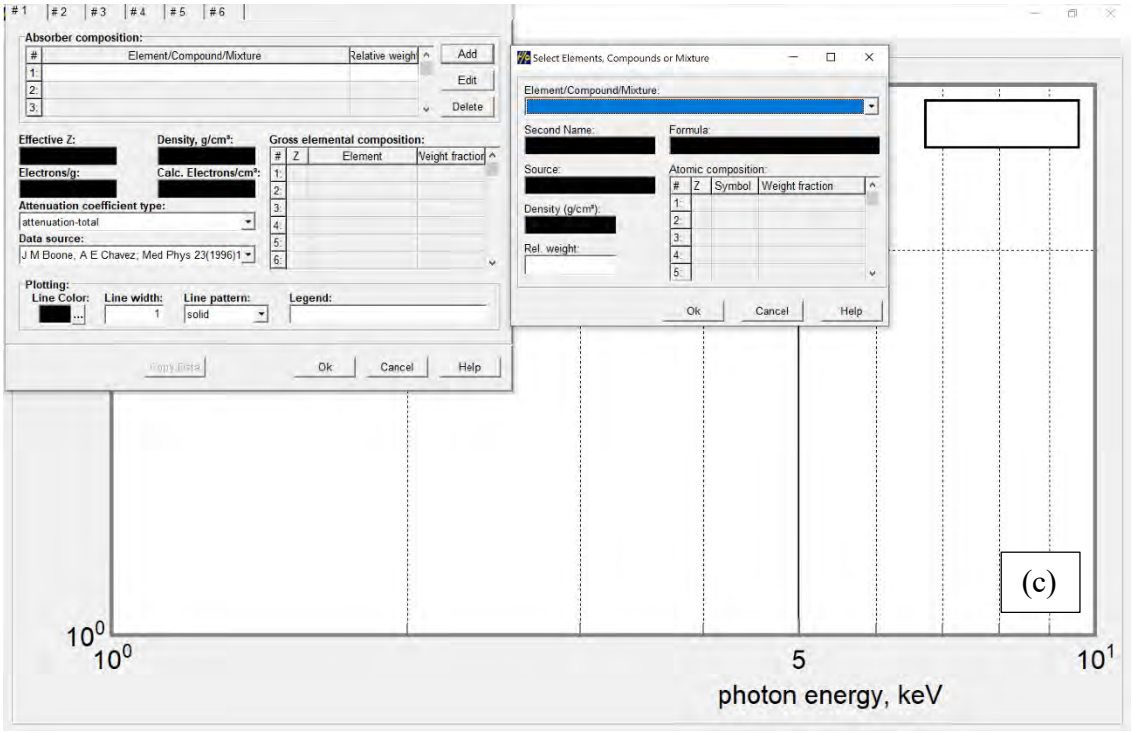

4. Relative weight was fixed as 100, and the Ok option was selected.

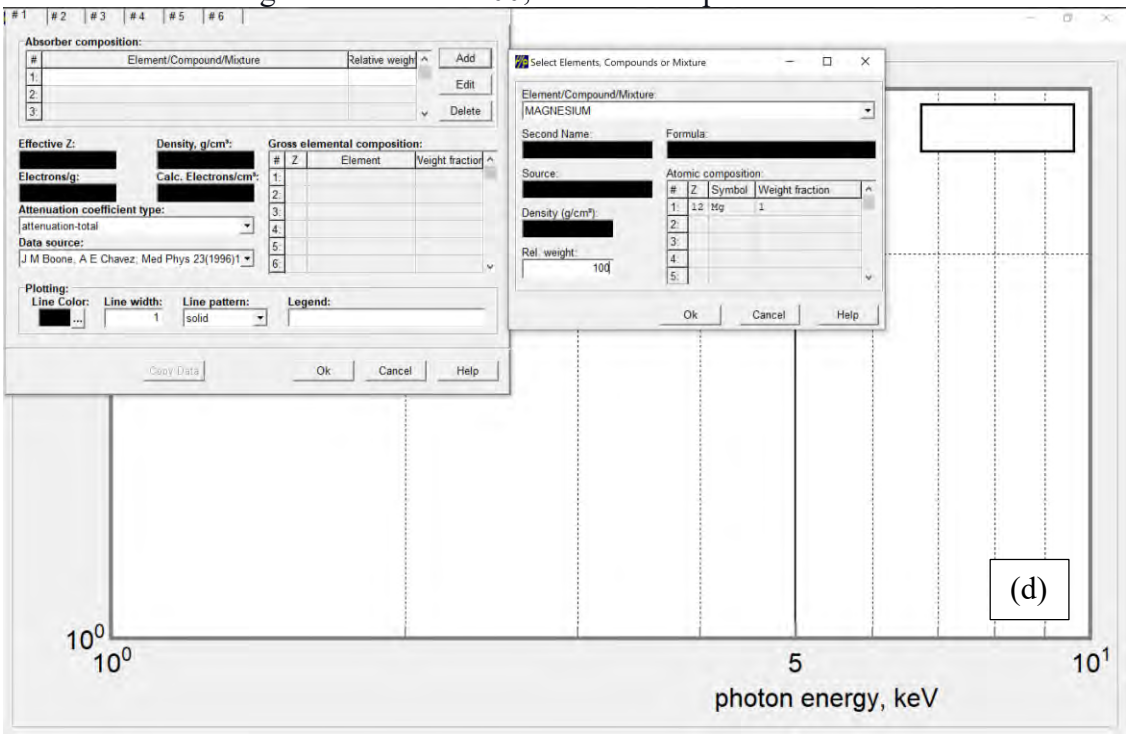

5. Then line colour, width, pattern, and legend were fixed.

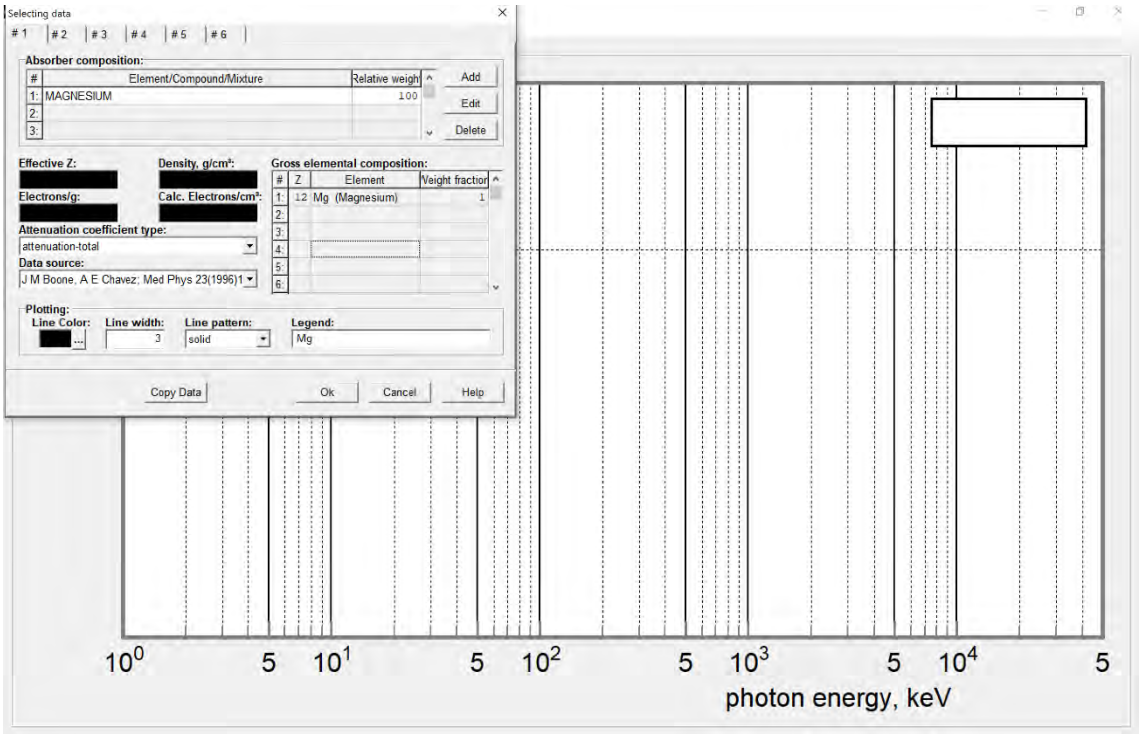

6. Then photon energy vs total attenuation curve of Mg was found.

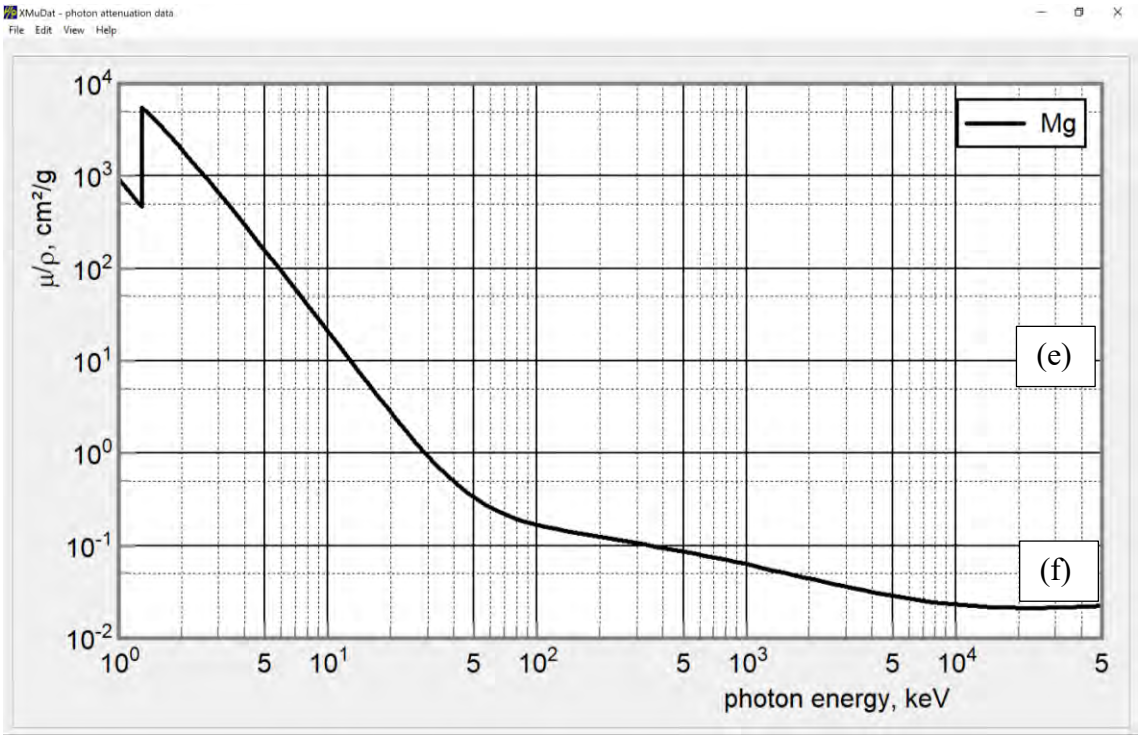

7. For the next curve of Erbium, the data setup was selected.

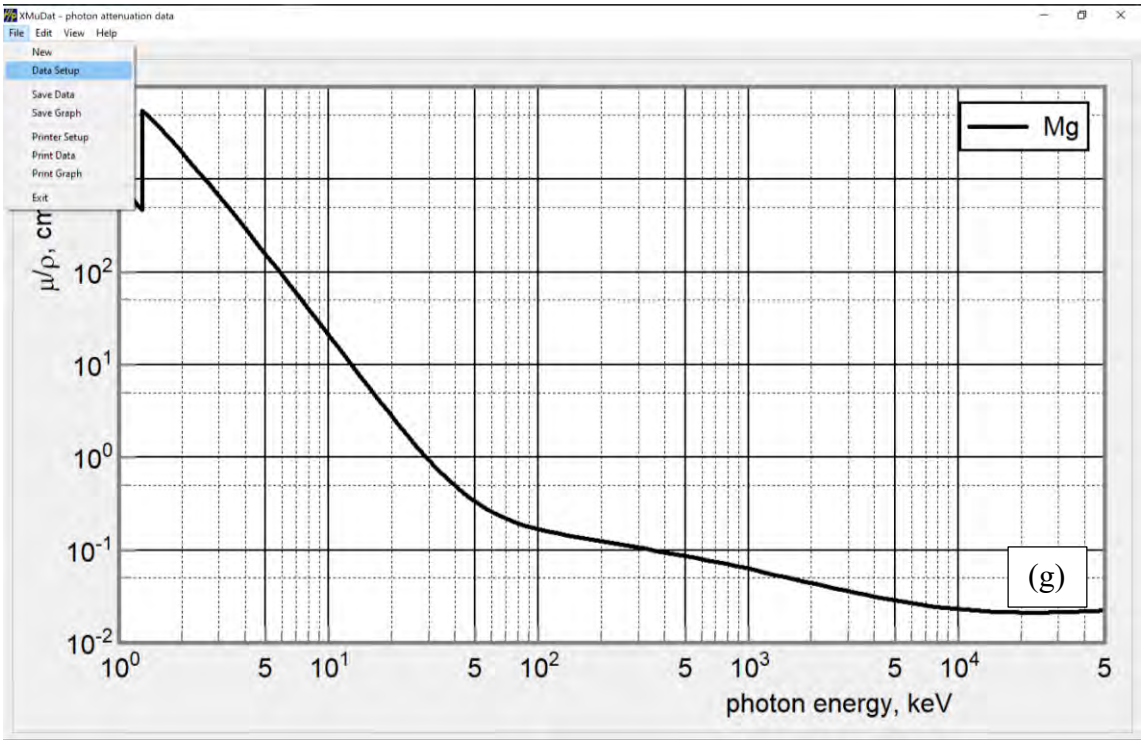

8. Then add option was selected from tab #2

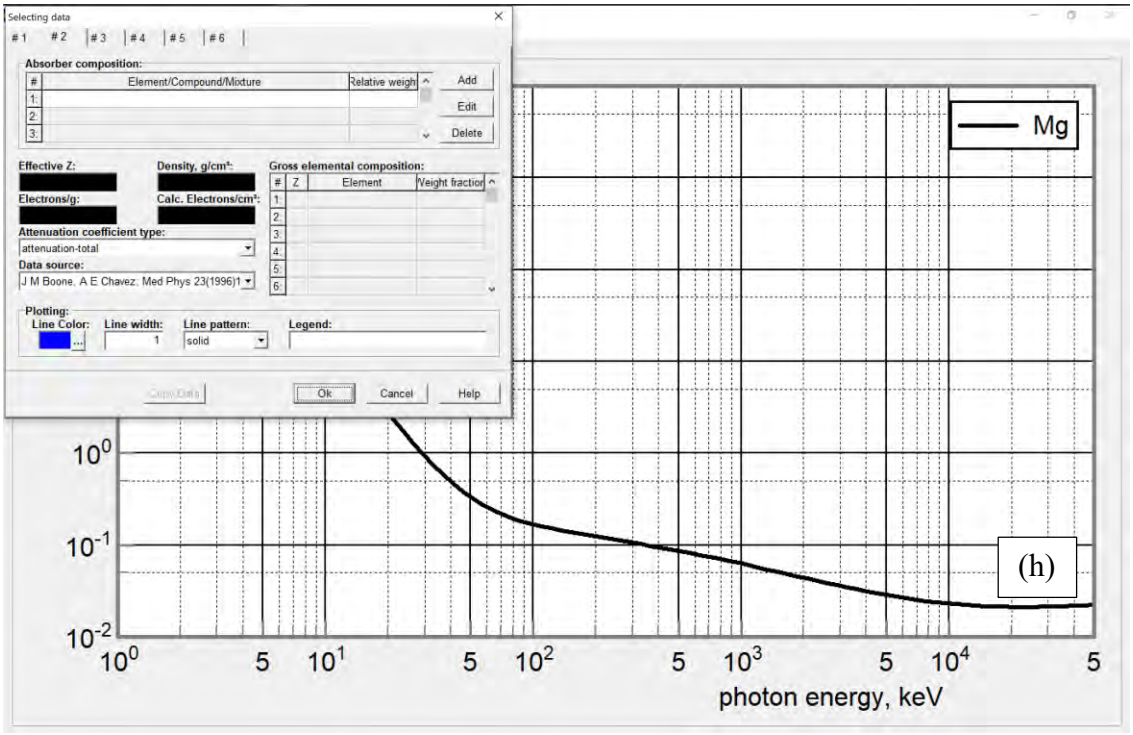

9. Erbium was selected from the element/compound/mixture option.

10. Relative weight was fixed as 100, and the ok option was pressed.

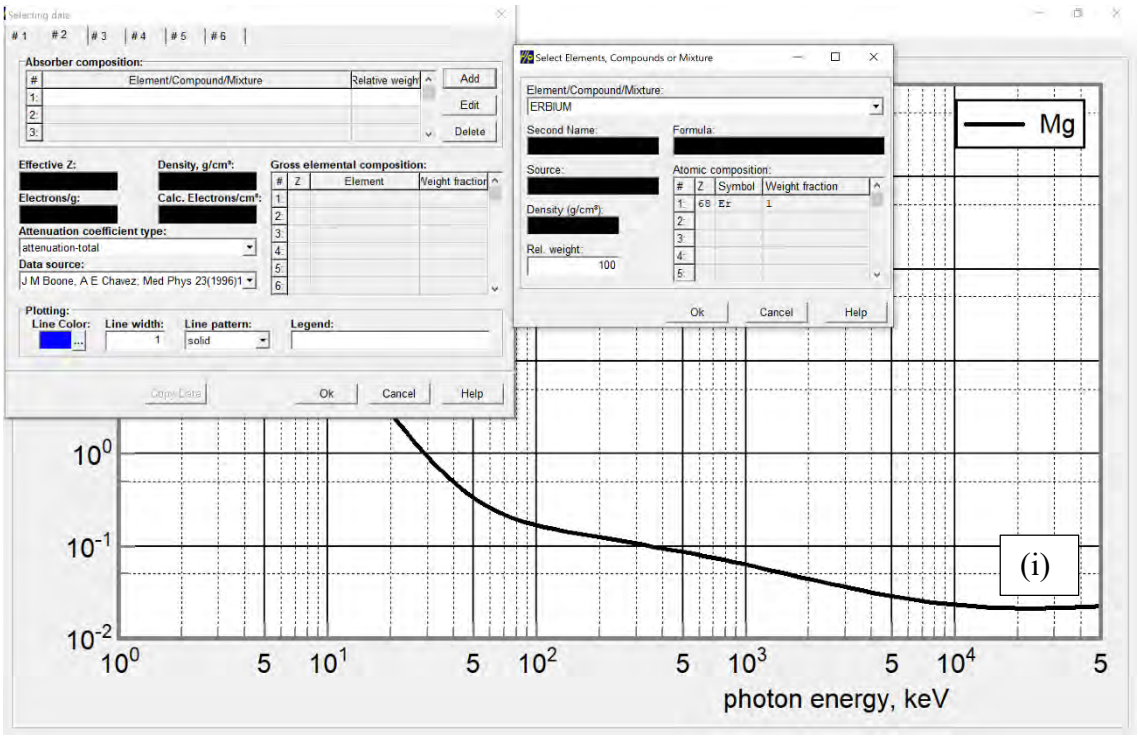

11. The line colour, width, pattern, and legend were fixed. Then the ok button was pressed.

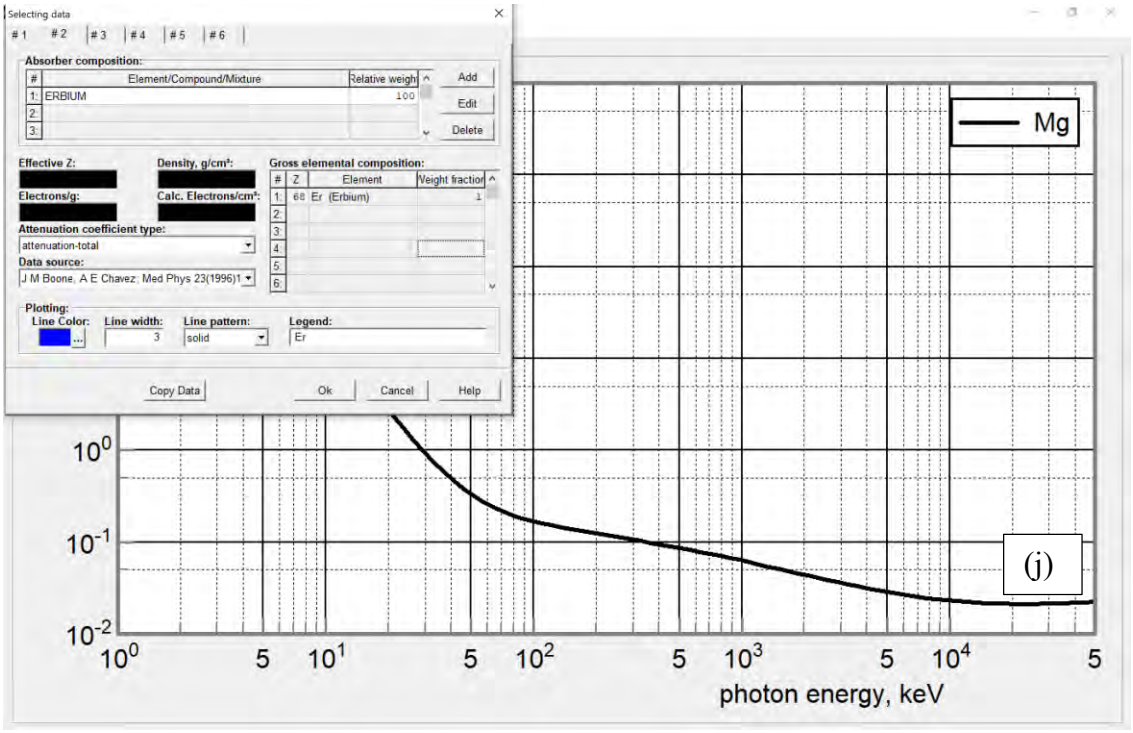

12. Then, the photon energy vs total attenuation curve was formed.

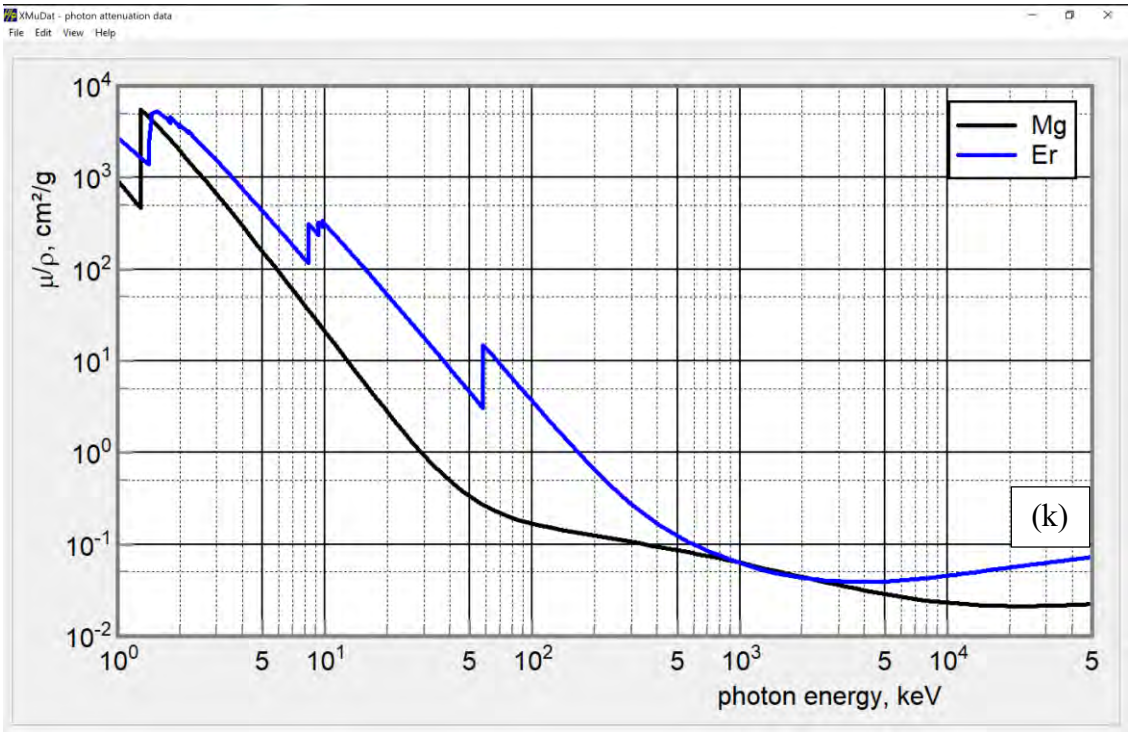

13. The data set up was selected once again for the third zinc curve.

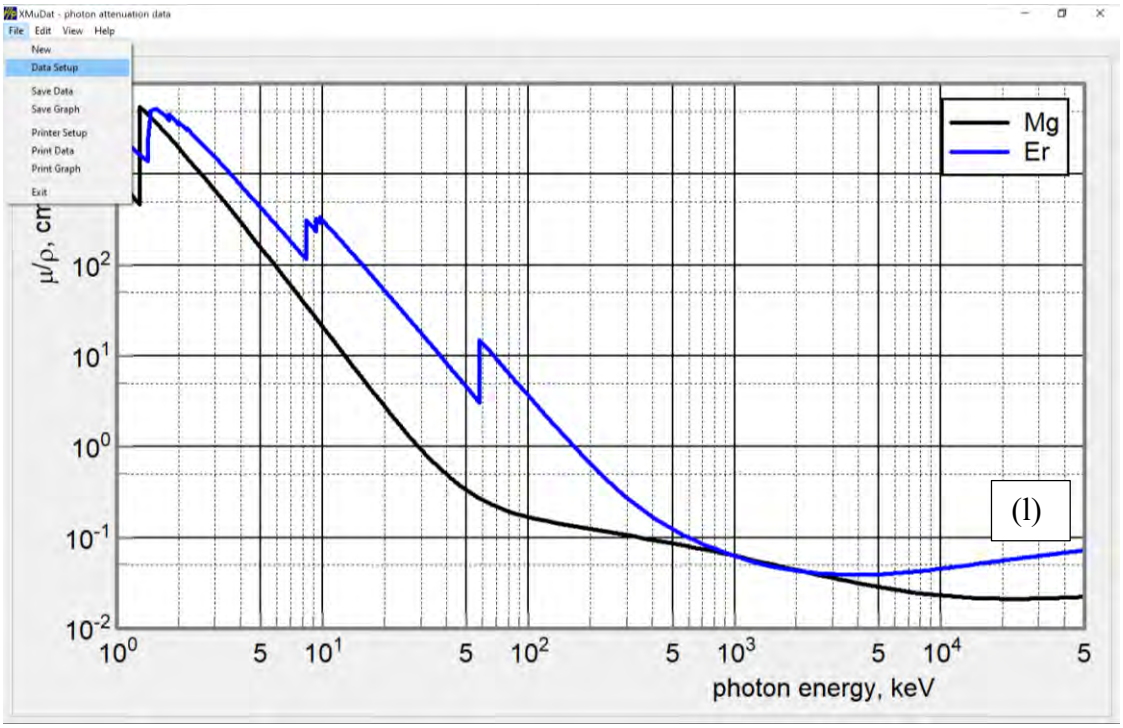

14. Add option was selected from tab #3

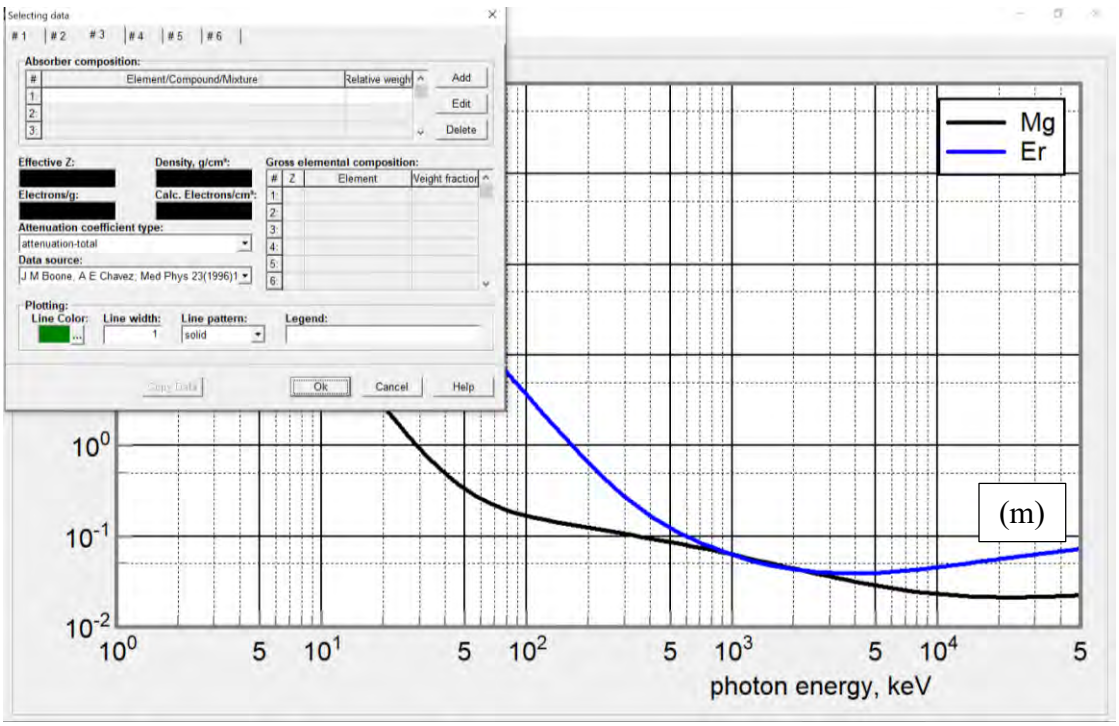

15. Zinc was selected from the element/compound/mixture option. The relative weight was made 100, and the ok option was selected.

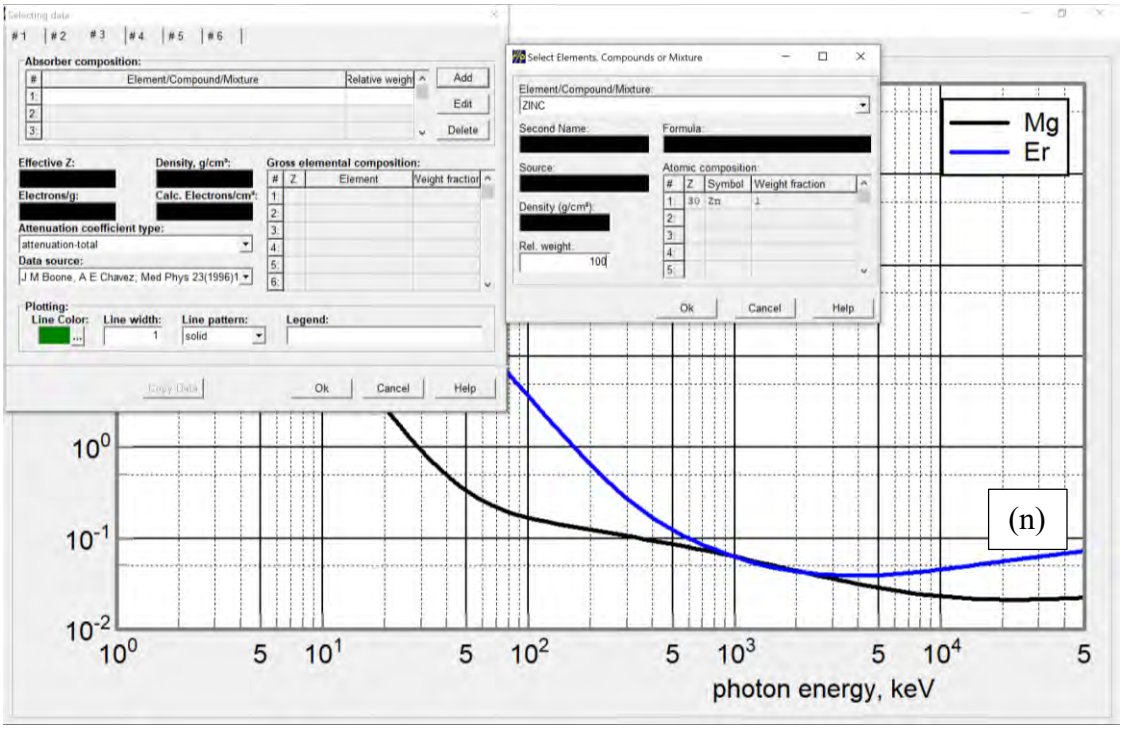

16. Then, the line colour, width, pattern, and legend were selected, and the ok option was selected.

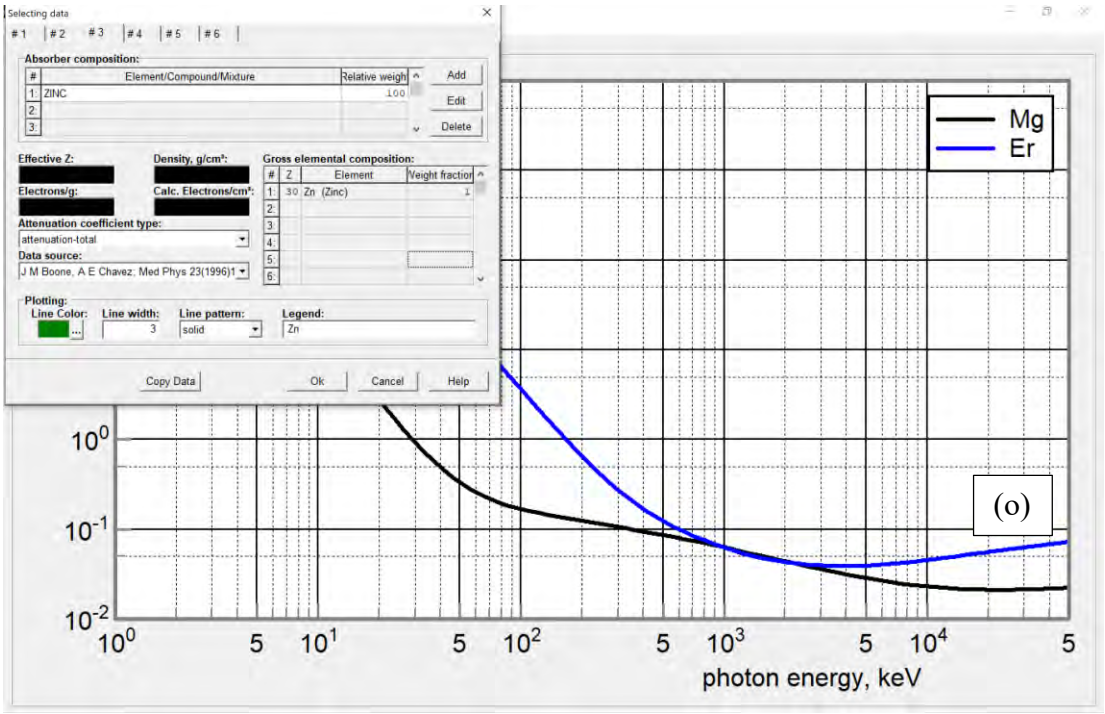

17. Then, the third curve of Zn appeared with the previous ones.

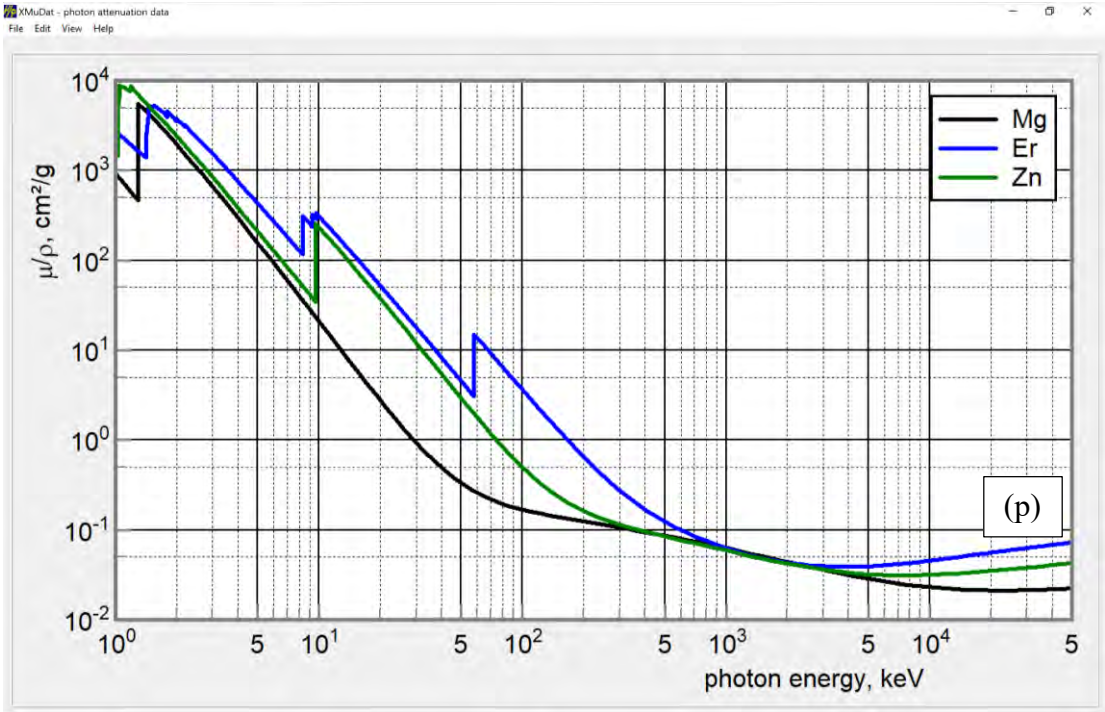

18. For the last curve of Cerium, a data selection option was selected.

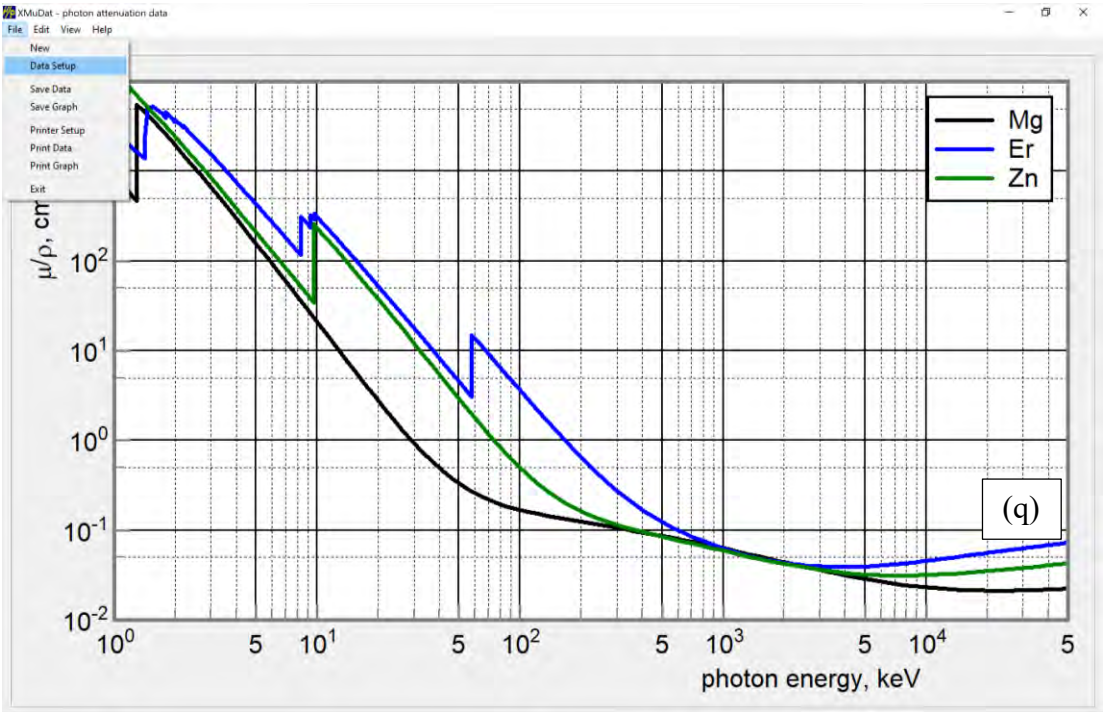

19. Add option was selected from the #4 tab.

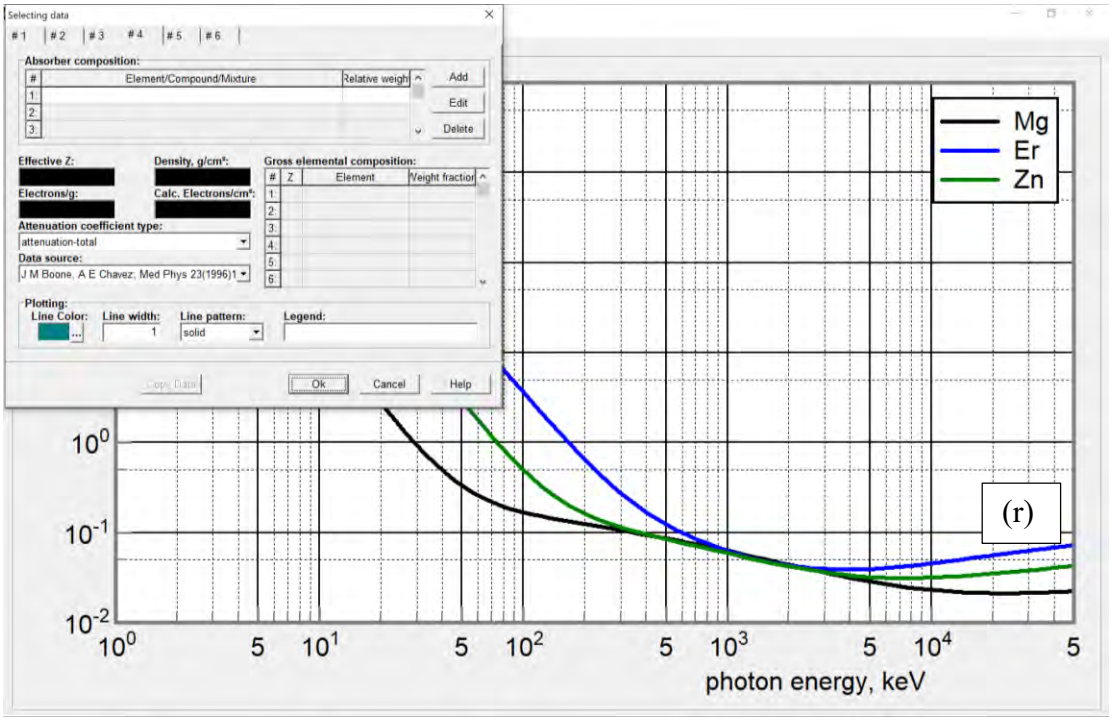

20. Cerium was selected from the element/compound/mixture option. Relative weight was fixed as 100, and the ok option was specified.

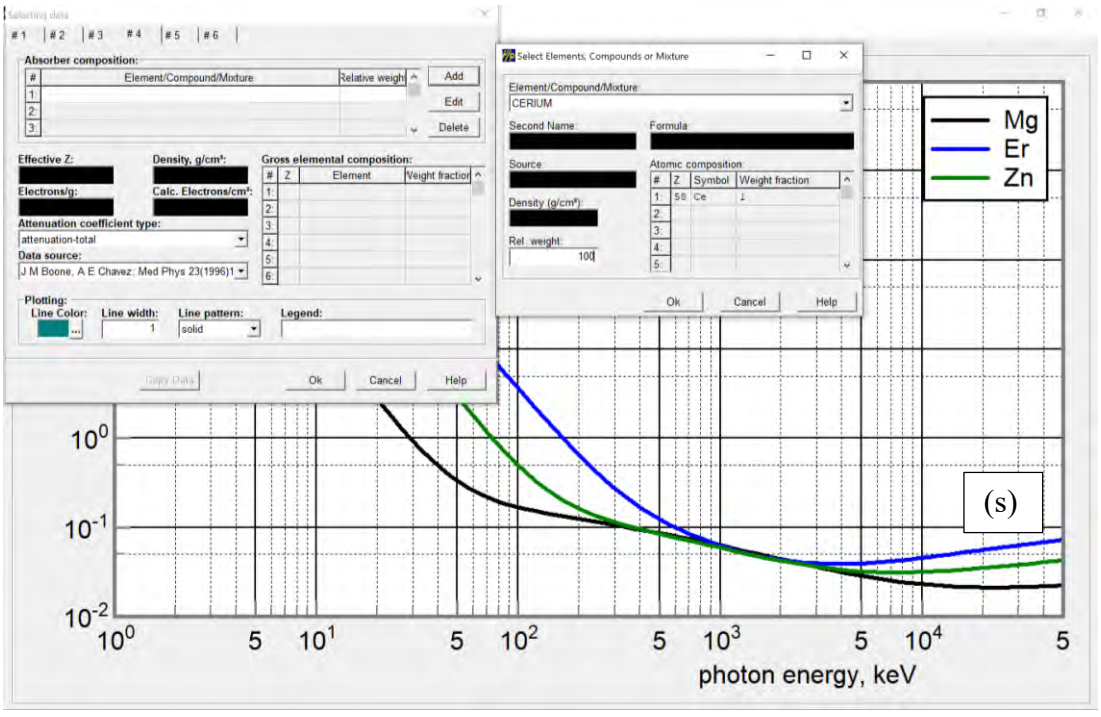

21. Then line colour, width, pattern, and the legend was fixed.

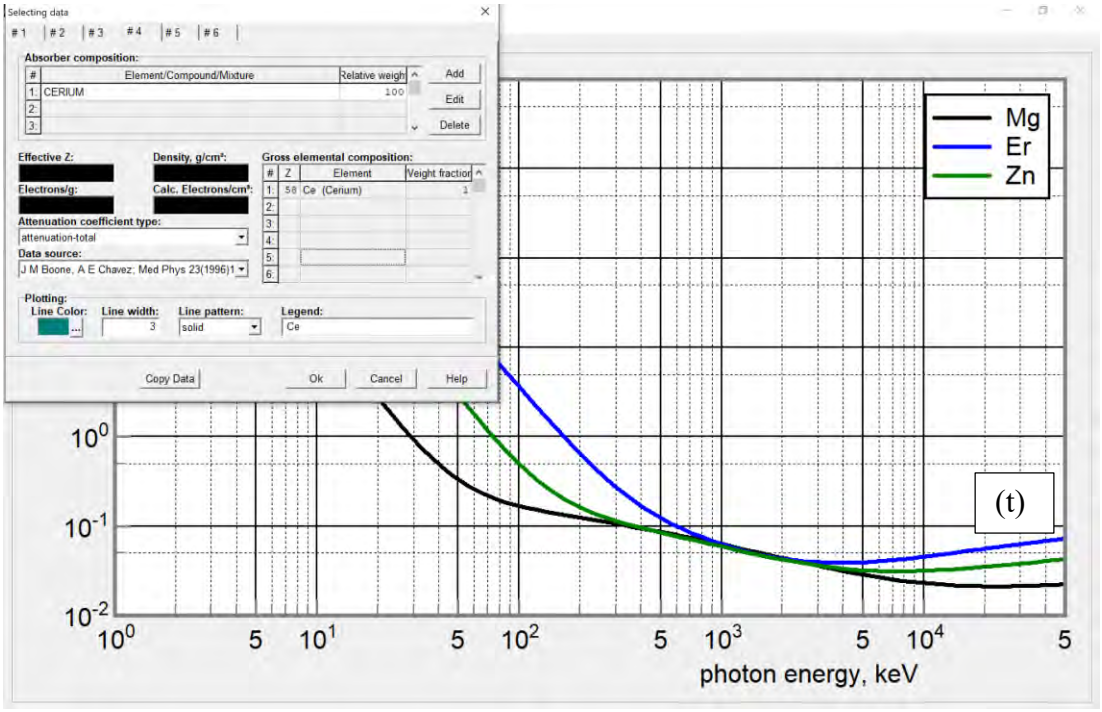

22. Then Ce's photon energy vs total attenuation curve appeared with the other curve.

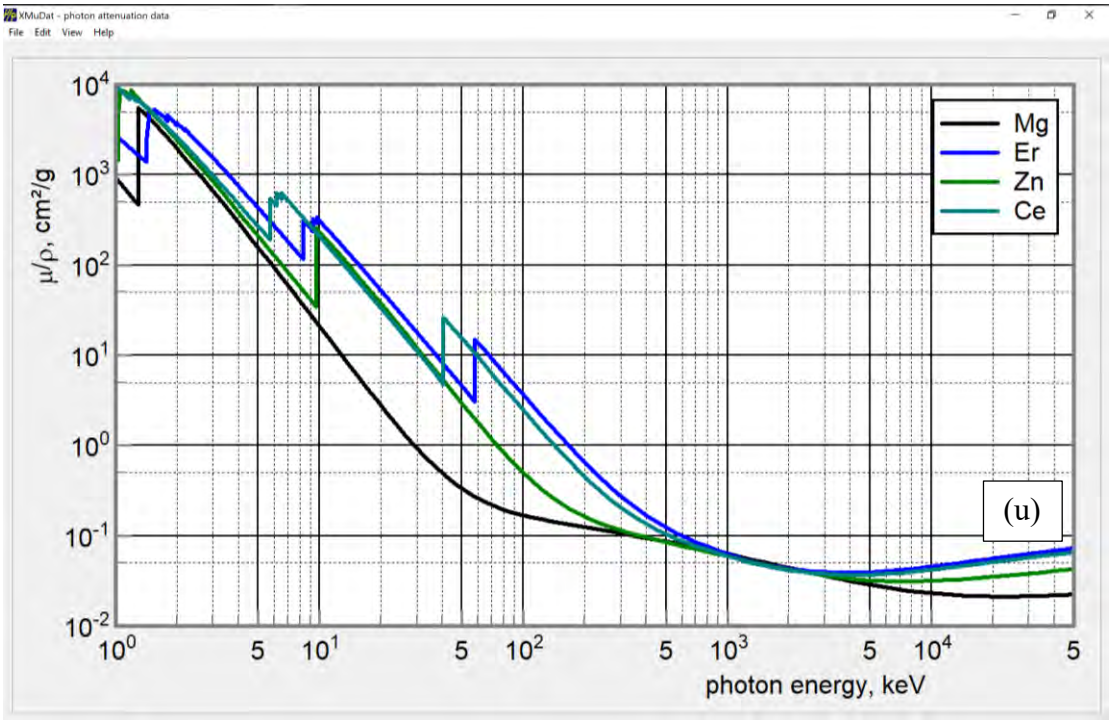

Figure 3.2: Total x-ray attenuation vs photon energy curve; (a)-(u)

Chapter 4

Experimental Procedure

This chapter discusses experimental steps that were followed during this research work. It describes magnesium alloy's synthesis and sintering techniques, heat treatment, and characterisation methods followed for complete characterisation and property analysis. This section also evaluates and justifies the parameters used in investigation and characterization.

The following experimental procedure was conducted in the current work:

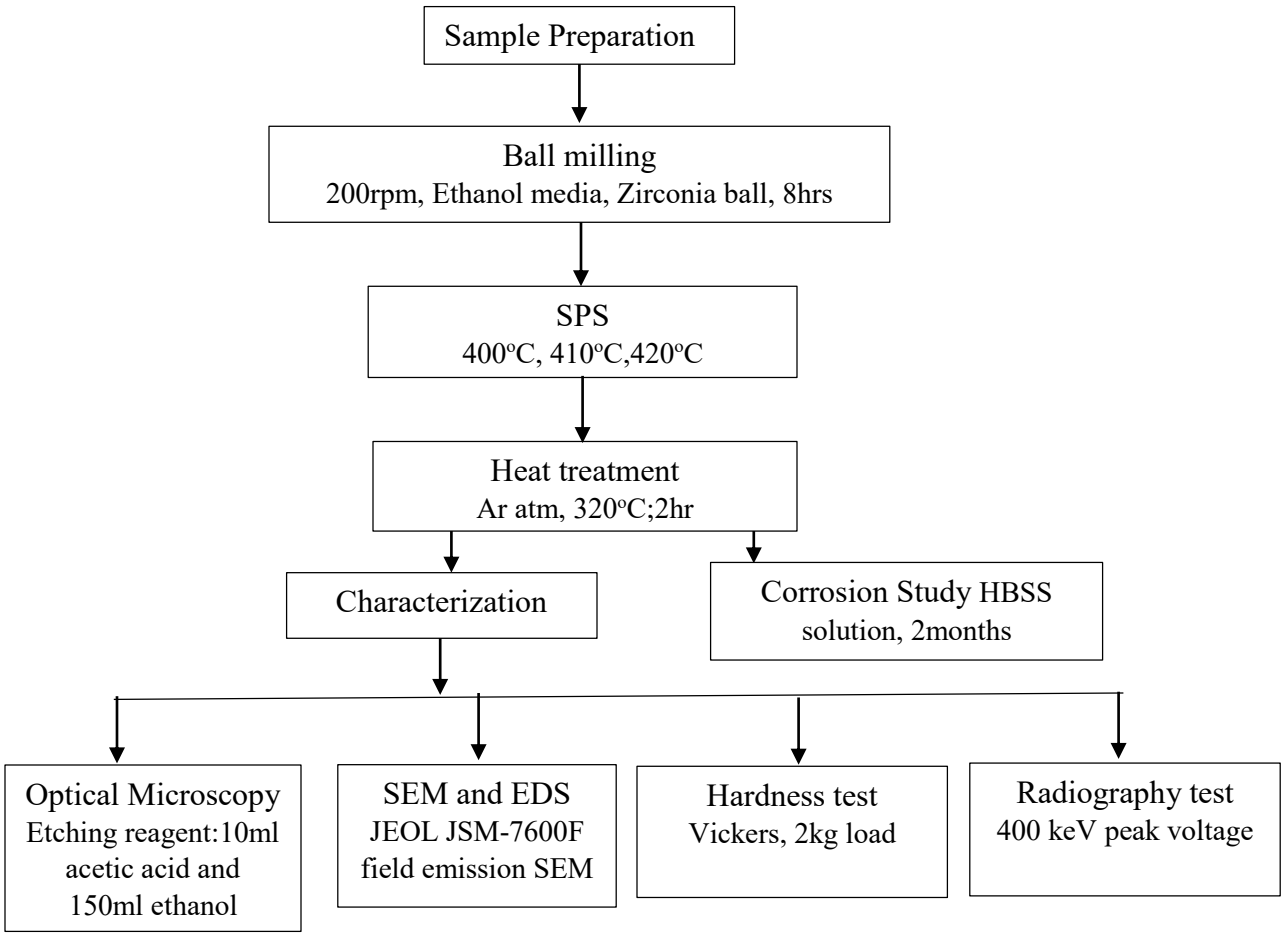

1. Powders were mixed in a controlled environment using alcohol media in a glove box. After mixing and homogenisation in ball billing, the powder mix was dried with a steady heat source in the glove box.

2. 15(fifteen) samples were prepared using the SPS method from pure Mg and pre-determined Zn, Er, and Ce powder.

3. Then, the samples were heat-treated in a tube furnace in an argon environment.
4. Optical micrographs were performed to identify the grain size of the samples.
5. SEM and EDS analyses were carried out to examine the distribution of the elements in the sintered samples.
6. The vickers hardness test was performed under the significant load (2 kg) for 10 seconds.
7. X-ray radiography test was performed in soft x-ray range to identify the visibility of the alloy under medical x-ray range.
8. The weight loss method performed an accelerated corrosion study in a mimic body fluid (HBSS modified) for two months.

4.1 Alloy preparation:

The presented section focuses on preparing samples by the SPS technique. The known quantity of dried and milled powder sample was taken in a cylindrical die, lined with graphite sheet, which easily removes the sintered compact. The die containing the powder sample was placed inside the SPS chamber. The specific pattern (time-temperature data) was set for the experiment to follow and, after that, maintain the required atmospheres as a vacuum inside the chamber. High DC Pulse is passed between graphite electrodes, and axial pressure is simultaneously applied from the sintering cycle. After the sintering, the power is turned off, and the sample is allowed to cool. All the procedures are described below in detail.

4.1.1 Sample powder mixture preparation:

At first, chemistry was selected based on the solubility of each element in the magnesium. According to the phase diagram of Er-Mg, Zn-Mg, and Ce-Mg (Figure 3.1), 67wt% of Mg powder, 2wt% of Zn powder, 20 wt% of Er powder, and 1wt% of Ce powder were weighed and mixed with grinding media (zirconia ball) and ethanol. All the powders were mixed in a rotary ball mill for 8hrs. After that, the sample media and alcohol were separated by settling for 24hrs in the beakers and pouring the alcohol in a separate beaker. The mixture was kept on a hot plate for complete drying, and the media was removed by picking with forceps. As magnesium is highly flammable in powder form, all the process has been performed inside the glovebox keeping the environment under zero oxygen.

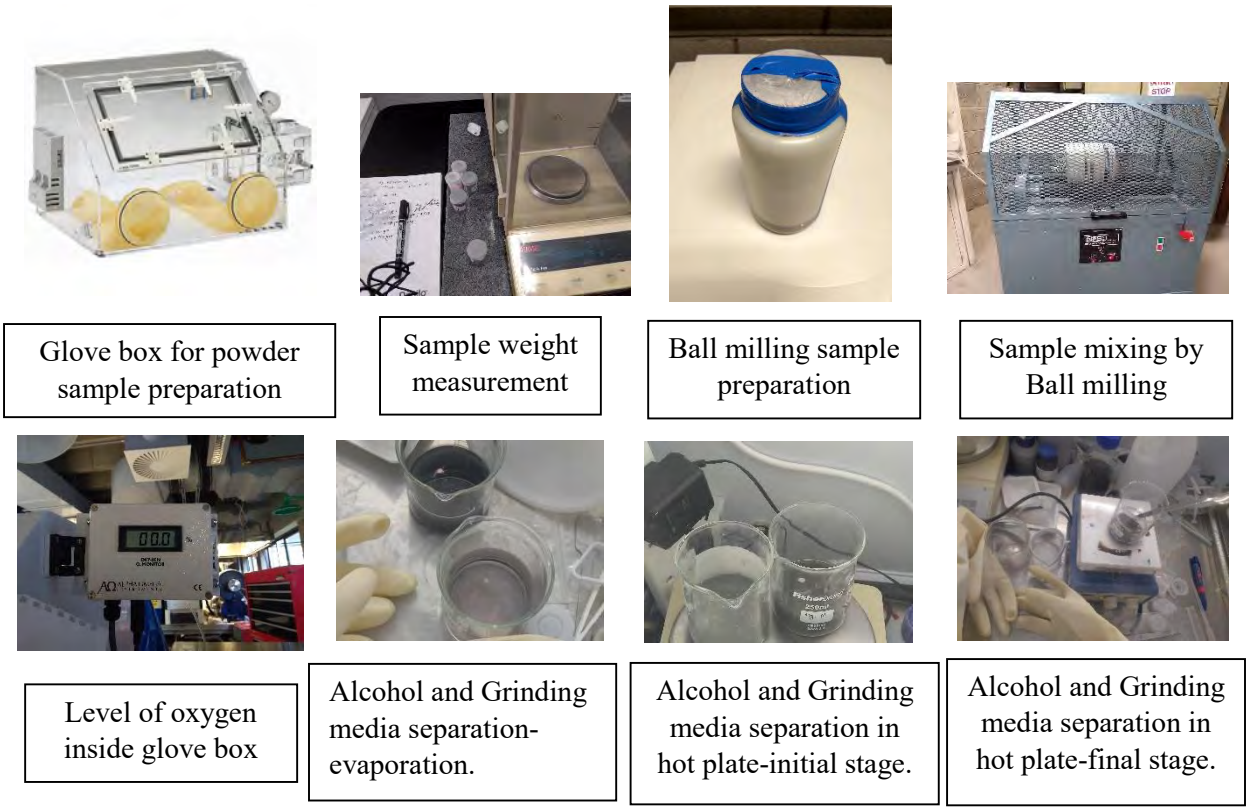

Figure 4.1: Steps of sample preparation for SPS

4.1.2 Die preparation and sample pouring inside die:

1. For each 10mm punch dia, 0.2mm thick graphite paper was cut into 40mm length and 38mm width. Conducting nature of carbon paper is helpful to transmit electric current uniformly throughout the powder taken inside the mould for sintering.
2. One face of each punch was coated with a BN (boron nitride) release agent on the face that was in direct contact with the powder during sintering.
3. Graphite paper was used to make a liner for the die's inner diameter (ID) to protect it and the sample from the deterioration of the sintering process.
4. The same graphite paper was used to make disks used as spacers between the powder and both punch faces.
5. One punch was inserted into the die cavity from the bottom side, and the powder was carefully transferred to the die cavity.
6. The die side was gently tapped to allow powder to settle.

7. The remaining punch was inserted into the die. Then it was pressed with hand to pre-compact the powder in the die. The powder column was tried to keep as close as possible to the centre of the die cavity.

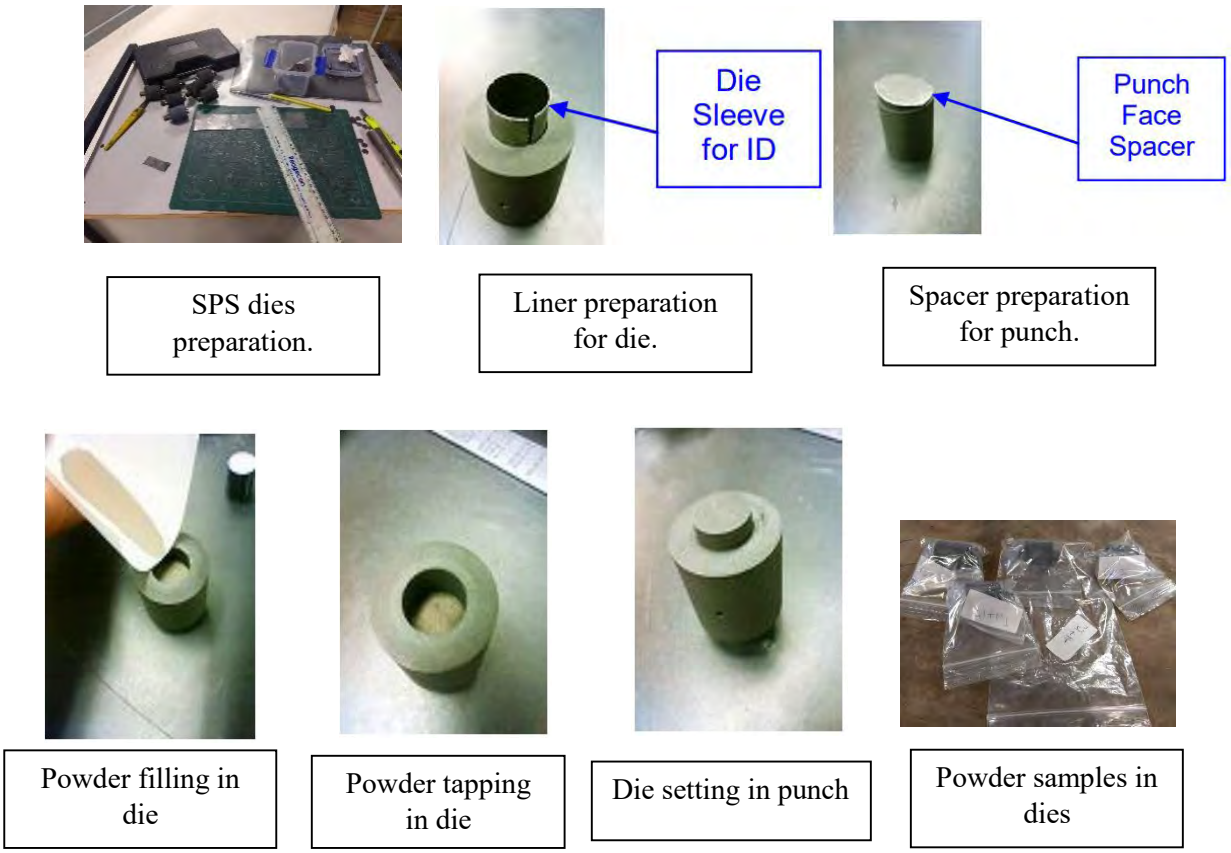

Figure 4.2: Die-punch preparation for SPS and sample pouring.

4.1.3 Temperature and pressure selection:

Temperature is an important process parameter in the consolidation of powders during SPS. Its appropriate selection could be used to control density, grain/crystallite size, and porosity of powder metallurgy parts which may improve mechanical properties. The SPS temperature has been fixed on some trial-and-error basis because of no available literature resource for this alloy. So , the conventional sintering temperature rule was first followed for the samples: sintering temperature was two-thirds of its melting temperature.

From the phase diagram mentioned in figure 3.1,

Melting temperature of Mg: 650^{o}C.
Melting temperature of Zn: 419^{o}C
Melting temperature of Er: 1522^{o}C
Melting temperature of Ce: 795^{o}C

So, the sintering temperature was selected around 2/3 of the melting temperature of Zinc (as it has the lowest sintering temperature), which was 300 ^{o}C using 3kN pressure. When the samples were sintered at 320^{o}C, their strength was too low to hold. Again during sintering, the pieces at 450^{o}C (2/3 of melting temperature of Magnesium), die spillage occurred. So, the temperature was tried to be fixed within a very narrow range from 400^{o}C to 420^{o}C with a constant 2.5kN vertical pressure.

After the die preparation, the samples were sintered at three different temperatures, such as 400^{o}C,410^{o}C, and 420^{o}C, and the following programs were used.

4.1.4 Program Selection in SPS:

Programs were selected by trial and error. Before sintering this alloy, some other alloy samples, including Cu-Zn alloy, Mg-Mn-Zn alloy, Cu-Mg alloy, Al-Mg alloy, Mg-Zn alloy, were sintered to understand how an alloy behaves during this SPS process. In general, shorter sintering times or higher rates suppress grain growth. So, one common trend had been followed for all samples that the heating rate was high in the lower temperature range. The following programs were selected to sinter samples at three different temperatures depending on the previous trial programs.

Table 4.1- Program for 400^{o}C sintering temperature.

Steps	Temperature range (^{o}C)	Time (min)	Rate (^{o}C/min)
1	0-130	5	26
2	130-300	3	56.67
3	300-350	1	50
4	350-375	1	25
5	375-388	1	13
6	388-394	1	6
7	394-397	1	3
8	397-400	3	1

Table 4. 2- Program for 410^{o}C sintering temperature.

Steps	Temperature range (^{o}C)	Time (min)	Rate (^{o}C/min)
1	0-130	5	26
2	130-310	3	60

3	310-360	1	50
4	360-385	1	25
5	385-397	1	12
6	397-404	1	7
7	404-407	1	3
8	407-410	3	1

Table 4. 3- Program for 420^{o}C sintering temperature.

Steps	Temperature range (^{o}C)	Time (min)	Rate (^{o}C/min)
1	0-130	5	26
2	130-310	3	60
3	310-370	1	60
4	370-395	1	25
5	395-410	1	15
6	410-415	1	5
7	415-417	1	2
8	417-420	3	1

4.1.5 Sintering process:

1. The powder samples were sintered into pallets in the spark plasma sintering furnace (Dr Sinter, SPS-515S, SPS Syntax Inc., Kawasaki, Japan). At first, the water-cooling valve and vacuum chamber were opened just after starting the machine.

2. The P.set button was kept to 000 positions to avoid damage to the tools or the machine.

3. The lower ram (lower electrode) was put down to insert the graphite die inside the chamber.

4. The prepared die was mounted on top of the lower ram with graphite spacer. Then another graphite spacer was put on top of the upper punch to make it symmetric.

5. Then, the lower ram was lifted until the spacer was contacted by the upper ram (upper electrode).

6. The thermocouple was inserted into the set hole properly.

7. The whole chamber was closed, and the Pirani vacuum gauge was opened to make the chamber air-free. Vacuum pump-1 was set as on, and vacuum pump-2 was set as open. The lower chamber was pushed tightly for two seconds after the vac. The valve was opened.

8. After getting the appropriate vacuum level, the pressure gauge reading was set as 2.5kN.

9. Then, previously determined patterns were set in the PID controller keeping the Z-axis displacement zero.

10. SPS time was set longer than the planned pattern time, and then the sintering was started.

11. After finishing the sintering following step-by-step changes of time, temperature, and pressure, the SPS machine was automatically stopped.

12. Then, the thermal controller was reset, and the P.set value was made zero before opening the chamber.

13. SPS pressure was lowered by stop buttons.

14. After completely cooling the sintering chamber (below 100^{o}C), the vacuum chamber was opened, and the chamber was returned to atmospheric pressure.

15. The sintering chamber was opened, and the thermocouple was removed carefully. Then the lower ram was put down, and the sample was drawn.

16. After removing the sample, the chamber was closed, and the power of the machine was turned off, and the water-cooling valve was closed before further SPS operation.

17. In this way total twelve (12) samples were sintered separately.

(a)

(b)

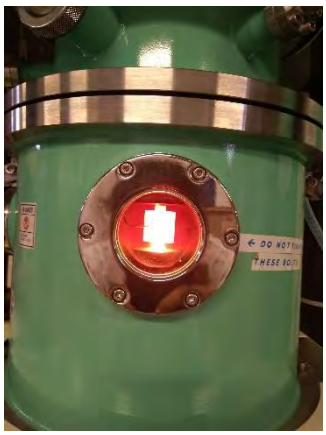

(c)

(d)

Figure 4.3: (a) Spark plasma sintering machine, (b) Sample inside the sintering chamber before sintering (c) Sample inside the sintering chamber during sintering (d) Final product after sintering.

4.1.6 Heat Treatment:

After sintering all the samples, each was polished on the wet polishing rotating disk at 150rpm. In the next phase, half of the samples were heat-treated in a tube furnace under the argon gas environment following a particular heat treatment cycle.

(a) Tube furnace

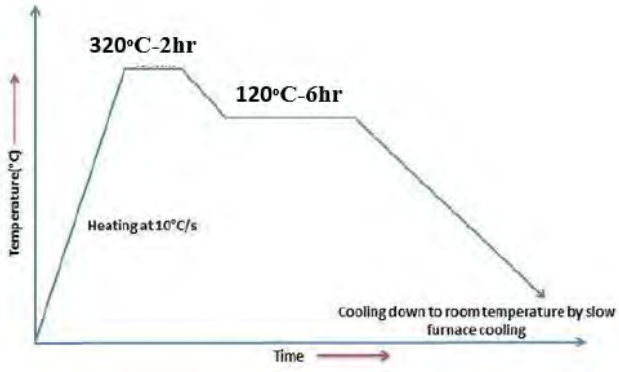

(b) Heat treatment cycle

Figure 4.4: Heat treatment (a) Tube furnace (b) Heat treatment cycle

4.2 Optical Microscopic Imaging

Optical micrographs of magnesium alloy samples were taken by using an optical microscope. It is a potent tool for understanding the grain size, shape, the morphology of samples. Prepared samples were taken under an optical microscope to see grain size, shape, and distribution. Before watching the surface of the samples, they were appropriately polished by using different grades of tungsten carbide paper for several minutes. Finally, 1-micrometre diamond suspension and 0.6-micrometre silicon suspension and polishing cloth were used for wet polishing. After that, the samples were immersed into the etching agent, a mixture of 10ml acetic acid and 150ml ethanol solution. Each sample was dipped in the acetic acid solution for 3 minutes, washed with distilled water, and then observed under an optical microscope to see grain and grain boundaries.

4.3 Scanning Electron Microscopy

A field emission scanning electron microscope (JEOL JSM-7600F) was used to scan electron microscopy to reveal different phases. Each sample was mounted in Bakelite mould, with 10mm and 30mm inner and outer diameter, respectively. Microstructures were observed both in secondary mode and backscattering modes.

This test was carried out for six samples of three different temperatures and heat-treated and untreated conditions. Along with the SEM, the system enables obtaininging chemical information from a specimen by using various techniques, including an X-ray energy-dispersive spectrometer (EDS). The EDS micro-analyzer in an SEM uses a primary electron beam to excite the emission of characteristic X-rays from the sample atoms. Since the electron beam can be readily focused on a microscopic area on a sample, the EDS micro-analyzer can examine chemical compositions in a tiny space.

4.4 Hardness Test

The Vickers hardness test measured the microhardness of the samples. The specimens were moulded in bakelite before hardness testing. The primary load (2 kg) was then applied for 10 seconds and removed. The resulting Vickers hardness number (as seen as a digital output) was inversely related to the additional depth to which the indenter was forced by the significant load beyond the depth of the zero-load condition.

4.5 Corrosion Test

The selection of corrosive media was an essential part of corrosion testing. The representative service environments are serum/plasma and interstitial fluid, considering the central application potentials of Mg (vascular stent material and bone fixation material); the usual service environments are serum/plasma and interstitial fluid.

The weight loss method is the most common method for the study of metal corrosion, and considered by some to be the benchmark standard. This method was used for corrosion rate determination of magnesium samples. It is the direct method for the one-point corrosion rate calculation, and the environment is easily controllable. Nonetheless, weight loss tests can also provide an exposed surface from which assessment of corrosion morphology (i.e., general,

localised, etc.) can be ascertained. "Simulated body fluids" is a broad term referring to the media containing all the major inorganic ions (without bio-relevant organic compounds except for glucose) that are present in human serum and interstitial fluid. Here, a simulated body fluid called Hanks' Balanced Salt solution (HBSS modified) with calcium, magnesium, and without phenol red and suitable for cell culture was used as corrosion media. Here milligram per decimeter square per day (MDD) method has been used. Here, the material loss was calculated in milligram, and the area's faiwas calculated in decimeter square.

MDD=$\frac{mg}{\frac{\text{dm2}}{day}}$

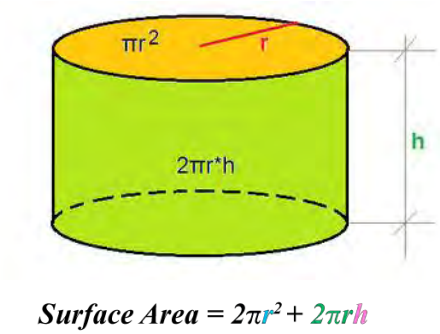

Surface Area = $2\pi r^2 + 2\pi rh$

Figure 4.5: Surface area calculation of the samples for corrosion test

In weight loss testing, the mass and surface of the Mg alloy specimens were measured before and after exposure to a corrosive environment for 61 days. The samples were tested under the static conditions in the lab, and changes of dimension and weight were recorded, maintaining 15 days fixed interval between the previous and the following data. From all the recorded information, MDD was calculated.

4.6 X-ray radiography

X-ray fluoroscopic image is vital to identify whether the samples are usable as implant material inside the body. It can be visible during the diagnostic implant imaging process if it shows enough contrast with the blood, tissue, or other body fluid inside the body.

Advanced imaging is often needed for the visualisation and evaluation of implanted devices. Mg implants are usually easier to visualize than polymeric visualisefor being metallic alloy. However, at late time points, the radiopacity of the Mg-based implant is low due to biodegradation, and the device's appearance may be like the surrounding tissue. High-resolution radiographs can also be used to identify and document stent or implant fracture or other abnormalities. Ex vivo imaging with x-ray can give two-dimensional (2-D) information that assists with localisation of the implant and, in some cases, quantification of the amount of residual implant or other parameters; this information is useful both alone and in conjunction with the medical evaluation.

Radiographic testing of two samples was performed in the non-destructive testing division of the Bangladesh Atomic Energy Commission. X-ray fluoroscopic images were taken using soft x-ray at 400 keV peak tube voltage for the magnesium alloy samples.

Chapter 5
Results and Discussions

In this chapter, the study results are presented and discussed concerning the aim of the study, which was to determine the influence of different sintering temperatures on various properties of the alloy. These aspects were described in the previous chapter that presented the methodology used in the study.

5.1 Optical Microscopic Imaging:

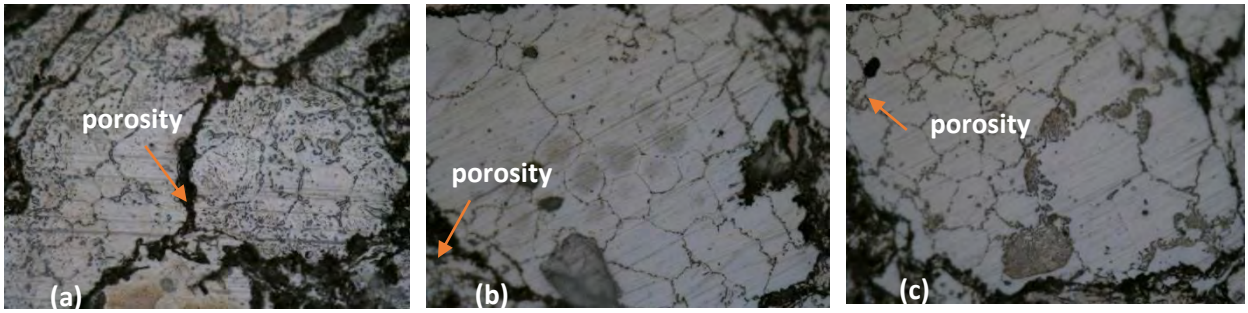

Figure 5.1: Optical micrograph of heat-treated sintered at a.400°C b.410°C c.420°C samples.

Figure 5.1 shows the microstructure of the heat-treated SPSed samples prepared at three different temperatures. The powder particles are still recognisable along with their primarily cellular microstructure. The clear visible grain boundary is observed in etched conditions. Coarser precipitates decorate the edges of the former powder particles. Maximum porosities are kept for the samples sintered at low temperatures. Inefficient sintering parameters such as pressure, temperature, and time may also be responsible for the lack of metal-metal contact required for successful sintering. Thus the relatively higher residual porosity levels observed. Molnarova et al. mentioned high atomic number particle in his Nanocrystalline Al7075 + 1 wt % Zr alloy prepared using mechanical milling and spark plasma sintering [134]. The initially continuous intercellular segregations were rearranged into semi-continuous precipitates formed by higher atomic weight alloying elements. Furthermore, a few hundred nm particles were found in the grain interiors. Another possible reason for the relatively high amount of porosity may be oxidation. Powders milled for 8 h are characterised by a smaller average particle and thus a larger surface area, which renders them more susceptible to oxidation during sintering. The oxide layer formed at the surface of the particles may then act as a diffusion barrier that prevents neck formation between neighbouring particles. Cˇapek and Vojteˇch showed that an increase in purity of the sintering atmosphere enhances the densification of porous Mg, which they have attributed to the reduction in the level of surface oxidation [134].

5.2 SEM and EDS analysis:

In the SPS consolidated Mg alloy, the grain size distribution with coarse grains was around 80µm for the samples sintered at 400°C, and refined grains with an average grain size was 13.33µm for the samples sintered at 420°C. The SEM micrograph comparison is shown below:

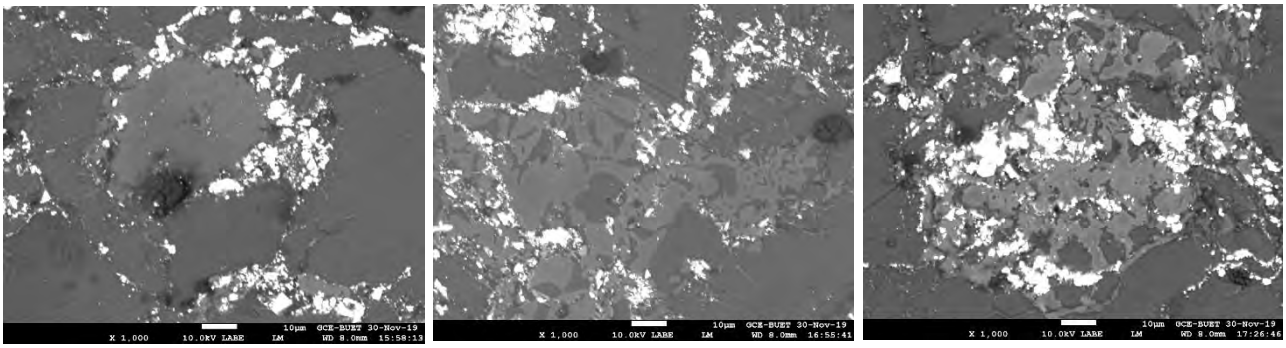

Figure 5.2: SEM micrograph of untreated samples sintered at a. 400°C b.410°C c.420°C.

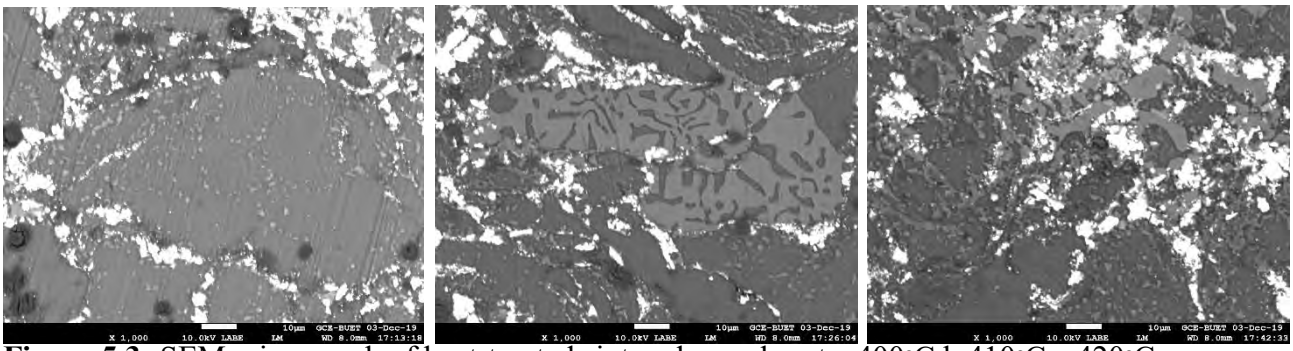

Figure 5.3: SEM micrograph of heat-treated sintered samples at a.400°C b.410°C c.420°C.

The SEM and EDS investigation revealed that sintering parameters had a tremendous effect on the size and distribution of different second-phase particles. Figure 5.2 and Figure 5.3 present SEM micrographs of the microstructure of the sintered Mg powder. In all the samples, a residual porosity located on the borders of the particles was revealed. The SEM result was satisfactory, considering it as a biomedical magnesium alloy. More acceptable grain size means better ductility of the alloy. But the number and size of pores decrease with increasing sintering temperature and time. Visible clear boundaries between the particles suggest further oxides on their surface. Despite the nature of the SPS process, these oxides were not wholly removed from the surface of the powder particles, which is associated most likely with the low sintering temperature and hence with the low pulse voltage, resulting in the hindered formation of micro-electrical discharges between the compacted powder particles. Both the sintering temperature and compaction pressure impact the rate of oxide removal. The higher the values of these parameters, the faster the phenomenon of crushing, followed by their evaporation. It was observed that the Mg particles underwent plastic deformation under the effect of the compaction pressure, the more when the sintering takes place at a higher temperature. It was declared in the research of Garbiec et al., with the increase of time and temperature, the size of the porosity decreased. However, the oxide boundary of the grains did not wholly remove despite the application of temperature, time, and pressure [135]. The elemental distribution showed an increased Er in these fine bright phases, whereas Zn and Ce were more

homogeneously in the matrix. Nevertheless, a small number of particles containing both Mg and Zn were present. Sintering at the temperature of 420°C resulted in a pronounced dissolution of the Mg-Er particles, as shown in Figure. 5.3 (c) in line with the data obtained from the EDS analysis. The content of both Er and Ce increased along these boundaries, leaving surrounding zones depleted of precipitates. With the increase of the SPS temperature, the size of the grains decreased. For the untreated samples grain size decreased from 80µm to 13.33µm and for treated samples 83µm to 17µm. Gabriel et al. also found that the grain size is about 17 to 66 for pure Magnesium powder [133]. It may be due to the consolidation pressure of the raw material. Dissolution of the grains during the heat treatment resulted in the formation of the more prominent grain of the samples i.e. for samples sintered at 420° C, the grain size varied from 13.33µm to 17 µm for untreated and treated sample

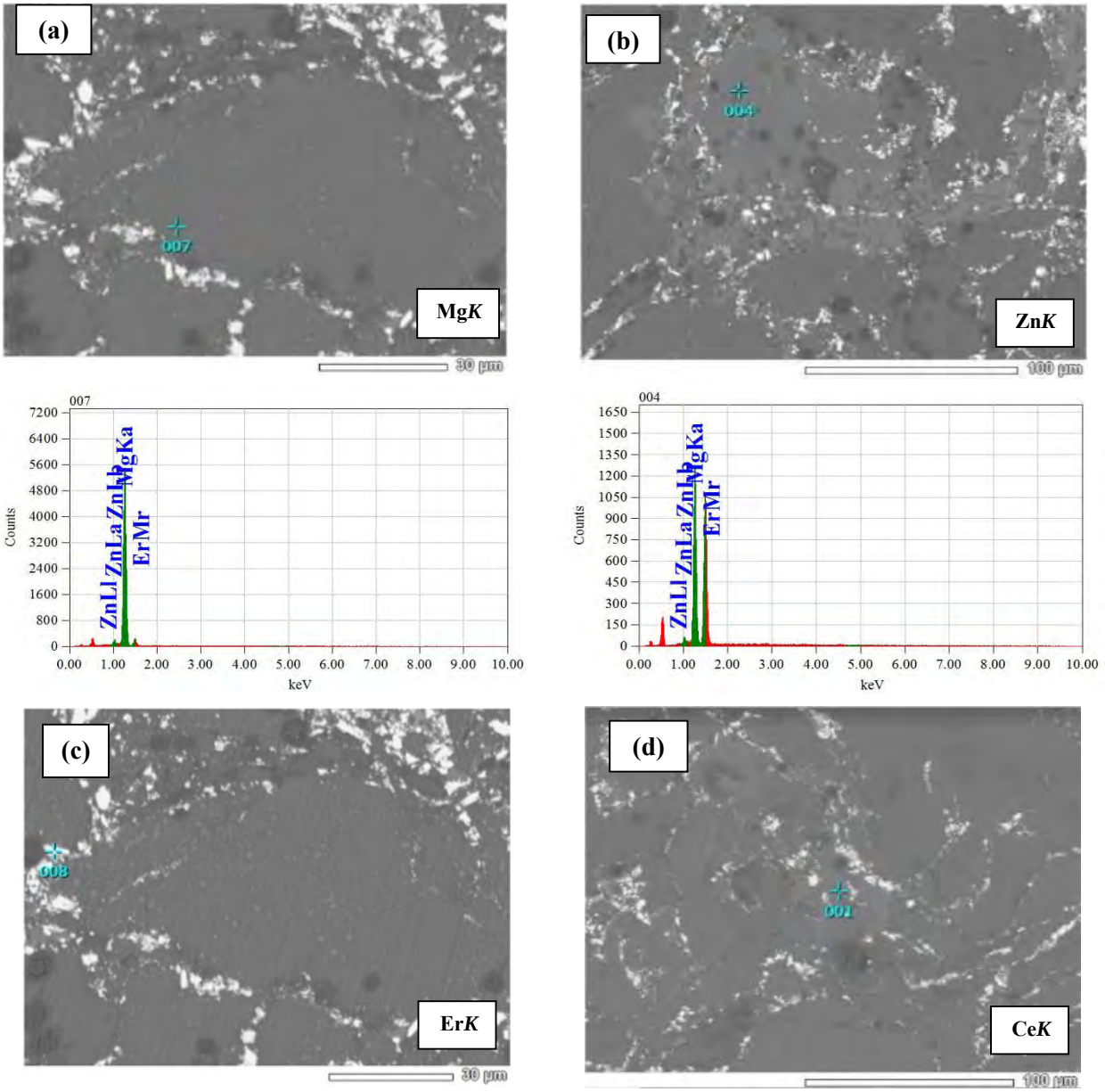

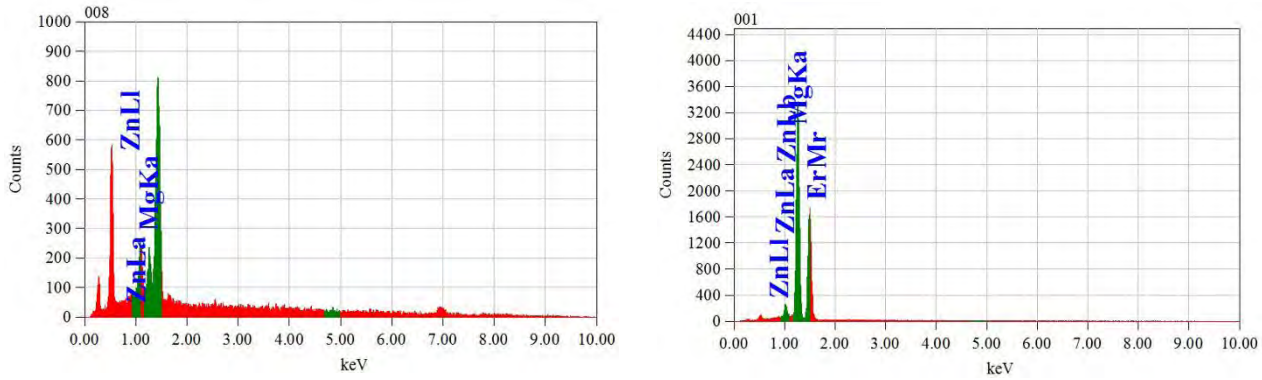

Figure 5.4: EDS analysis of heat-treated samples (a),(b),(c),(d) sintered at 400°C.

Table 5. 1- Elemental distribution of the samples sintered at 400°C.

Point	Element	Mass %
(a)007	Mg	96.76
(b)004	Zn	7.81
(c) 008	Er	95.75
(d) 001	Ce	3.13

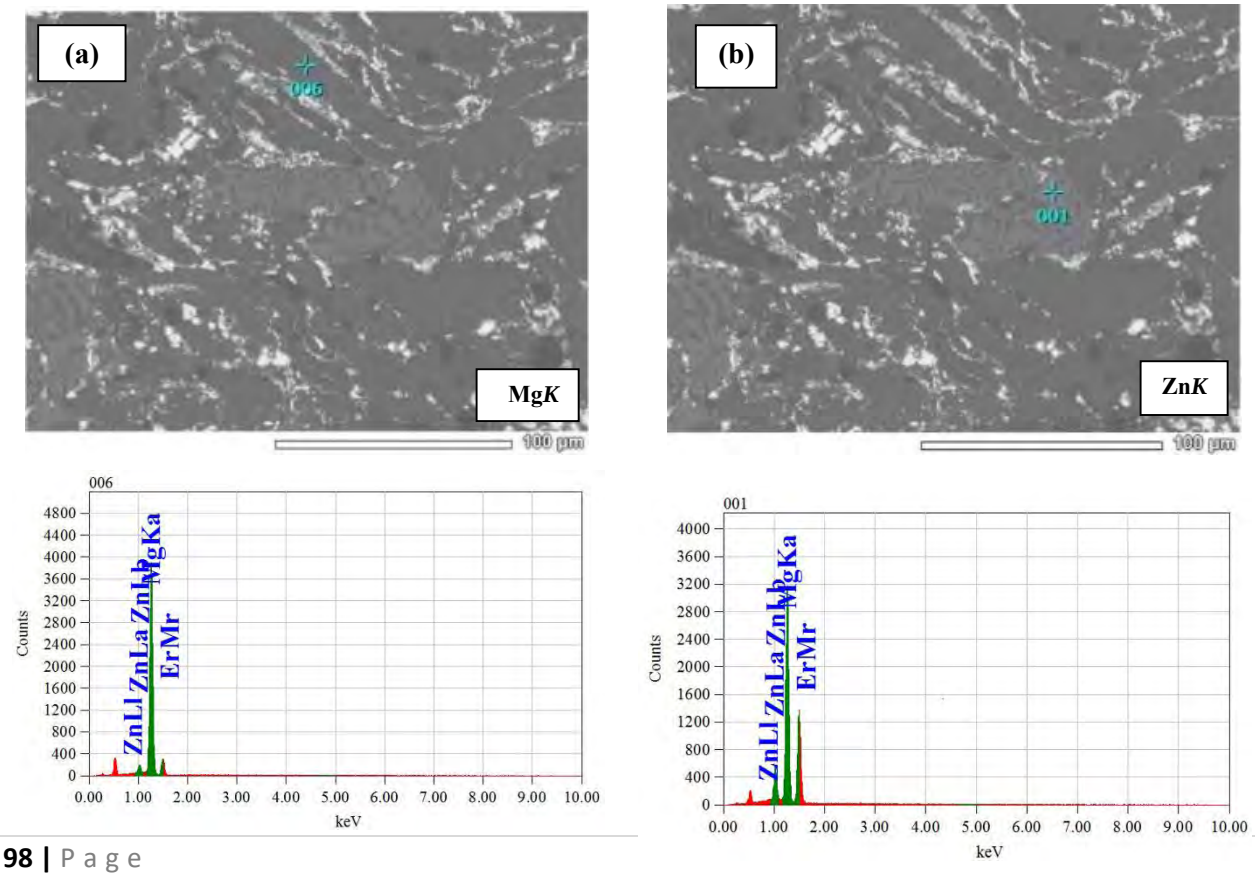

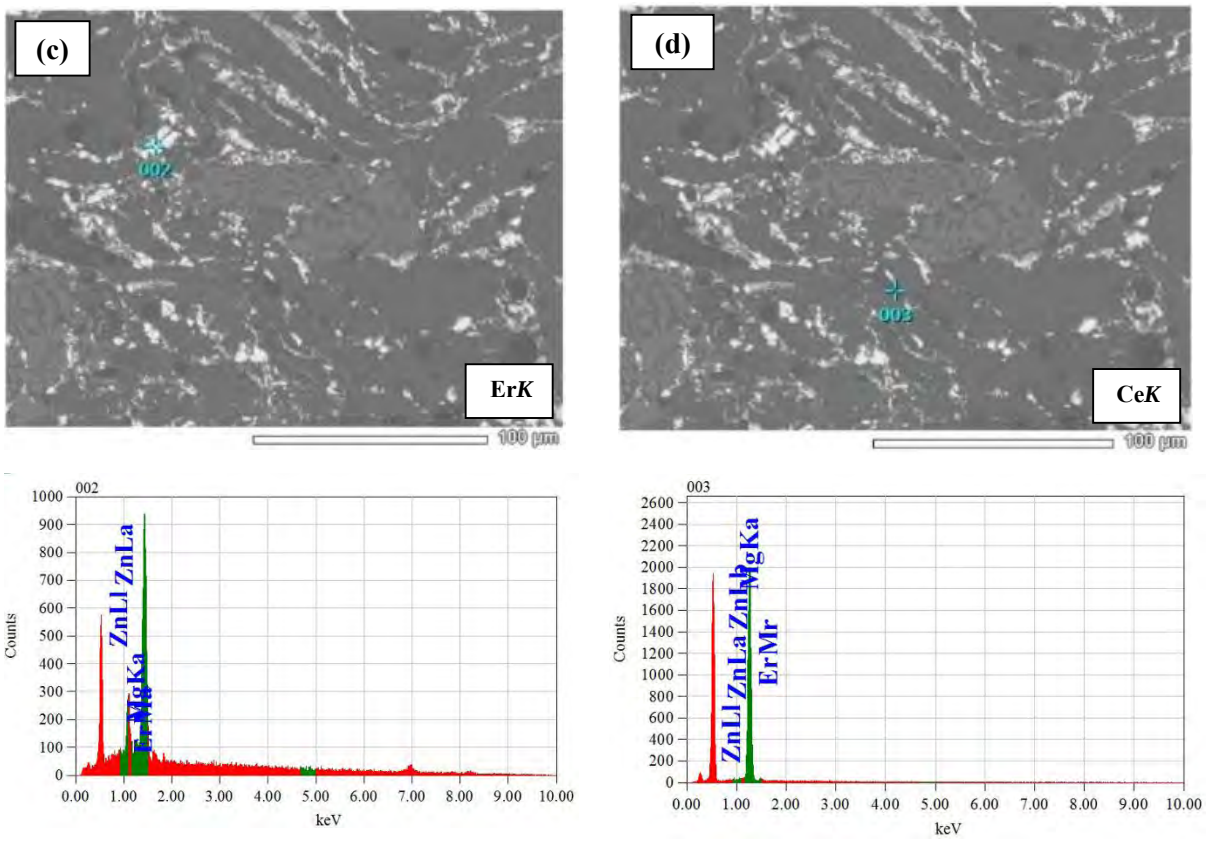

Figure 5.5: EDS analysis of heat-treated samples (a),(b),(c),(d) sintered at 410°C.

Table 5. 2- Elemental distribution of the samples sintered at 410°C.

Point	Element 1	Mass %
(a) 006	Mg	94.34
(b) 001	Zn	17.61
(c) 002	Er	98.71
(d) 003	Ce	1.20

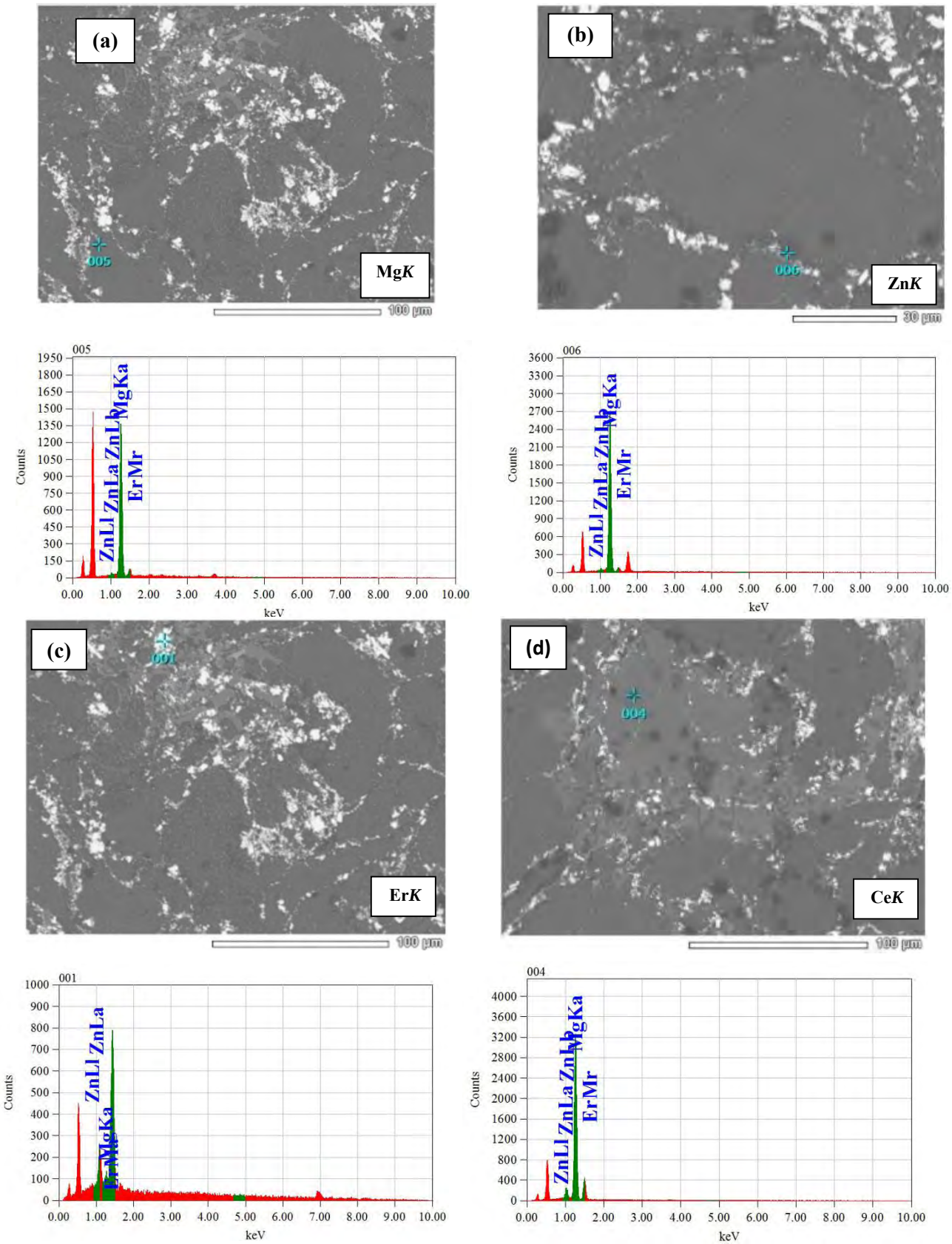

Figure 5.6: EDS analysis of heat-treated samples (a),(b),(c),(d) sintered at 420°C.

Table 5. 3- Elemental distribution of the samples sintered at 420°C.

Point	Element 7	Mass %
(a) 005	Mg	98.27
(b) 006	Zn	3.58
(c) 001	Er	97.87
(d) 004	Ce	3.23

The alloy's EDS analysis (elemental distribution) is presented in figures 5.4, 5.5, and 5.6, respectively. The EDS spectra and atomic percentages of elements listed here show that Er is distributed in the bright phase. The comparatively darker cluster could be the CeZn intermetallic compound of the Ce-Zn system. Still, the content of Zn and Ce in the precipitate is too low (Table 5.2-point 3), which indicates that the observed phase could be other phases from the Mg-Zn-Ce system. In contrast, based on the elemental distribution, Zn is more likely concentrated in the smaller precipitates. However, it is impossible to determine the actual composition of the small precipitates because of the inherently limited resolution of the EDS analysis. Without the heat treatment, the presence of magnesium and oxygen is obtained in the research of Kajánek et al. where SEM and EDS testing were used to analyse the topography and composition of a test material which explained that oxygen entered in the synthesis process of magnesium alloy from chemical sources [136].

5.3 Hardness Data

Spark plasma sintering (SPS) is a better technique due to its low energy consumption and short sintering time. SPS utilises a pulsed direct electrical current to perform high-speed consolidation of powders. Rapid high heating and cooling rates that characterise the SPS process allow maintaining and improving the inherent properties of powders in their fully dense products. Again, density has a significant impact on hardness. From Table 5.4, it can be observed that average hardness is highest for the samples prepared at 420°C.

Table 5. 4- Hardness of the samples sintered at 400°C, 410°C, and 420°C.

Temp	Hardness (Hv)	Avg Hardness (Hv)
400 °C	92.4	93.87
	95.2	
	94.0	
410 °C	101.8	102.8

	102.1	
	104.5	
420 °C	111.7	106.9
	108.0	
	107.0	

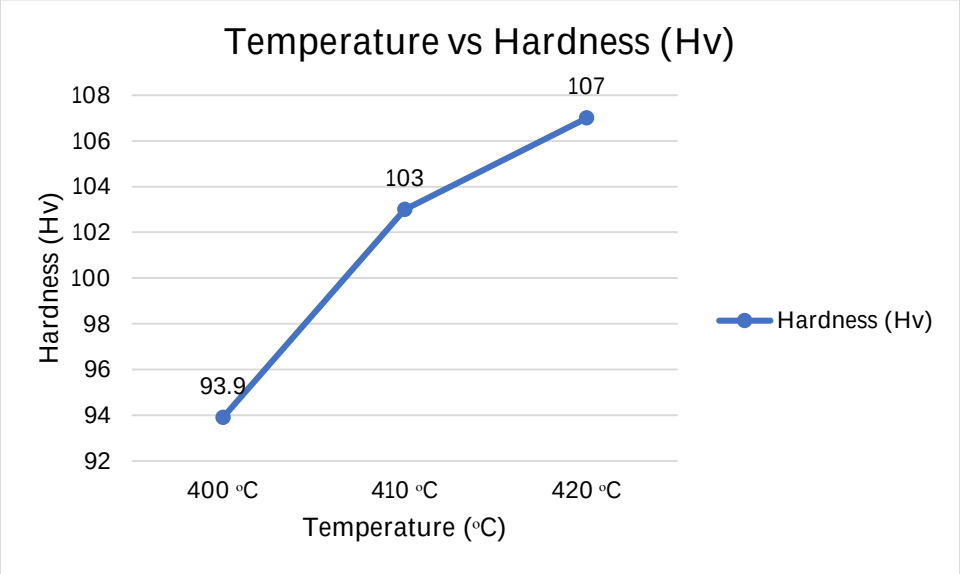

Figure 5.7: Hardness of the samples sintered at 400°C, 410°C and 420°C

Sintering temperature has a significant effect on the hardness of the sintered alloy. From figure 5.7, it can be seen that the hardness increases with the temperature increase. The higher densification part was produced at higher spark plasma sintering temperature conducted at 420°C compared with 400°C and 410°C. According to the Hall–Petch relationship, the hardness increases with the decrease of the grain size. The hardness of the SPSed alloy was predicted using Hall–Petch relationship suggested by Razavi et al. for Mg alloys [137].

5.4 Corrosion test

During this test, data was collected in the interval period, and weight loss was calculated using the MDD formula. And with this, weight loss data were plotted concerning time.

Figure 5.8: Samples in Day 1.

Table 5. 5- Weight and Area calculation of the samples in Day-01

Temp. (Cel.)	Sample wt. (mg)	Dia(dm)	Radius(dm)	Thickness (dm)	Area(dm^2)	Avg Area (dm^2)
400	913	0.1027	0.05135	0.0530	0.033668	0.033651
		0.1026	0.05130	0.0528	0.033554	
		0.1025	0.05125	0.0535	0.033731	
410	1008	0.1019	0.05095	0.0561	0.034270	0.034181
		0.1023	0.05115	0.0560	0.034436	
		0.1018	0.05090	0.0549	0.033836	
420	989	0.1013	0.05065	0.0567	0.034164	0.033998
		0.1012	0.05060	0.0558	0.033828	
		0.1022	0.05110	0.0548	0.034001	

Data was recorded on the very first day before the immersion of the samples into the HBSS. After 15 days, the samples were collected from the HBSS solution, and changes in area and weight were recorded.

Figure 5.9: Samples in Day 16.

Table 5. 6- Weight and Area calculation of the samples in Day-16

Temp. (Cel.)	Sample wt. (mg)	Dia(dm)	Radius(dm)	Thickness (dm)	Area(dm^2)	Avg Area(dm^2)
400	857	0.0925	0.04625	0.0350	0.023611	0.023231
		0.0918	0.04590	0.0332	0.022812	
		0.0923	0.04615	0.0341	0.023270	
410	996	0.0917	0.04585	0.0340	0.023004	0.022773
		0.0913	0.04565	0.0320	0.022272	
		0.0918	0.04590	0.0340	0.023043	
420	960	0.0902	0.04510	0.0331	0.022160	0.022249
		0.0905	0.04525	0.0332	0.022304	
		0.0903	0.04515	0.0334	0.022284	

Table 5. 7- Corrosion rate determination After 15 days.

Temp	Δwt. (mg)	Δarea (dm^2)	MDD
400	56	0.010420	358.2905
410	12	0.011408	70.1265
420	29	0.011748	165.1301

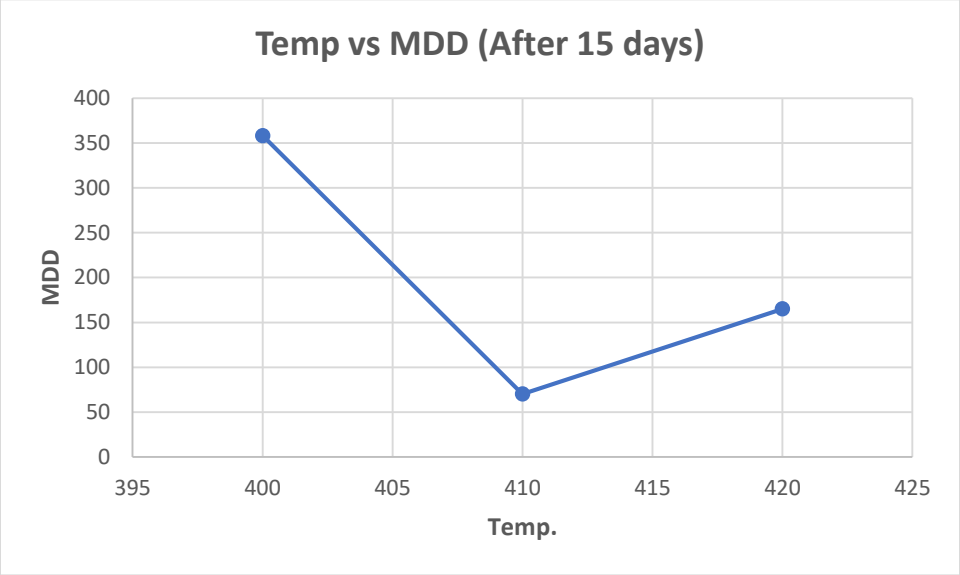

Figure 5.10: Corrosion rate (MDD) vs Temperature (°C) after 15 days.

According to Figure 5.10, the corrosion rate found minimum for the samples that were sintered at 410°C was 70.1265 MDD, and the maximum corrosion rate observed for the samples that sintered at 400° was 358.29 MDD. Initially, the corrosion rate was decreased for the sample SPSed in 410 °C but increased again at 420 °C. It may be due to the connecting porosity of the sample's surface. Knapek et al. also mentioned similar behaviour for Mg alloy [138].

Figure 5.11: Samples in Day 31.

Table 5. 8- Weight and Area calculation of the samples in Day-31

Temp. (Cel.)	Sample wt. (mg)	Dia(dm)	Radius(dm)	Thickness (dm)	Area(dm^2)	Avg Area(dm^2)
400	798	0.0700	0.0350	0.022	0.012535	0.012658
		0.0704	0.0352	0.025	0.013314	
		0.0701	0.0351	0.020	0.012123	
410	987	0.0708	0.0354	0.025	0.013434	0.013227
		0.0706	0.0353	0.024	0.013153	
		0.0704	0.0352	0.024	0.013093	
420	940	0.0730	0.0365	0.022	0.013416	0.013494
		0.0725	0.0363	0.023	0.013495	
		0.0720	0.0360	0.024	0.013572	

Table 5. 9- Corrosion rate determination After 30 days.

Temp	Δwt. (mg)	Δarea (dm^2)	MDD
400	59.2	0.010574	373.2576
410	9.5	0.009546	66.3444
420	19.7	0.008755	150.0110

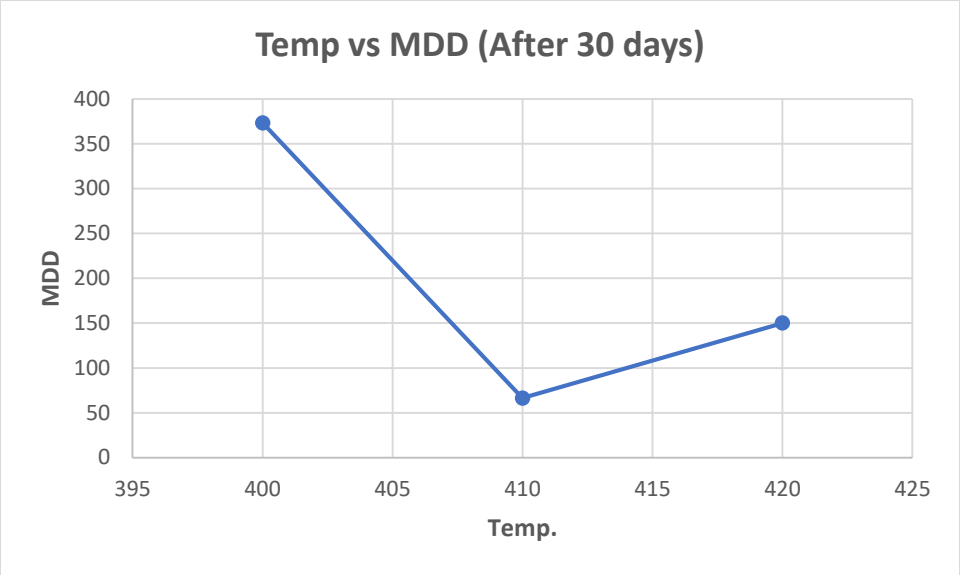

Figure 5.12: Corrosion rate (MDD) vs Temperature (°C) after 30 days.

Figure 5.12 showed a similar pattern of corrosion rate for the first 15 days. Here the maximum corrosion rate of 373.2576 MMD was obtained for the samples sintered at 400 °C, and the minimum corrosion rate of 66.34 MMD was observed for the samples sintered at 410 °C sintered. This corrosion pattern is similar to the previous graph, and it can also be explained according to the research of Knapek et al.[138]

Figure 5.13: Samples in Day 46.

Table 5. 10- Weight and Area calculation of the samples in Day-46

Temp. (Cel.)	Sample wt. (mg)	Dia(dm)	Radius(dm)	Thickness (dm)	Area(dm^2)	Avg Area(dm^2)
400	680	0.062	0.031	0.019	0.009739	0.010152
		0.065	0.033	0.020	0.010721	
		0.063	0.032	0.019	0.009995	
410	962	0.060	0.030	0.020	0.009425	0.011425
		0.070	0.035	0.021	0.012315	
		0.070	0.035	0.022	0.012535	
420	932	0.069	0.035	0.021	0.012031	0.012079
		0.068	0.034	0.023	0.012177	
		0.069	0.035	0.021	0.012031	

Table 5. 11- Corrosion rate determination After 45 days.

Temp	Δwt. (mg)	Δarea (dm^2)	MDD
400	118	0.002506	3139.084
410	24.5	0.001802	906.5052
420	8.3	0.001415	391.0765

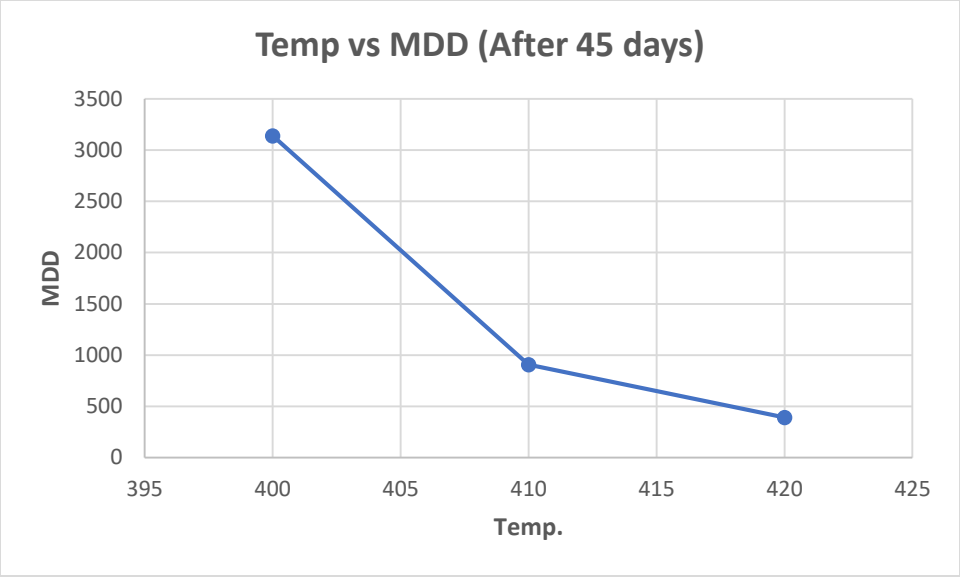

Figure 5.14: Corrosion rate (MDD) vs Temperature (°C) after 45 days.

In Figure 5.14, the corrosion rate pattern was different from the previous graphs in this period data. This curve showed that the higher the sintering temperature of the samples, the lower the degradation rate. The minimum corrosion rate was observed for the sintered sample of 420 °C, and the maximum was for 400°C. It is due to the higher densification of the SPSed samples. Guo et al. [139] have investigated the effect of sintering temperature on the corrosion resistance of Ti-24Nb-4Zr-7.9Snalloy and reported that alloys with lower density (sintered at low temperature) have lower corrosion resistance and vice versa. This lower corrosion resistance resulted from a more porous/less dense structure when sintered at low temperatures. Higher density means less interconnected porosity, so there will be fewer chances of electrolyte penetration into such interconnected pores, i.e., corrosion resistance will be increased. On the other hand, lower porosity samples will have less corrosion resistance due to open interconnected porosity. It is very well known that porosity in sintered samples will allow the corrosion medium stagnation in pores, which will lead to crevice corrosion. Bautista et al.[140] investigated the role of sintering temperature on density and the corrosion properties. They reported that an alloy with the highest sinter density (at higher sintering temperature) showed the best corrosion resistance.

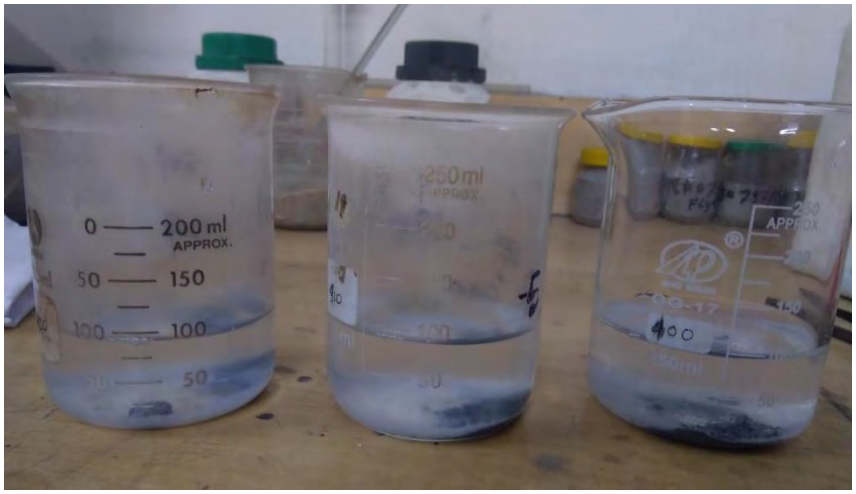

Figure 5.15: Samples in Day 61.

Table 5. 12- Weight and Area calculation of the samples in Day-61

Temp. (Cel.)	Sample wt. (mg)	Dia(dm)	Radius(dm)	Thickness (dm)	Area(dm^2)	Avg Area(dm^2)
400	550 Disintegrated	-	-	-	-	-
		-	-	-	-	
		-	-	-	-	
410	916	0.050	0.025	0.015	0.006283	0.006424
		0.050	0.025	0.014	0.006126	
		0.052	0.026	0.016	0.006861	
420	915	0.059	0.0295	0.019	0.00899	0.006635
		0.058	0.0290	0.019	0.008746	
		0.059	0.0295	0.018	0.008804	

Table 5. 13- Corrosion rate determination After 60 days.

Temp	Δwt. (mg)	Δarea (dm^2)	MDD
400	130	-	-
410	46	0.005001	613.1583
420	66.6	0.005444	203.2672

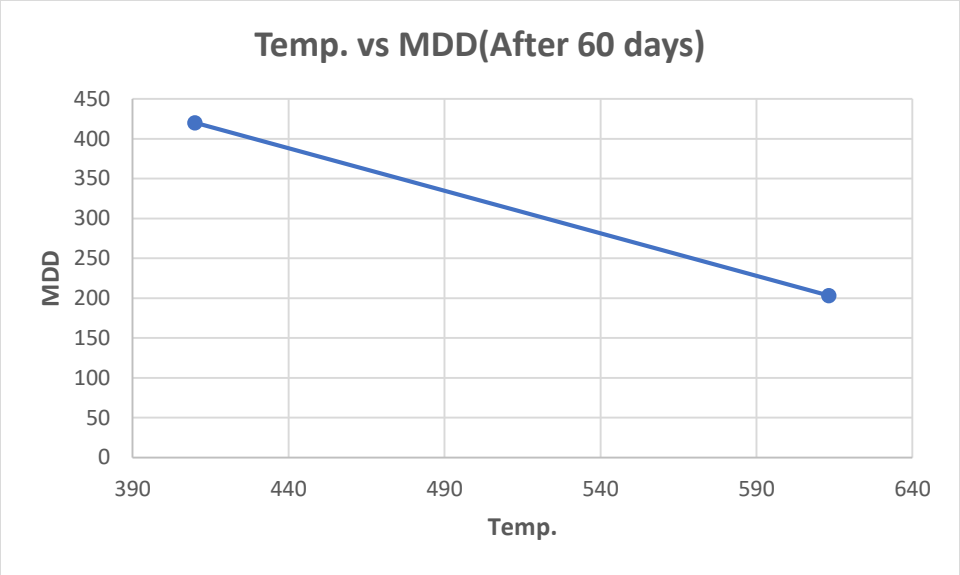

Figure 5.16: Corrosion rate (MDD) vs Temperature (°C) after 60 days.

In Figure 5.16, complete degradation was observed for the sintered sample of 400 °C, and the minimum corrosion rate was observed for the 420 °C. The sample SPSed in higher temperature possess higher densification means lower corrosion rate as mentioned by Bautista et al.[134].

Table 5. 14- Temperature and avg. corrosion rate after 60 days

Temperature	Avg. MDD
400	1290.2110
410	414.0335
420	227.3712

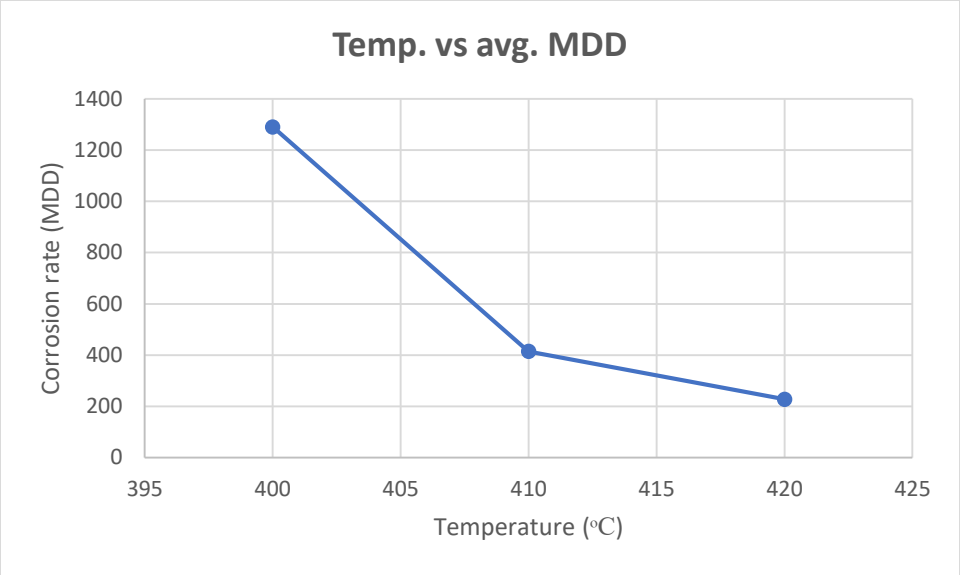

Figure 5.17: Relation between avg. corrosion rate (MDD) vs Temperature (°C) after 60 days

After averaging all the corrosion rate data of 60days, it is observed that the corrosion rate is the lowest for the samples sintered at higher temperature (420 °C), and the samples sintered at low temperature degrade at the highest rate. According to Bautista et al.[140], The total corrosion rate also decreases with maximum densification and minimum interconnected porosity.

Table 5. 15- Temperature and percentage of degradation after 60 days

Temp	Percentage of degradation in two months (60 days)
400	39.8%
410	9.1%
420	7.5%

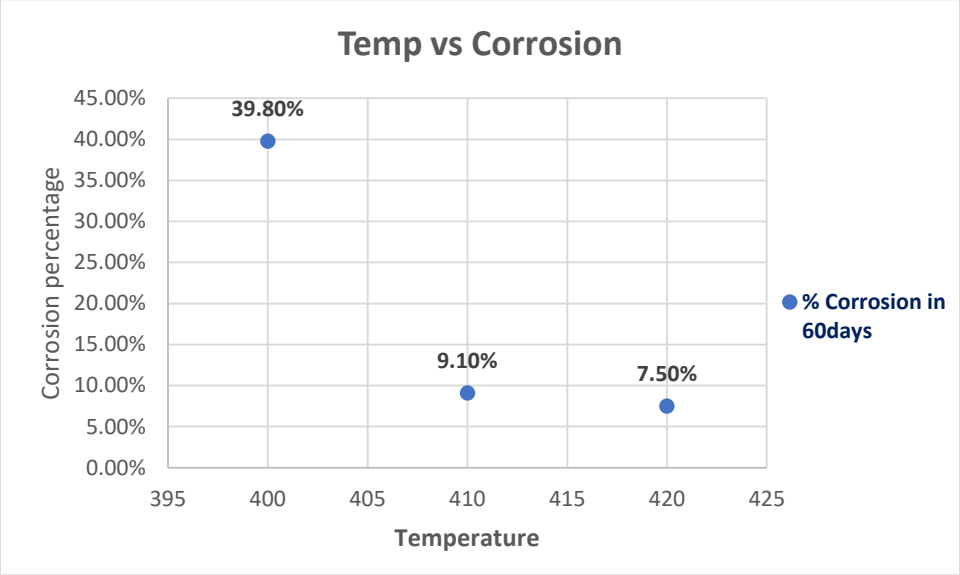

Figure 5.18: Relation between Temperature (°C) vs Degradation rate in 60 days

It also reveals from the above Figure 5.18 that the sample of 420 °C corrodes only 7.5%, but the sample of 400 °C corrodes 39%, which is comparatively higher for the use as biodegradable material. This lower corrosion resistance resulted from a more porous/less dense structure when sintered at low temperatures. Higher density means less interconnected porosity, so there will be fewer chances of electrolyte penetration into such interconnected pores, i.e., corrosion resistance will be increased. On the other hand, lower porosity samples will have less corrosion resistance due to open interconnected porosity. It is very well known that porosity in sintered samples will allow the corrosion medium stagnation in pores, which will lead to crevice corrosion. The alloy with 7.5% corrosion within two months can be used with some modifications for implant material where only two years of support is required. The corrosion rate was relatively high upon sintering at the lowest temperature of 400 °C, whereas a rather significant decrease in this quantity for the samples sintered at higher temperatures, 410 and 420 °C. Even though the improvement in the corrosion rate versus SPS temperature was not utterly gradual for all the data collection schedules, the immersion tests revealed superior corrosion performance upon sintering at higher temperatures. Knapek et al. also reviewed a similar phenomenon for SPSed Mg alloy for different temperatures. Higher corrosion resistance was observed for higher SPS temperatures, 500 and 550 °C. [138]

4.4 Radiography test:

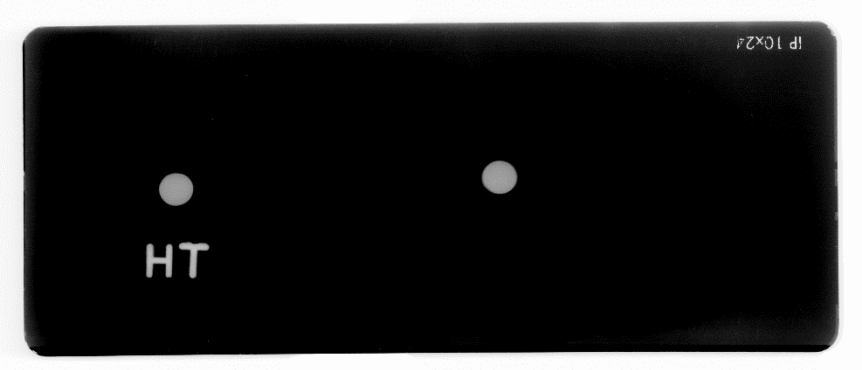

Figure 5.19: Radiopacity of the samples in heat-treated and untreated condition (Samples prepared at 420^{o} C)

Both samples (heat-treated and without treatment) showed almost similar visibility (Figure 5.19) under the radiographic testing. This image from the soft x-ray range reveals a very high radiopacity. Itassumed that the higher percentage of erbium is a reason for this increased visibility. Due to being cheaper than gold and platinum, erbium can be considered a valuable alternative. The xmudat x-ray attenuation coefficient can explain this phenomenon.

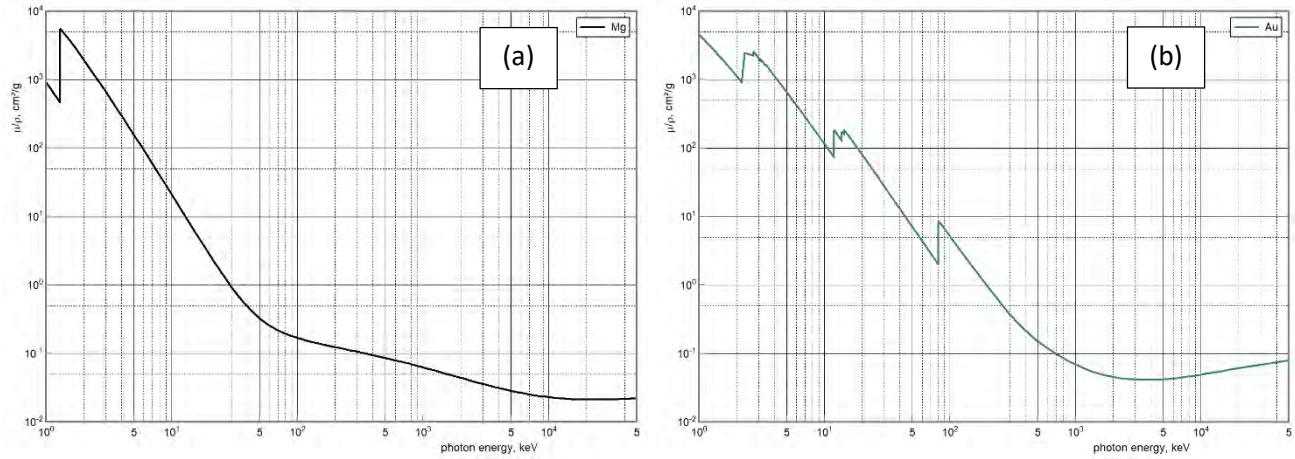

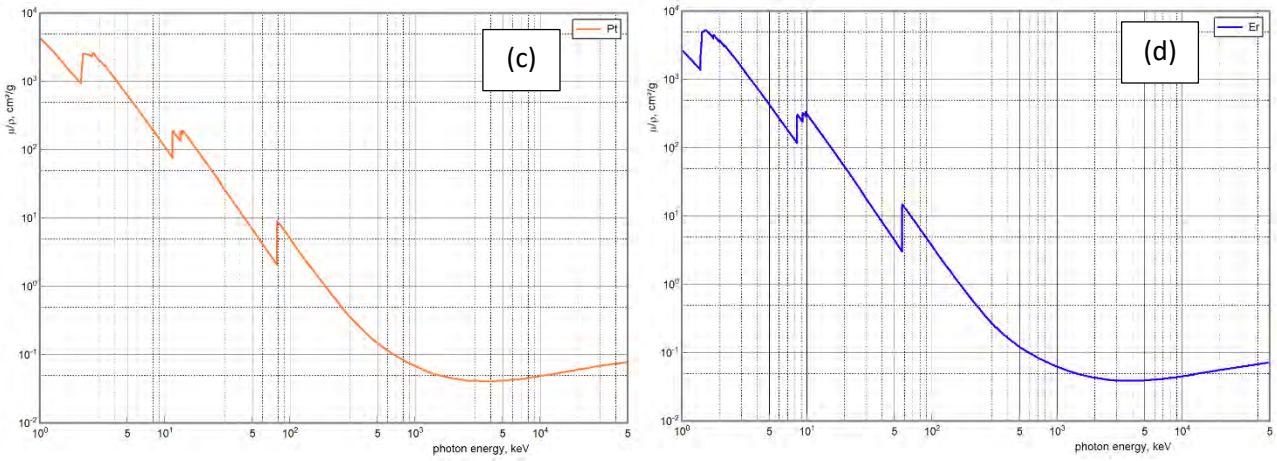

Figure 5.20: (a)Mg (b) Au (c) Pt (d) Er x-ray attenuation with respect to photon energy.

From the above graphs in Figure 5.20, it can be explained that in the soft x-ray range (5keV-10keV), there are some peaks only for Er, which provides the opacity of the samples both in a heat-treated and untreated condition. Ce can also show a height similar to (Figure 3.7 u) when used in a higher weight percentage. But it should be used at a minimum level because it has limited biocompatibility. In contrast, Er does not have such limitations. So, adequately modified samples can be an excellent alternative to Au or Pt marker in the implant. The dynamic nature of the linear attenuation coefficient is captured in the term "cumulative linear coefficient" (cumulative μ), which sums the products of multiplication of the X-ray imaging photon spectra (taken as a probable distribution) with the photon energy-dependent μ over the entire energy range of the photon spectra. The cumulative μ simulated for NiTi, 316 stainless steel, and platinum- enhancement of radiopacity by 7.5at% erbium (Er) was reported by Tofail et al. [72].

Chapter 6

Conclusion

The thesis work can be divided into two steps.

1. Synthesis and characterisation of Magnesium alloy (Mg, Er, Zn, Ce) by SPS sintering
2. Examine its viability as a body implant by identifying its hardness, radiopacity under x-ray, and accelerated corrosion behaviour in simulated body fluid.

Synthesis and Characterization of the Magnesium Alloy:

67% magnesium powder, 20% erbium powder, 2% zinc powder, and 1% cerium powder were mixed in the air-free environment. Then ball milled using alcohol media. After complete drying using a hot plate, the alloy pallet samples were sintered in the SPS machine at three different temperatures (400^{o}C, 410^{o}C, 420^{o}C) under constant pressure. Then the pallets were heat-treated in the tube furnace using an argon environment. After that, the following observations were recorded:

1. The microstructure of the sintered samples confirmed the presence of cellular grains. The presence of maximum porosities was found in the samples prepared at low SPS temperature.
2. SEM results declared the more acceptable grain size of the alloy. Maximum grain size (~80 nm) was observed for the sample prepared at 400^{o}C and minimum grain size (~13.33 nm) for the samples prepared at 420^{o}C.
3. EDS analysis confirmed Zn, Er, and Ce in the Mg matrix. Elemental distribution showed an increased concentration of Er in these fine bright phases along the grain boundary.

Viability analysis as a body implant material:

1. Accelerated corrosion test performed in modified Hank's solution reveals maximum corrosion rate (39%) for the sample of 400 ^{o}C and minimum corrosion rate (7.5%) for the sample of 400^{o}C. This lower corrosion resistance resulted from a more porous/less dense structure when sintered at low temperatures. The alloy with 7.5% corrosion within two months can be used with some modifications for implant material where only two years of support is required. Samples prepared at 420^{o} Celsius showed maximum hardness, and samples of 400^{o}C showed minimum hardness. The mean hardness value ranged from 93.87Hv to 106.9Hv for this unique alloy.
2. Samples showed higher radiopacity under soft medical x-ray range both in heat-treated and untreated conditions. Due to their greater radiopacity in the x-ray visibility test, Mg alloy with a higher weight percentage of Er is an excellent alternative to Au and Pt marker, confirmed by the mass attenuation coefficient in xmudat software.

Potential future work based on the limitation of the present study:

The following potential future work can be carried out in future:

1. Investigating the correlation between porosity, density and absorption.
2. Effect of rare earth element added to the mechanical and chemical properties of the newly designed alloy.
3. Phase analyses using x-ray diffraction.
4. Radiopacity comparison between conventional Mg alloy and newly designed Mg alloy

References

[1] N. Eliaz and N. Metoki, "Calcium phosphate bioceramics: A review of their history, structure, properties, coating technologies and biomedical applications," *Materials (Basel).*, vol. 10, no. 4, 2017.

[2] B. J. C. Luthringer, F. Feyerabend, and R. W. Römer, "Magnesium-Based Implants: A Mini-Review," *Magnes. Res.*, vol. 27, no. 4, pp. 142–154, 2014.

[3] M. Saini, "Implant biomaterials: A comprehensive review," *World J. Clin. Cases*, vol. 3, no. 1, p. 52, 2015.

[4] M. Li, M. J. Mondrinos, X. Chen, M. R. Gandhi, F. K. Ko, and P. I. Lelkes, "Elastin Blends for Tissue Engineering Scaffolds," *J. Biomed. Mater. Res. Part A*, vol. 79, no. 4, pp. 963–73, 2006.

[5] S. Agarwal, J. Curtin, B. Duffy, and S. Jaiswal, "Biodegradable magnesium alloys for orthopaedic applications: A review on corrosion, biocompatibility and surface modifications," *Mater. Sci. Eng. C*, vol. 68, pp. 948–963, 2016.

[6] P. K. Bowen *et al.*, "Biodegradable Metals for Cardiovascular Stents: From Clinical Concerns to Recent Zn-Alloys," *Adv. Healthc. Mater.*, vol. 5, no. 10, pp. 1121–1140, 2016.

[7] N. Eliaz, "Corrosion of metallic biomaterials: A review," *Materials (Basel).*, vol. 12, no. 3, 2019.

[8] D. J. Blackwood, "Biomaterials: Past Successes and Future Problems," *Corros. Rev.*, vol. 21, no. 2, pp. 97–124, 2003.

[9] H. Wang, N. Eliaz, Z. Xiang, H. P. Hsu, M. Spector, and L. W. Hobbs, "Early bone apposition in vivo on plasma-sprayed and electrochemically deposited hydroxyapatite coatings on titanium alloy," *Biomaterials*, vol. 27, no. 23, pp. 4192–4203, 2006.

[10] N. Eliaz, S. Shmueli, I. Shur, D. Benayahu, D. Aronov, and G. Rosenman, "The effect of surface treatment on the surface texture and contact angle of electrochemically deposited hydroxyapatite coating and on its interaction with bone-forming cells," *Acta Biomater.*, vol. 5, no. 8, pp. 3178–3191, 2009.

[11] O. Geuli, N. Metoki, T. Zada, M. Reches, N. Eliaz, and D. Mandler, "Synthesis, coating, and drug-release of hydroxyapatite nanoparticles loaded with antibiotics," *J. Mater. Chem. B*, vol. 5, no. 38, pp. 7819–7830, 2017.

[12] I. Lundstrgm, "ical Considerations of Tita," *Clin. Mater.*, vol. 9, pp. 115–134, 1992.

[13] T. Hanawa, "Reconstruction and Regeneration of Surface Oxide Film on Metallic Materials in Biological Environments," *Corros. Rev.*, vol. 21, no. 2–3, pp. 161–182, 2003.

[14] R. L. Williams, S. A. Brown, and K. Merritt, "Electrochemical studies on the influence of proteins on the corrosion of implant alloys," *Biomaterials*, vol. 9, no. 2, pp. 181–186, 1988.

[15] C. Sittig, G. Hähner, A. Marti, M. Textor, N. D. Spencer, and R. Hauert, "The implant material, Ti6Al7Nb: Surface microstructure, composition and properties," *J. Mater. Sci. Mater. Med.*, vol. 10, no. 4, pp. 191–198, 1999.

[16] I. Gurappa, "Characterization of different materials for corrosion resistance under simulated body fluid conditions," *Mater. Charact.*, vol. 49, no. 1, pp. 73–79, 2002.

[17] N. Eliaz, W. Kopelovitch, L. Burstein, E. Kobayashi, and T. Hanawa, "Electrochemical processes of nucleation and growth of calcium phosphate on titanium supported by real-time quartz crystal microbalance measurements and X-ray photoelectron spectroscopy analysis," *J. Biomed. Mater. Res. - Part A*, vol. 89, no. 1, pp. 270–280, 2009.

[18] N. Metoki, D. Mandler, and N. Eliaz, "Effect of decorating titanium with different self-assembled monolayers on the electrodeposition of calcium phosphate," *Cryst. Growth Des.*, vol. 16, no. 5, pp. 2756–2764, 2016.

[19] G. Manivasagam, U. Kamachi Mudali, B. Rajb, and R. Asokamani, "Corrosion and Microstructural Aspects of Titanium and its Alloys as Orthopaedic Devices," *Corros. Rev.*, vol. 21, no. 2–3, pp. 125–160, 2003.

[20] M. J. Muñoz-Portero, J. García-Antón, J. L. Guiñón, and R. Leiva-García, "Pourbaix diagrams for titanium in concentrated aqueous lithium bromide solutions at 25°C," *Corros. Sci.*, vol. 53, no. 4, pp. 1440–1450, 2011.

[21] S. B. Hong, N. Eliaz, E. M. Sachs, S. M. Allen, and R. M. Latanision, "Corrosion behavior of advanced titanium-based alloys made by three-dimensional printing (3DPTM) for biomedical applications," *Corros. Sci.*, vol. 43, no. 9, pp. 1781–1791, 2001.

[22] M. A. Khan, R. L. Williams, and D. F. Williams, "Corrosion and Wear of Titanium Alloys in the Biological Environment," vol. 17, no. 22, pp. 1–10, 2013.

[23] B. Grosgogeat, L. Reclaru, M. Lissac, and F. Dalard, "Measurement and evaluation of galvanic corrosion between titanium/Ti6Al4V implants and dental alloys by electrochemical techniques and auger spectrometry," *Biomaterials*, vol. 20, no. 10, pp. 933–941, 1999.

[24] N. Eliaz and T. M. Sridh, "Electrocrystallization of hydroxyapatite and its dependence on solution conditions," *Cryst. Growth Des.*, vol. 8, no. 11, pp. 3965–3977, 2008.

[25] G. D. Winter, "Tissue reaction to metallic wear and corrosion products in human patients," *J. Biomed. Mater. Res.*, vol. 8, no. 3, pp. 11–26, 1974.

[26] J. J. Elsner *et al.*, "Wear rate evaluation of a novel polycarbonate-urethane cushion form bearing for artificial hip joints," *Acta Biomater.*, vol. 6, no. 12, pp. 4698–4707, 2010.

[27] J. J. Elsner *et al.*, "Long-term evaluation of a compliant cushion form acetabular bearing for hip joint replacement: A 20 million cycles wear simulation," *J. Orthop. Res.*, vol. 29, no. 12, pp. 1859–1866, 2011.

[28] D. Lakstein, W. Kopelovitch, Z. Barkay, M. Bahaa, D. Hendel, and N. Eliaz, "Enhanced osseointegration of grit-blasted, NaOH-treated and electrochemically hydroxyapatite-

coated Ti-6Al-4V implants in rabbits," *Acta Biomater.*, vol. 5, no. 6, pp. 2258–2269, 2009.

[29] A. A. White and S. M. Best, *Properties and characterisation of bone repair materials*, no. 1. Woodhead Publishing Limited, 2009.

[30] C. Piconi, G. Maccauro, F. Muratori, and E. Brach Del Prever, "Alumina and zirconia ceramics in joint replacements.," *J. Appl. Biomater. Biomech.*, vol. 1, no. 1, pp. 19–32, 2003.

[31] M. Z. Ibrahim, A. A. D. Sarhan, F. Yusuf, and M. Hamdi, "Biomedical materials and techniques to improve the tribological, mechanical and biomedical properties of orthopedic implants – A review article," *J. Alloys Compd.*, vol. 714, pp. 636–667, 2017.

[32] Z. G. Huan, M. A. Leeflang, J. Zhou, L. E. Fratila-Apachitei, and J. Duszczyk, "In vitro degradation behavior and cytocompatibility of Mg-Zn-Zr alloys," *J. Mater. Sci. Mater. Med.*, vol. 21, no. 9, pp. 2623–2635, 2010.

[33] Y. Ding, C. Wen, P. Hodgson, and Y. Li, "Effects of alloying elements on the corrosion behavior and biocompatibility of biodegradable magnesium alloys: A review," *J. Mater. Chem. B*, vol. 2, no. 14, pp. 1912–1933, 2014.

[34] J. S. Ishay, Z. Barkay, N. Eliaz, M. Plotkin, S. Volynchik, and D. J. Bergman, "Gravity orientation in social wasp comb cells (Vespinae) and the possible role of embedded minerals," *Naturwissenschaften*, vol. 95, no. 4, pp. 333–342, 2008.

[35] A. Vinogradov, V. N. Serebryany, and S. V. Dobatkin, "Tailoring microstructure and properties of fine grained magnesium alloys by severe plastic deformation," *Adv. Eng. Mater.*, vol. 20, no. 4, 2018.

[36] P. Tian and X. Liu, "Surface modification of biodegradable magnesium and its alloys for biomedical applications," *Regen. Biomater.*, vol. 2, no. 2, pp. 135–151, 2015.

[37] S. Zhang *et al.*, "Research on an Mg-Zn alloy as a degradable biomaterial," *Acta Biomater.*, vol. 6, no. 2, pp. 626–640, 2010.

[38] G. Manivasagam and S. Suwas, "Biodegradable Mg and Mg based alloys for biomedical implants," *Mater. Sci. Technol. (United Kingdom)*, vol. 30, no. 5, pp. 515–520, 2014.

[39] Y. Ding, J. Lin, C. Wen, D. Zhang, and Y. Li, "Mechanical properties, in vitro corrosion and biocompatibility of newly developed biodegradable Mg-Zr-Sr-Ho alloys for biomedical applications," *Sci. Rep.*, vol. 6, no. August, pp. 1–10, 2016.

[40] P. Szymczyk, G. Ziółkowski, A. Junka, and E. Chlebus, "Application of Ti6Al7Nb alloy for the manufacture of biomechanical functional structures (BFS) for custom-made bone implants," *Materials (Basel).*, vol. 11, no. 6, pp. 1–16, 2018.

[41] M. S. Uddin, C. Hall, and P. Murphy, "Surface treatments for controlling corrosion rate of biodegradable Mg and Mg-based alloy implants," *Sci. Technol. Adv. Mater.*, vol. 16, no. 5, 2015.

[42] J. Pan, C. Karlén, and C. Ulfvin, "Electrochemical Study of Resistance to Localized Corrosion of Stainless Steels for Biomaterial Applications," *J. Electrochem. Soc.*, vol. 147,

no. 3, p. 1021, 2000.

[43] A. D. Pogrebnjak, S. N. Bratushka, V. M. Beresnev, and N. Levintant-Zayonts, “Shape memory effect and superelasticity of titanium nickelide alloys implanted with high ion doses,” *Russ. Chem. Rev.*, vol. 82, no. 12, pp. 1135–1159, 2013.

[44] J. M. Anderson, A. Rodriguez, and D. T. Chang, “Foreign body reaction to biomaterials,” *Semin. Immunol.*, vol. 20, no. 2, pp. 86–100, 2008.

[45] S. Virtanen, “Corrosion of biomedical implant materials,” *Corros. Rev.*, vol. 26, no. 2–3, pp. 147–172, 2008.

[46] M. Morita, T. Sasada, H. Hayashi, and Y. Tsukamoto, “The corrosion fatigue properties of surgical implants in a living body,” *J. Biomed. Mater. Res.*, vol. 22, no. 6, pp. 529–540, 1988.

[47] E. J. Sutow, D. W. Jones, and E. L. Milne, “In vitro Crevice Corrosion Behavior of Implant Materials,” *J. Dent. Res.*, vol. 64, no. 5, pp. 842–847, 1985.

[48] K. J. Bundy, M. A. Vogelbaum, and V. H. Desai, “The influence of static stress on the corrosion behavior of 316L stainless steel in Ringer’s solution,” *J. Biomed. Mater. Res.*, vol. 20, no. 4, pp. 493–505, 1986.

[49] M. Dilea, A. Mazare, D. Ionita, and I. Demetrescu, “Comparison between corrosion behaviour of implant alloys Ti6Al7Nb and Ti6Al4Zr in artificial saliva,” *Mater. Corros.*, vol. 64, no. 6, pp. 493–499, 2013.

[50] S. Cabeza, G. Garcés, P. Pérez, and P. Adeva, “Properties of WZ21 (%wt) alloy processed by a powder metallurgy route,” *J. Mech. Behav. Biomed. Mater.*, vol. 46, pp. 115–126, 2015.

[51] M. Cataldo-Hernández, M. Stewart, A. Bonakdarpour, M. Mohseni, and D. P. Wilkinson, “Degradation of ferrate species produced electrochemically for use in drinking water treatment applications,” *Can. J. Chem. Eng.*, vol. 96, no. 5, pp. 1045–1052, 2018.

[52] L. A. Drake *et al.*, “Potential invasion of microorganisms and pathogens via ‘interior hull fouling’: Biofilms inside ballast water tanks,” *Biol. Invasions*, vol. 7, no. 6, pp. 969–982, 2005.

[53] P. Zhang, W. P. Johnson, and R. Rowland, “Bacterial tracking using ferrographic separation,” *Environ. Sci. Technol.*, vol. 33, no. 14, pp. 2456–2460, 1999.

[54] S. A. Brown and K. Merritt, “Fretting corrosion in saline and serum,” *J. Biomed. Mater. Res.*, vol. 15, no. 4, pp. 479–488, 1981.

[55] B. G. Pound, “Corrosion behavior of metallic materials in biomedical applications. I. Ti and its alloys,” *Corros. Rev.*, vol. 32, no. 1–2, pp. 1–20, 2014.

[56] U. Kamachi Mudali1, B. Raj, T. M. Sridhar, and N. Eliaz, “Failures of Stainless Steel Orthopedic Devices - Causes and Remedies,” *Corros. Rev.*, vol. 21, no. 2, pp. 231–268, 2003.

[57] C. C. Shih, S. J. Lin, K. H. Chung, Y. L. Chen, and Y. Y. Su, "Increased corrosion resistance of stent materials by converting current surface film of polycrystalline oxide into amorphous oxide," *J. Biomed. Mater. Res.*, vol. 52, no. 2, pp. 323–332, 2000.

[58] B. G. Pound, "Corrosion behavior of metallic materials in biomedical applications. II. Stainless steels and Co-Cr alloys," *Corros. Rev.*, vol. 32, no. 1–2, pp. 21–41, 2014.

[59] T. Fusayama, T. Katayori, and S. Nomoto, "Corrosion of Gold and Amalgam Placed in Contact with Each other," *J. Dent. Res.*, vol. 42, no. 5, pp. 1183–1197, 1963.

[60] D. J. Rabkin, E. V. Lang, and D. P. Brophy, "Nitinol properties affecting uses in interventional radiology," *J. Vasc. Interv. Radiol.*, vol. 11, no. 3, pp. 343–350, 2000.

[61] A. Wadood, "Brief overview on nitinol as biomaterial," *Adv. Mater. Sci. Eng.*, vol. 2016, 2016.

[62] J. A. Hunter, G. H. Mills, and R. D. Sturrock, "Ferrography - A new method for isolation of particles from biological fluids," *J. Clin. Pathol.*, vol. 35, no. 6, pp. 689–690, 1982.

[63] A. N. Hughes, B. A. Jordan, and S. Orman, "The corrosion fatigue properties of surgical implant materials. Third progress report: May 1973," *Eng. Med.*, vol. 7, no. 3, pp. 135–141, 1978.

[64] M. Traisnel, D. le Maguer, H. F. Hildebrand, and A. Iost, "Corrosion of surgical implants," *Clin. Mater.*, vol. 5, no. 2–4, pp. 309–318, 1990.

[65] S. Tamilselvi and N. Rajendran, "Electrochemical studies on the stability and corrosion resistance of Ti-5Al-2Nb-1Ta alloy for biomedical applications," *Trends Biomater. Artif. Organs*, vol. 20, no. 1, pp. 49–52, 2006.

[66] H. Zitter, "Schadensfalle an chirurgischen Implantaten und ihre Ursachen," *Werkstoffe und Korrosion*, vol. 42, no. 9, pp. 455–466, 1991.

[67] J. C. De La Vega and U. O. Häfeli, "Utilization of nanoparticles as X-ray contrast agents for diagnostic imaging applications," *Contrast Media Mol. Imaging*, vol. 10, no. 2, pp. 81–95, 2015.

[68] "Properties of Materials Used in Orthopaedic," pp. 1–35, 2015.

[69] A. Johnson and T. Shiraishi, *Biocompatibility of precious metals for medical applications*. Woodhead Publishing Limited, 2014.

[70] K. Yang and Y. Ren, "Nickel-free austenitic stainless steels for medical applications," *Sci. Technol. Adv. Mater.*, vol. 11, no. 1, p. 014105, 2010.

[71] S. A. M. Tofail *et al.*, "X-ray visibility and metallurgical features of NiTi shape memory alloy with erbium," *Mater. Lett.*, vol. 137, pp. 450–454, 2014.

[72] A. Tuissi *et al.*, "Radiopaque Shape Memory Alloys: NiTi–Er with Stable Superelasticity," *Shape Mem. Superelasticity*, vol. 2, no. 2, pp. 196–203, 2016.

[73] J. P. Bearinger, C. A. Orme, and J. L. Gilbert, "In situ imaging and impedance

measurements of titanium surfaces using AFM and SPIS," *Biomaterials*, vol. 24, no. 11, pp. 1837–1852, 2003.

[74] K. Hakshur, I. Benhar, Y. Bar-Ziv, N. Halperin, D. Segal, and N. Eliaz, "The effect of hyaluronan injections into human knees on the number of bone and cartilage wear particles captured by bio-ferrography," *Acta Biomater.*, vol. 7, no. 2, pp. 848–857, 2011.

[75] S. L. Graindorge and G. W. Stachowiak, "Changes occurring in the surface morphology of articular cartilage during wear," *Wear*, vol. 241, no. 2, pp. 143–150, 2000.

[76] S. Hiromoto and T. Hanawa, "Corrosion of Implant Metals in the Presence of Cells," *Corros. Rev.*, vol. 24, no. 5–6, pp. 323–352, 2011.

[77] J. Zhao, Y. Deng, F. Xu, and J. Zhang, "Effects of initial grain size of Al-Zn-Mg-Cu alloy on the recrystallization behavior and recrystallization mechanism in isothermal compression," *Metals (Basel).*, vol. 9, no. 2, 2019.

[78] G. Song and A. Atrens, "Understanding magnesium corrosion. A framework for improved alloy performance," *Adv. Eng. Mater.*, vol. 5, no. 12, pp. 837–858, 2003.

[79] E. A. Trillo, C. Ortiz, P. Dickerson, R. Villa, S. W. Stafford, and L. E. Murr, "Evaluation of mechanical and corrosion biocompatibility of TiTa alloys," *J. Mater. Sci. Mater. Med.*, vol. 12, no. 4, pp. 283–292, 2001.

[80] S. B. Hong, N. Eliaz, G. G. Leisk, E. M. Sachs, R. M. Latanision, and S. M. Allen, "A new Ti-5Ag alloy for customized prostheses by three-dimensional printing (3DP^{TM})," *J. Dent. Res.*, vol. 80, no. 3, pp. 860–863, 2001.

[81] C. Prakash, S. Singh, B. S. Pabla, S. S. Sidhu, and M. S. Uddin, "Bio-inspired low elastic biodegradable Mg-Zn-Mn-Si-HA alloy fabricated by spark plasma sintering," *Mater. Manuf. Process.*, vol. 34, no. 4, pp. 357–368, 2019.

[82] M. Nakagawa, S. Matsuya, K. U. Section, B. Engineering, O. Faculty, and D. Science, "Masaharu NAKAGAWA," *Dent. Mater. J.*, vol. 20, no. 4, pp. 305–314, 2001.

[83] J. Seo, Y. C. Kim, and J. W. Hu, "Pilot study for investigating the cyclic behavior of slit damper systems with recentering shape memory alloy (SMA) bending bars used for seismic restrainers," *Appl. Sci.*, vol. 5, no. 3, pp. 187–208, 2015.

[84] N. Eliaz *et al.*, "The effect of surface treatments on the adhesion of electrochemically deposited hydroxyapatite coating to titanium and on its interaction with cells and bacteria," *J. Mater. Sci. Mater. Med.*, vol. 22, no. 7, pp. 1741–1752, 2011.

[85] N. Eliaz, "Electrocrystallization of Calcium Phosphates," *Isr. J. Chem.*, vol. 48, no. 3–4, pp. 159–168, 2008.

[86] N. Metoki, C. M. R. Rosa, H. Zanin, F. R. Marciano, N. Eliaz, and A. O. Lobo, "Electrodeposition and biomineralization of nano-β-tricalcium phosphate on graphenated carbon nanotubes," *Surf. Coatings Technol.*, vol. 297, pp. 51–57, 2016.

[87] R. Zhang, N. Metoki, O. Sharabani-Yosef, H. Zhu, and N. Eliaz, "Hydroxyapatite/Mesoporous Graphene/Single-Walled Carbon Nanotubes Freestanding

Flexible Hybrid Membranes for Regenerative Medicine," *Adv. Funct. Mater.*, vol. 26, no. 44, pp. 7965–7974, 2016.

[88] C. H. Evans, D. C. Mears, and C. L. Stanitski, "Ferrographic analysis of wear in human joints. Evaluation by comparison with arthroscopic examination of symptomatic knees," *J. Bone Jt. Surg. - Ser. B*, vol. 64, no. 5, pp. 572–578, 1982.

[89] N. Metoki, S. Il Baik, D. Isheim, D. Mandler, D. N. Seidman, and N. Eliaz, "Atomically resolved calcium phosphate coating on a gold substrate," *Nanoscale*, vol. 10, no. 18, pp. 8451–8458, 2018.

[90] N. Metoki, K. Sadman, K. Shull, N. Eliaz, and D. Mandler, "Electro-Assisted Deposition of Calcium Phosphate on Self-Assembled Monolayers," *Electrochim. Acta*, vol. 206, pp. 400–408, 2016.

[91] C. Prakash, S. Singh, M. K. Gupta, M. Mia, G. Królczyk, and N. Khanna, "Synthesis, characterization, corrosion resistance and in-vitro bioactivity behavior of biodegradable Mg-Zn-Mn-(Si-HA) composite for orthopaedic applications," *Materials (Basel).*, vol. 11, no. 9, 2018.

[92] E. Ghali, "Corrosion and protection of magnesium alloys," *Mater. Sci. Forum*, vol. 350, pp. 261–272, 2000.

[93] L. Farbaniec, C. L. Williams, L. Kecskes, K. T. Ramesh, and R. Becker, "Microstructural effects on the spall properties of ECAE-processed AZ31B magnesium alloy," *Int. J. Impact Eng.*, vol. 98, no. August, pp. 34–41, 2016.

[94] O. Geuli, N. Metoki, N. Eliaz, and D. Mandler, "Electrochemically Driven Hydroxyapatite Nanoparticles Coating of Medical Implants," *Adv. Funct. Mater.*, vol. 26, no. 44, pp. 8003–8010, 2016.

[95] B. Aksakal, Ö. S. Yildirim, and H. Gul, "Metallurgical failure analysis of various implant materials used in orthopedic applications," *J. Fail. Anal. Prev.*, vol. 4, no. 3, pp. 17–23, 2004.

[96] G. W. Stachowiak and P. Podsiadlo, "Analysis of wear particle boundaries found in sheep knee joints during in vitro wear tests without muscle compensation," *J. Biomech.*, vol. 30, no. 4, pp. 415–419, 1997.

[97] C. H. Evans, D. C. Mears, and J. L. Mcknight, "A preliminary ferrographic survey of the wear particles in human synovial fluid," *Arthritis Rheum.*, vol. 24, no. 7, pp. 912–918, 1981.

[98] A. ZIEROLD, ARTHUR, "Reaction of bone to various metals," *Arch. Surg.*, 1924.

[99] D. Svetlizky, O. Levi, I. Benhar, and N. Eliaz, "Mechanical properties of Bio-Ferrography isolated cancerous cells studied by atomic force microscopy," *J. Mech. Behav. Biomed. Mater.*, vol. 91, no. April 2018, pp. 345–354, 2019.

[100] D. F. Zhang, G. L. Shi, Q. W. Dai, W. Yuan, and H. L. Duan, "Microstructures and mechanical properties of high strength Mg-Zn-Mn alloy," *Trans. Nonferrous Met. Soc. China (English Ed.*, vol. 18, no. SPEC. ISSUE 1, pp. s59–s63, 2008.

[101] F. Rosalbino, S. De Negri, G. Scavino, and A. Saccone, “Microstructure and in vitro degradation performance of Mg-Zn-Mn alloys for biomedical application,” *J. Biomed. Mater. Res. - Part A*, vol. 101 A, no. 3, pp. 704–711, 2013.

[102] K. Mendel, N. Eliaz, I. Benhar, D. Hendel, and N. Halperin, “Magnetic isolation of particles suspended in synovial fluid for diagnostics of natural joint chondropathies,” *Acta Biomater.*, vol. 6, no. 11, pp. 4430–4438, 2010.

[103] D. M. Meyer, A. Tillinghast, N. C. Hanumara, and A. Franco, “Bio-ferrography to capture and separate polyethylene wear debris from hip simulator fluid and compared with conventional filter method,” *J. Tribol.*, vol. 128, no. 2, pp. 436–441, 2006.

[104] J. Stewart and D. E. Williams, “The initiation of pitting corrosion on austenitic stainless steel: on the role and importance of sulphide inclusions,” *Corros. Sci.*, vol. 33, no. 3, 1992.

[105] S. Ifergane *et al.*, “The effect of manufacturing processes on the fatique lifetime of aeronautical bolts,” *Eng. Fail. Anal.*, vol. 8, no. 3, pp. 227–235, 2001.

[106] O. Levi, A. Shapira, B. Tal, I. Benhar, and N. Eliaz, “Isolating EGFR Overexpressing Carcinoma Cells from Human Whole Blood by Bio-Ferrography,” *Cytom. Part B Clin. Cytom.*, p. n/a-n/a, 2014.

[107] J. A. Von, “Antibiotic-metal ~~ ractions in sa ; line medium,” pp. 9–11, 1988.

[108] B. Akça and S. Z. Erzeneoɨlu, “The mass attenuation coefficients, electronic, atomic, and molecular cross sections, effective atomic numbers, and electron densities for compounds of some biomedically important elements at 59.5 kev,” *Sci. Technol. Nucl. Install.*, vol. 2014, 2014.

[109] V. G. Pronyaev, “XMuDat: Photon attenuation data on PC. Version 1.0.1 of August 1998. Summary documentation,” pp. 21–22, 1998.

[110] D. C. Mears, E. N. Hanley, R. Rutkowski, and V. C. Westcott, “Ferrographic analysis of wear particles in arthroplastic joints,” *J. Biomed. Mater. Res.*, vol. 12, no. 6, pp. 867–875, 1978.

[111] S. O. N. G. Pengfei, W. A. N. G. Jingfeng, and P. A. N. Fusheng, “Research status and prospect of high strength wrought magnesium alloys,” 2010.

[112] S. Fajardo, García-Galvan, F. R., V. Barranco, J. C. Galvan, and S. F. Batlle, “We are IntechOpen , the world ’ s leading publisher of Open Access books Built by scientists , for scientists TOP 1 %,” *Intech*, vol. i, no. tourism, p. 13, 2016.

[113] D. Bogdanski *et al.*, “Easy assessment of the biocompatibility of Ni-Ti alloys by in vitro cell culture experiments on a functionally graded Ni-NiTi-Ti material,” *Biomaterials*, vol. 23, no. 23, pp. 4549–4555, 2002.

[114] C. G. Simon, C. A. Khatri, S. A. Wight, and F. W. Wang, “Preliminary report on the biocompatibility of a moldable, resorbable, composite bone graft consisting of calcium phosphate cement and poly(lactide-co-glycolide) microspheres,” *J. Orthop. Res.*, vol. 20, no. 3, pp. 473–482, 2002.

[115] W. P. Johnson, P. Zhang, P. M. Gardner, M. E. Fuller, and M. F. DeFlaun, "Evidence for Detachment of Indigenous Bacteria from Aquifer Sediment in Response to Arrival of Injected Bacteria," *Appl. Environ. Microbiol.*, vol. 67, no. 10, pp. 4908–4913, 2001.

[116] P. Zhang, W. P. Johnson, T. D. Scheibe, K. Choi, F. C. Dobbs, and B. J. Mailloux, "•, XN • A3," vol. 37, no. 11, pp. 2687–2698, 2001.

[117] M. F. DeFlaun *et al.*, "Comparison of methods for monitoring bacterial transport in the subsurface," *J. Microbiol. Methods*, vol. 47, no. 2, pp. 219–231, 2001.

[118] W. P. Johnson and W. O. McIntosh, "Tracking of injected and resident (previously injected) bacterial cells in groundwater using ferrographic capture," *J. Microbiol. Methods*, vol. 54, no. 2, pp. 153–164, 2003.

[119] J. Venezuela and M. S. Dargusch, "The influence of alloying and fabrication techniques on the mechanical properties, biodegradability and biocompatibility of zinc: A comprehensive review," *Acta Biomater.*, vol. 87, no. xxxx, pp. 1–40, 2019.

[120] M. Syverud, J. E. Dahl, H. Herø, and E. Morisbak, "Corrosion and biocompatibility testing of palladium alloy castings," *Dent. Mater.*, vol. 17, no. 1, pp. 7–13, 2001.

[121] S. Zhao, X. Zhu, C. Cao, J. Sun, and J. Liu, "Transferrin modified ruthenium nanoparticles with good biocompatibility for photothermal tumor therapy," *J. Colloid Interface Sci.*, vol. 511, pp. 325–334, 2018.

[122] S. Seetharaman *et al.*, "Effect of erbium modification on the microstructure, mechanical and corrosion characteristics of binary Mg-Al alloys," *J. Alloys Compd.*, vol. 648, pp. 759–770, 2015.

[123] E. Willbold *et al.*, "Effect of the addition of low rare earth elements (lanthanum, neodymium, cerium) on the biodegradation and biocompatibility of magnesium," *Acta Biomater.*, vol. 11, no. 1, pp. 554–562, 2015.

[124] M. Mondet, E. Barraud, S. Lemonnier, N. Allain, and T. Grosdidier, "Optimisation of the mechanical properties of a Spark Plasma Sintered (SPS) magnesium alloy through a post-sintering in-situ precipitation treatment," *J. Alloys Compd.*, vol. 698, pp. 259–266, 2017.

[125] W. N. A. Wan Muhammad, Y. Mutoh, and Y. Miyashita, "Microstructure and mechanical properties of magnesium prepared by spark plasma sintering," *Adv. Mater. Res.*, vol. 129–131, pp. 764–768, 2010.

[126] A. BORRELL, M. DOLORES SALVADOR, V. GARCIA-ROCHA, A. FERNANDEZ, E. CHICARDI, and F. GOTOR, "Spark plasma sintering of Ti," *Mater. Sci. Eng. A. Struct. Mater.*, vol. 543, pp. 173–179, 2012.

[127] Canyon Hydro *et al.*, "We are IntechOpen , the world ' s leading publisher of Open Access books Built by scientists , for scientists TOP 1 %," *Intech*, vol. 32, no. July, pp. 137–144, 2013.

[128] M. Zavareh, A. Sarhan, M. Roudan, and P. Zavareh, "TiC–TiB2 composites: A review of processing, properties and applications," *TIC*, vol. 27, no. January 2014, p. 6.8, 2014.

[129] C. Hu, Y. Sakka, S. Grasso, and T. Nishimura, “S PARK P LASMA S INTERING (SPS), OR P ULSE D ISCHARGE S INTERING (PDS) OF MAX P HASES,” no. January, 2012.

[130] M. U. F. Khan, A. Patil, J. Christudasjustus, T. Borkar, and R. K. Gupta, “Spark plasma sintering of a high-energy ball milled Mg-10 wt% Al alloy,” *J. Magnes. Alloy.*, vol. 8, no. 2, pp. 319–328, 2020.

[131] J. Ahmed, I. H. Toor, and N. Al-Aqeeli, “Effect of sintering temperature on the corrosion properties of nanostructured Fe-18Cr-2Si alloy prepared by SPS,” *Mater. Corros.*, vol. 68, no. 3, pp. 361–367, 2017.

[132] W. Xie *et al.*, “Investigation of the sintering pressure and thermal conductivity anisotropy of melt-spun spark-plasma-sintered (Bi,Sb)2Te3 thermoelectric materials,” *J. Mater. Res.*, vol. 26, no. 15, pp. 1791–1799, 2011.

[133] F. Heyduk, D. Andrzejewski, D. Garbiec, and B. Pachutko, “Wpływ temperatury i czasu spiekania na właściwości spieków z proszku Mg wytworzonych metodą SPS,” *Obróbka Plast. Met.*, vol. 27, no. November, pp. 263–272, 2016.

[134] A. Muthuchamy, A. Raja Annamalai, and R. Ranka, “Mechanical and electrochemical characterization of super-solidus sintered austenitic stainless steel (316L),” *High Temp. Mater. Process.*, vol. 35, no. 7, pp. 643–651, 2016.